

**LABORATORY AND NUMERICAL SIMULATIONS OF  
SUB-CRITICAL SURFACE SUBSIDENCE AS AFFECTED  
BY OPENING GEOMETRY AND DEPTH**



**Suratwadee Sartkaew**

**A Thesis Submitted in Partial Fulfillment of the Requirements for the**

**Doctor of Philosophy of Engineering in Geotechnology**

**Suranaree University of Technology**

**Academic Year 2016**

การจำลองในห้องปฏิบัติการและระเบียบวิธีเชิงตัวเลขสำหรับการหลุดตัวของ  
ผิวดินที่ต่ำกว่าจุดวิกฤต ที่มีผลกระทบจากรูปทรงเรขาคณิต  
และความลึกของช่องเหมือง



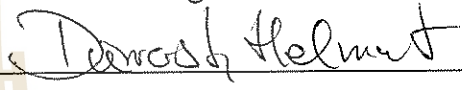
นางสาวสุรตีวดี ศาสตร์แก้ว

วิทยานิพนธ์นี้เป็นส่วนหนึ่งของการศึกษาตามหลักสูตรปริญญาวิศวกรรมศาสตรดุษฎีบัณฑิต  
สาขาวิชาเทคโนโลยีธรณี  
มหาวิทยาลัยเทคโนโลยีสุรนารี  
ปีการศึกษา 2559

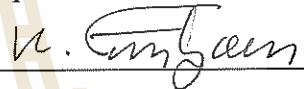
**LABORATORY AND NUMERICAL SIMULATIONS OF SUB-  
CRITICAL SURFACE SUBSIDENCE AS AFFECTED BY  
OPENING GEOMETRY AND DEPTH**

Suranaree University of Technology has approved this thesis submitted in partial fulfillment of the requirements for the Degree of Doctor of Philosophy.


Thesis Examining Committee

  
\_\_\_\_\_  
(Asst. Prof. Dr. Helmut Dürrast)


Chairperson

  
\_\_\_\_\_  
(Prof. Dr. Kittitep Fuenkajorn)

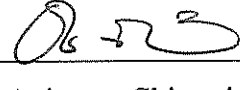
Member (Thesis Advisor)

  
\_\_\_\_\_  
(Asst. Dr. Decho Phueakphum)


Member

  
\_\_\_\_\_  
(Dr. Prachya Tepnarong)

Member

  
\_\_\_\_\_  
(Dr. Anisong Chitnarin)

Member

  
\_\_\_\_\_  
(Assoc. Prof. Ft. Lt. Dr. Kontorn Chamniprasart)

  
\_\_\_\_\_  
(Prof. Dr. Sukit Limpijumnong)

Vice Rector for Academic Affairs  
and Innovation

Dean of Institute of Engineering

สุรติวัติ ศาสตร์แก้ว : การจำลองในห้องปฏิบัติการและระเบียบวิธีเชิงตัวเลขสำหรับการทรุดตัวของผิวดินที่ต่ำกว่าจุดวิกฤต ที่มีผลกระทบจากรูปทรงเรขาคณิตและความลึกของช่องเหมือง (LABORATORY AND NUMERICAL SIMULATIONS OF SUB-CRITICAL SURFACE SUBSIDENCE AS AFFECTED BY OPENING GEOMETRY AND DEPTH) อาจารย์ที่ปรึกษา : ศาสตราจารย์ ดร.กิตติเทพ เพ็ญขจร, 124 หน้า.

แบบจำลองเชิงกายภาพและแบบจำลองเชิงตัวเลขได้นำมาศึกษาเพื่อตรวจสอบความถูกต้องของโปรแกรมฟังก์ชันในการกำหนดโปรแกรมการทรุดตัวภายใต้สภาวะที่ต่ำกว่าจุดวิกฤต ชั้นหินปิดทับได้จำลองด้วยส่วนผสมของเจลสังเคราะห์และพาราฟิน คุณสมบัติของเจลและขนาดความกว้างและความลึกของช่องเหมืองที่ใช้ในแบบจำลองสามารถสัมพันธ์กับคุณสมบัติของชั้นหินปิดทับบริเวณเหมืองเกลือและเหมืองโพแทชในหมวดหินมหาสารคาม โดยใช้กฎการเปรียบเทียบของขนาด ค่าตรวจวัดจากแบบจำลองทางกายภาพนำมาคำนวณหาค่าการทรุดตัวสูงสุด ค่าความชัน ค่าความเครียดในแนวระนาบและค่ามุมความโค้ง ผลจากแบบจำลองทางกายภาพและแบบจำลองเชิงตัวเลขของช่องเหมืองเดี่ยวในแนวระนาบมีความสอดคล้องกันเป็นอย่างดี โดยพบว่าช่องเหมืองในระดับลึกส่งผลให้ค่าการทรุดตัวและค่าความชันน้อย องค์ประกอบของการทรุดตัวมีค่าเพิ่มขึ้นเมื่ออัตราส่วนความกว้างต่อความลึกของช่องเหมืองเพิ่มขึ้น ภายใต้ความกว้างของร่องการทรุดตัวที่เท่ากัน ฟังก์ชันตรีโกณมิติสามารถประเมินค่าองค์ประกอบของการทรุดตัวได้ต่ำกว่าแบบจำลองทางกายภาพ โดยเฉพาะอย่างยิ่งช่องเหมืองที่มีขนาดเล็ก ฟังก์ชันไฮเปอร์โบลิกให้ค่าการประเมินสูงกว่าแบบจำลองทางกายภาพประมาณร้อยละ 10 และฟังก์ชันเอกซ์โพเนนเชียลสามารถประเมินค่าองค์ประกอบของการทรุดตัวได้ใกล้เคียงกับแบบจำลองทางกายภาพมากที่สุด ซึ่งมีค่าต่ำกว่าแบบจำลองเชิงกายภาพประมาณร้อยละ 5 ในทุกกรณี

สาขาวิชา เทคโนโลยีธรณี  
ปีการศึกษา 2559

ลายมือชื่อนักศึกษา สุรติวัติ ศาสตร์แก้ว  
ลายมือชื่ออาจารย์ที่ปรึกษา ดร.กิตติเทพ เพ็ญขจร

SURATWADEE SARTKAEW : LABORATORY AND NUMERICAL  
SIMULATIONS OF SUB-CRITICAL SURFACE SUBSIDENCE AS  
AFFECTED BY OPENING GEOMETRY AND DEPTH.

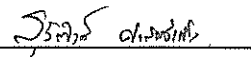
THESIS ADVISOR : PROF. KITTITEP FUENKAJORN, Ph.D., P.E.,  
124 PP.

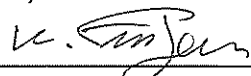
ANGLE OF DRAW/ PROFILE FUNCTION/ SCALE LAW/ TROUGH

Physical and numerical simulations are performed to verify the representativeness of some profile functions used to define the subsidence profiles under sub-critical to critical conditions. Synthetic gel with paraffin is used to simulate the overburden. Based on the scale law the gel properties and the opening depths and widths can be correlated with those of the prototypes of the overburden above salt and potash mines in the Maha Sarakham formation. The model measurements are used to calculate the maximum subsidence, slope, horizontal strains and curvature angle. The physical model results under single isolated horizontal opening agree well with those obtained from numerical analyses that deeper opening induces smaller maximum subsidence and slope. All components increase with opening width-to-depth ratio. Under the same trough width, the trigonometric function underpredicts the subsidence components particularly for small openings. The hyperbolic predictions are about 10% greater than the physical model results. The exponential function gives the closest predictions while it underestimates the model results by less than 5% for all cases.

School of Geotechnology

Academic Year 2016

Student's Signature 

Advisor's Signature 

## ACKNOWLEDGMENTS

I wish to acknowledge the funding supported by Suranaree University of Technology (SUT).

I would like to express my sincere thanks to Prof. Dr. Kittitep Fuenkajorn for his valuable guidance and efficient supervision. I appreciate his strong support, encouragement, suggestions and comments during the research period. My heartiness thanks to Asst. Prof. Dr. Helmut Dürrast, Assist. Dr. Decho Phueakphum, Dr. Prachya Tepnarong and Dr. Anisong Chitnarin for their constructive advice, valuable suggestions and comments on my research works as thesis committee members. Grateful thanks are given to all staffs of Geomechanics Research Unit, Institute of Engineering who supported my work.

Finally, I would like to thank beloved parents for their love, support and encouragement.

มหาวิทยาลัยเทคโนโลยีสุรนารี

Suratwadee Sartkaew

# TABLE OF CONTENTS

	<b>Page</b>
ABSTRACT (THAI) .....	I
ABSTRACT (ENGLISH).....	II
ACKNOWLEDGEMENTS .....	III
TABLE OF CONTENTS.....	IV
LIST OF TABLES .....	IX
LIST OF FIGURES .....	XI
SYMBOLS AND ABBREVIATIONS.....	XIV
<b>CHAPTER</b>	
<b>I INTRODUCTION.....</b>	<b>1</b>
1.1 Background and rationale .....	1
1.2 Research objectives.....	3
1.3 Scope and limitations .....	4
1.4 Research methodology .....	4
1.4.1 Literature review.....	5
1.4.2 Material preparation.....	6
1.4.3 Fabrication of the test frame .....	6
1.4.4 Physical modelling method.....	6
1.4.5 Physical model results .....	7

## TABLE OF CONTENTS (Continued)

	<b>Page</b>
1.4.6 Comparison of computer and physical model .....	7
1.4.7 Profile functions.....	7
1.4.8 Discussions, conclusion and thesis writing .....	8
1.5 Thesis contents .....	8
<b>II LITERATURE REVIEW .....</b>	<b>9</b>
2.1 Introduction.....	9
2.2 Calculation and prediction of surface subsidence.....	9
2.3 Numerical simulations for subsidence prediction.....	13
2.4 Similarity theory (Scale law) .....	20
2.5 Physical modeling.....	27
2.6 Effect of underground opening geometries and overburden properties on surface subsidence .....	36
<b>III MATERIAL PREPARATION.....</b>	<b>40</b>
3.1 Introduction.....	40
3.2 Overburden simulator .....	40
<b>IV FABRICATION OF THE TEST FRAME.....</b>	<b>51</b>
4.1 Introduction.....	51
4.2 Design and fabrication of the test apparatus .....	51



## TABLE OF CONTENTS (Continued)

	<b>Page</b>
<b>V PHYSICAL MODELLING METHOD</b> .....	56
5.1 Introduction.....	56
5.2 Similarity theory (scale law) .....	56
5.3 Physical model testing .....	57
<b>VI PHYSICAL MODEL RESULTS</b> .....	66
6.1 Introduction.....	66
6.2 Test results .....	66
6.3 Prediction .....	80
<b>VII COMPARISON OF COMPUTER AND PHYSICAL MODEL</b> .....	87
7.1 Introduction.....	87
7.2 Computer simulations .....	87
7.3 Comparison of numerical and physical results .....	89
<b>VIII PROFILE FUNCTIONS</b> .....	103
8.1 Introduction.....	103
8.2 Profile functions.....	103
8.3 Comparison of analytical and physical results .....	105
<b>IX DISCUSSIONS AND CONCLUSIONS</b> .....	121
9.1 Discussions .....	121
9.2 Conclusions.....	122

**TABLE OF CONTENTS (Continued)**

	<b>Page</b>
9.3 Recommendations for future studies .....	124
REFERENCES .....	125
BIOGRAPHY .....	132



## LIST OF TABLES

Table	Page
2.1 Scale factors (Wood, 2004).....	23
2.2 Similarity theory constants (Ghabraie et al., 2015).....	26
3.1 Specimen dimensions prepared for uniaxial compression testing.....	43
5.1 Density ( $\rho_p$ ) and elasticity ( $E_p$ ) of Maha Sarakham formation used as prototype properties (Crosby, 2007; Wetchasat, 2002).....	61
5.2 Similarity theory constants.....	62
5.3 Test variables.....	64
6.1 Physical model results under different opening depths and widths for elastic modulus = 1 MPa.....	69
6.2 Physical model results under different opening depths and widths for elastic modulus = 3 MPa.....	69
6.3 Physical model results under different opening depths and widths for elastic modulus = 5 MPa.....	70
6.4 Physical model results correlated with actual fields conditions.....	86
7.1 FLAC simulation parameters.....	88
7.2 Numerical simulation results under different opening depths and widths for elastic modulus = 1 MPa.....	91

## LIST OF TABLES (Continued)

<b>Table</b>	<b>Page</b>
7.3 Numerical simulation results under different opening depths and widths for elastic modulus = 3 MPa.....	91
7.4 Numerical simulation results under different opening depths and widths for elastic modulus = 5 MPa.....	92
8.1 Maximum slope ( $\times 10^{-3}$ ) values from physical and analytical methods under different opening geometries and elastic moduli.....	107
8.2 Maximum horizontal displacement-to-opening depth ratio values from physical and analytical methods under different opening geometries and elastic moduli.....	108
8.3 Maximum horizontal strain ( $\times 10^{-3}$ ) values from physical and analytical methods under different opening geometries and elastic moduli.....	109
8.4 Curvature angle (degrees) values from physical and analytical methods under different opening geometries and elastic moduli.....	110

## LIST OF FIGURES

Figure	Page
1.1 Research methodology.....	5
2.1 Schematic of ground movements caused by subsidence (Singh, 1992).....	11
2.2 Properties of error function curve to represent cross-section settlement trough above tunnel (Peck, 1969).....	13
2.3 Sensitivity analysis on panel width (Shahriar et al., 2009).....	15
2.4 Sensitivity analysis on seam depth (Shahriar et al., 2009).....	16
2.5 Comparison between monitored and computed (FEM) vertical displacements corresponding to the tunnel section with a centerline depth of 11.5 m as a function of the distance from the tunnel face (Migliazza et al., 2009).....	17
2.6 Basic subsidence mesh and model dimensions (Ren and Li, 2008).....	19
2.7 Surface subsidence curves of different unconsolidated layers thickness (Dai et al., 2011).....	20
2.8 Experimental setup (Tunsakul et al., 2013).....	24
2.9 Small-scale model of masonry structure (wood or sugar blocks) and foundation (silicon): (a) model; (b) wood; (c) sugar (Heib et al., 2013).....	25
2.10 Angles of draw and break and terminology for referring to different areas around first and second extractions (Ghabraie et al., 2015).....	27

## LIST OF FIGURES (Continued)

Figure	Page
2.11 Classical trap door problem (Terzaghi, 1936).....	28
2.12 Variables used by Fuenkajorn and Aracheeploha (2009).....	29
2.13 Surface settlement measured for applied displacements of 1 mm and 4 mm (Park et al., 1999).....	32
2.14 Three-dimensional trapdoor tester (side view) (Adachi et al., 2003).....	33
2.15 Test setup and failure mechanism (Sterpi et al., 1996).....	34
2.16 Schematic diagram of the model box (Wang et al., 2015).....	35
2.17 Effect of different overburden properties on the angle of draw (Yao et al., 1991).....	36
2.18 Volumetric ratio of trough volume to excavation volume ( $V_s/V_o$ ) as a function of opening depth ratio $Z/W$ (a) and opening height ratio $H/W$ (b) for four values of length to width ratio $L/W$ (Thongprapha et al., 2015).....	39
3.1 Synthetic gel mixed with paraffin under 60 °c.....	41
3.2 Some gel specimens prepared for uniaxial compression test.....	41
3.3 Gel specimen placed in a universal testing machine (UTM).....	42
3.4 Stress-strain curves obtained from gel specimens with paraffin contents 10% by weight.....	45
3.5 Stress-strain curves obtained from gel specimens with paraffin contents 32% by weight.....	46

## LIST OF FIGURES (Continued)

Figure	Page
3.6	Stress-strain curves obtained from gel specimens with paraffin contents 36% by weight..... 47
3.7	Stress-strain curves obtained from gel specimens with paraffin contents 40% by weight..... 48
3.8	Stress-strain curves obtained from gel specimens with paraffin contents 45% by weight..... 49
3.9	Elastic modulus (a) and Poisson's ratio (b) of synthetic gel as a function of paraffin additive content..... 50
4.1	Trap door apparatus used for physical model testing..... 52
4.2	Perspective view of trap door apparatus..... 53
4.3	Front view of trap door apparatus..... 53
4.4	Side view of trap door apparatus..... 54
4.5	Plane view of trap door apparatus..... 54
4.6	Measurement system of trap door apparatus..... 55
4.1	Trap door apparatus used for physical model testing..... 52
4.2	Perspective view of trap door apparatus..... 53
4.3	Front view of trap door apparatus..... 53
4.4	Side view of trap door apparatus..... 54
4.5	Plane view of trap door apparatus..... 54
4.6	Measurement system of trap door apparatus..... 55

## LIST OF FIGURES (Continued)

Figure	Page
5.1	Locations of overburden above salt openings in the Maha Sarakham formation.....58
5.2	Stratigraphic units of three boreholes drilled in the Maha Sarakham formation.....60
5.2	Stratigraphic units of three boreholes drilled in the Maha Sarakham formation.....60
5.3	Trap door apparatus used in physical model simulations.....63
5.4	Synthetic gel melted into viscous fluid under temperature of 60 °c.....65
5.5	Filling synthetic gel into material container.....65
6.1	Variables used in physical model simulations.....67
6.2	Example of three-dimensional image of gel subsidence for Z = 40 mm and W = 250 mm (a) and cross-section image (b) (left) and Z = 100 mm and W = 100 mm (right). Vertical scale is greatly exaggerated.....68
6.3	Angle of draw (a) and maximum subsidence-to-opening depth ratio (b) as a function of the opening width-to-depth ratios (W/Z) for various elastic modulus of model.....71
6.4	Maximum surface slope (a) curvature angle (b) as a function of the opening width-to-depth ratios for various elastic modulus of model.....72



## LIST OF FIGURES (Continued)

Figure	Page
6.5	Maximum horizontal displacement-to-opening depth ratio (a) and maximum horizontal strain (b) as a function of the opening width-to-depth ratio for various elastic modulus of model.....72
6.6	Subsidence profiles measured from physical model test under $E_m = 1$ MPa for various opening width and depth.....74
6.7	Subsidence profiles measured from physical model test under $E_m = 3$ MPa for various opening width and depth.....75
6.8	Subsidence profiles measured from physical model test under $E_m = 5$ MPa and opening depth = 40 mm.....76
6.9	Subsidence profiles measured from physical model test under $E_m = 5$ MPa and opening depth = 60 mm.....77
6.10	Subsidence profiles measured from physical model test under $E_m = 5$ MPa and opening depth = 80 mm.....78
6.11	Subsidence profiles measured from physical model test under $E_m = 5$ MPa and opening depth = 100 mm.....79
6.12	Volumetric ratio of trough volume-to-excavation volume ( $V_s/V_o$ ) as a function of opening width-to-depth ratio for various elastic moduli.....80
6.13	Predicted angle of draw (a) and maximum subsidence-to-opening depth ratio (b) as a function of the opening width-to-depth ratios ( $W/Z$ ) for various elastic modulus of model ( $E_m$ ).....83

## LIST OF FIGURES (Continued)

Figure	Page
6.14 Predicted maximum surface slope (a) curvature angle (b) as a function of the opening width-to-depth ratios ( $W/Z$ ) for various elastic modulus of model ( $E_m$ ).....	84
6.15 Predicted maximum horizontal displacement-to-opening depth ratio (a) and maximum horizontal strain (b) as a function of the opening width-to-depth ratios ( $W/Z$ ) for various elastic modulus of model ( $E_m$ ).....	84
6.16 Predicted volumetric ratio of trough volume to excavation volume ( $V_s/V_o$ ) as a function of the opening width-to-depth ratios ( $W/Z$ ) for various elastic modulus of model ( $E_m$ ).....	85
7.1 Example of finite difference mesh developed for FLAC simulations.....	90
7.2 Comparison of angle of draw (a) and maximum subsidence-to-opening depth ratio (b) obtained from FLAC and physical model test.....	94
7.3 Comparison of maximum slope (a) and curvature angle (b) obtained from FLAC and physical model test.....	94
7.4 Comparison of maximum horizontal displacement-to-opening depth ratio (a) and maximum horizontal strain (b) obtained from FLAC and physical model test.....	95
7.5 Comparison of volumetric ratio of trough-to-opening ( $V_s/V_o$ ) obtained from FLAC and physical model test.....	95

## LIST OF FIGURES (Continued)

<b>Figure</b>	<b>Page</b>
7.6 Comparisons of subsidence profiles measured from physical and predicted by numerical model under $E_m = 1$ MPa for various opening width and depth.....	97
7.7 Comparisons of subsidence profiles measured from physical and predicted by numerical model under $E_m = 3$ MPa for various opening width and depth.....	98
7.8 Comparisons of subsidence profiles measured from physical and predicted by numerical model under $E_m = 5$ MPa and opening depth = 40 mm.....	99
7.9 Comparisons of subsidence profiles measured from physical and predicted by numerical model under $E_m = 5$ MPa and opening depth = 60 mm.....	100
7.10 Comparisons of subsidence profiles measured from physical and predicted by numerical model under $E_m = 5$ MPa and opening depth = 80 mm.....	101
7.11 Comparisons of subsidence profiles measured from physical and predicted by numerical model under $E_m = 5$ MPa and opening depth = 100 mm.....	102
8.1 Comparisons of subsidence profile predicted by different functions under $E_m = 1$ MPa for various opening width and depth.....	111

## LIST OF FIGURES (Continued)

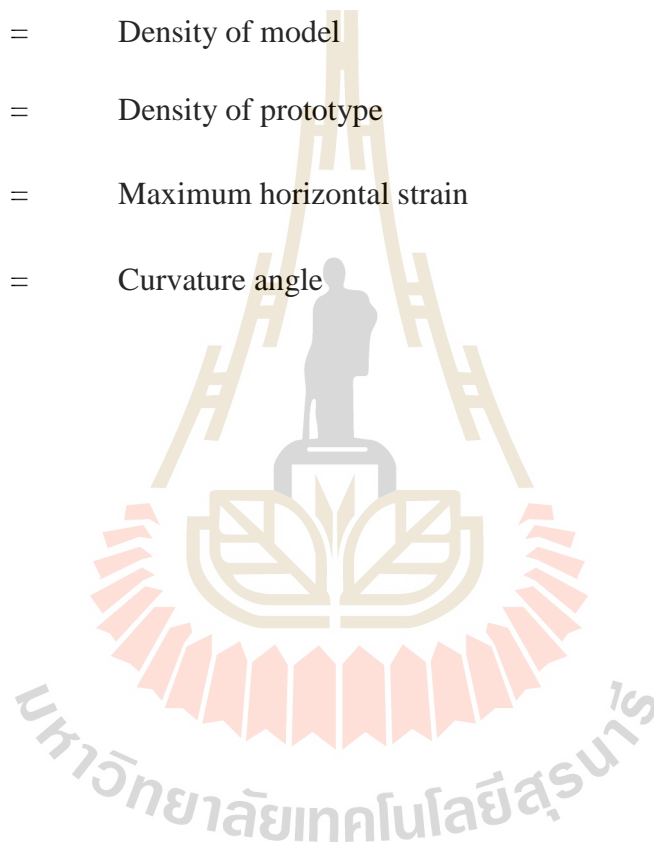
Figure	Page
8.2	Comparisons of subsidence profile predicted by different functions under $E_m = 3$ MPa for various opening width and depth ..... 112
8.3	Comparisons of subsidence profile predicted by different functions under $E_m = 5$ MPa and opening depth = 40 mm ..... 113
8.4	Comparisons of subsidence profile predicted by different functions under $E_m = 5$ MPa and opening depth = 60 mm ..... 114
8.5	Comparisons of subsidence profile predicted by different functions under $E_m = 5$ MPa and opening depth = 80 mm ..... 115
8.6	Comparisons of subsidence profile predicted by different functions under $E_m = 5$ MPa and opening depth = 100 mm ..... 116
8.7	Maximum slope comparisons between physical model and three profile functions where W/Z ratios = 1 – 4 ..... 117
8.8	Curvature angle comparisons between physical model and three profile functions where W/Z ratios = 1 – 4 ..... 118
8.9	Maximum horizontal displacement-to-opening depth ratio comparisons between physical model and three profile functions where W/Z ratios = 1 – 4 ..... 119
8.10	Maximum horizontal strain comparisons between physical model and three profile functions where W/Z ratios = 1 – 4 ..... 120

## SYMBOLS AND ABBREVIATIONS

$B$	=	Width of trough
$c$	=	arbitrary constant
$C_E$	=	Constants for the elastic modulus similarity of the prototype to the model
$C_L$	=	Constants for the dimension similarity of the prototype to the model
$C_\rho$	=	Constants for the density similarity of the prototype to the model
$E_m$	=	Elastic modulus of model
$E_p$	=	Elastic modulus of prototype
$G(x)$	=	Surface slope
$G_{max}$	=	Maximum slope
$H$	=	Opening height
$K(x)$	=	Curvature
$L$	=	Opening length
$L_m$	=	Dimension of model
$L_p$	=	Dimension of prototype
$S(x)$	=	Surface subsidence
$S_{max}$	=	Maximum subsidence
$U_{max}$	=	Maximum horizontal displacement
$V_o$	=	Opening volume

**SYMBOLS AND ABBREVIATIONS (Continued)**

$V_s$	=	Trough volume
$W$	=	Opening width
$x$	=	Horizontal distance from the point of inflection
$Z$	=	Opening depth
$\rho_m$	=	Density of model
$\rho_p$	=	Density of prototype
$\epsilon_{max}$	=	Maximum horizontal strain
$\psi$	=	Curvature angle



# CHAPTER I

## INTRODUCTION

### 1.1 Background and rationale

The rapid growth of resources exploitation and the potential development of underground space utilization has called for a true understanding of the mechanical behavior of the Maha Sarakham rock salt, particularly that of the Middle and Lower members. The salt formation hosts several solution-mined caverns, and is considered as a host rock for compressed-air energy storage caverns by the Thai Department of Energy, and for chemical waste disposal by the Office of Atomic Energy for Peace (Fuenkajorn and Archeeploha, 2011; Fuenkajorn and Phueakphum, 2010). One of the primary concern is the environmental impact due to ground surface subsidence. This subsidence is sometimes of little importance to green field sites (i.e., those without surface structures), but it may cause significant damage where engineering structures and farmlands are present. The local regulations state that mine surface subsidence must be below the critical condition, the subsidence components must not have adverse effects on the manmade structures, agriculture areas and natural resources on and near ground surface, and that analytical, observational and numerical methods are required to confirm the subsidence characteristics induced by site-specific conditions.

A variety of methods has been developed to study the surface subsidence induced by underground mines (Nieland, 1991; Cui et al., 2000; Asadi et al., 2005).

One of them is the empirical method which is sets of equations derived based on observations and actual field measurements. They can be presented in several forms of mathematical functions. Such relations are intended to describe the profile of the surface subsidence, and hence sometimes called “profile function” (Singh, 1992). Some that are notably mentioned include hyperbolic, exponential and trigonometric functions. These functions are widely accepted for sub-critical to critical conditions because they are quick and simple to use, and yield fairly satisfactory results (Rafael and Javier, 2000; Asadi et al., 2004).

Numerical methods have also been employed for the subsidence analysis, primarily to predict the maximum subsidence, and the sizes and shape of the subsidence trough. The extent of subsidence area is predominantly controlled by geological conditions of the overburden strata. A variety of numerical codes have been used ranging from linearly elastic, plastic, to visco-elastic plastic models (Migliazza et al., 2009; Fuenkajorn and Archeeploha, 2011; Helm et al., 2013; Cai et al., 2014; Gao et al., 2014). The main drawback of the numerical approaches is that they require representative material parameters and accurate boundary and loading conditions of the simulated domains. This means that extensive laboratory and field testing and measurements are required to obtain representativeness of the input data.

Physical modelling has long been a research tool for understanding of the subsidence mechanisms (Terzaghi, 1936; Adachi et al., 2003; Ghabraie et al., 2015; Thongprapha et al., 2015). Several modeling techniques has been developed worldwide to study the ground responses to the underground excavations. These techniques range from two-dimensional trap door tests to miniature tunnel boring machines that can simulate the process of tunnel excavation and lining installation in



a centrifuge (Park et al., 1999; Meguid et al., 2008). The primary advantage of the physical or scaled-down model test is that the boundaries and loading conditions and material properties can be well controlled, and hence provides the results that are isolated from the effects of material inhomogeneity, complex shape and boundary loadings.

Even though the profile functions and numerical simulations have widely been accepted to describe the subsidence characteristics, verification of their predictability has rarely been attempted. To ensure that these simple methods are adequately reliable to predict the actual field phenomena, verification of their results with the laboratory test (physical) model under identical boundary conditions is needed.

## **1.2 Research objectives**

The objective of this study is to simulate the surface subsidence under sub-critical condition as affected by overburden properties, mine opening geometries and depths by using scale-down physical and numerical models. The synthetic gel and paraffin wax are used to represent the overburdens in order to exhibit an elastic behavior. The mixing ratios are varied to obtain 3 different properties. The results are focused on the maximum subsidence, angle of draw, volume of the subsidence trough, slope and curvature of the ground surface. The physical model results are compared with the analytical methods given by Singh (1992) and with the numerical simulations (FLAC 4.0) in terms of the subsidence components above.

### 1.3 Scope and limitations

The scope and limitations of the research include as follows.

- 1) Scaled-down physical model are developed in the laboratory with the size of 75×75×30 cm.
- 2) Synthetic gel and paraffin wax are prepared to simulate the elastic overburden and the mixing ratios are varied to obtain 3 different properties.
- 3) The opening width varies from 50 mm to 250 mm with an increment of 50 mm. The overburden thickness or opening depth is varied from 40 to 100 mm with the outer boundary of 0.5 m from the openings. The opening length and height are 200 and 10 mm.
- 4) Maximum subsidence values, angle of draw, slopes, curvature and volume of the subsidence trough are determined.
- 5) Physical model results are compared with the analytical methods given by Singh (1992) and with numerical simulations (using FLAC 4.0 software).
- 6) The main focus is on the sub-critical subsidence induced by manmade underground openings (e.g. mines, tunnels and caverns).

### 1.4 Research methodology

The research methodology shown in Figure 1.1 comprises 8 steps; including literature review, material preparation, fabrication of the test frame, physical modelling method, physical model results, comparison of computer and physical model, profile functions, discussions and conclusions, and thesis writing and presentation.

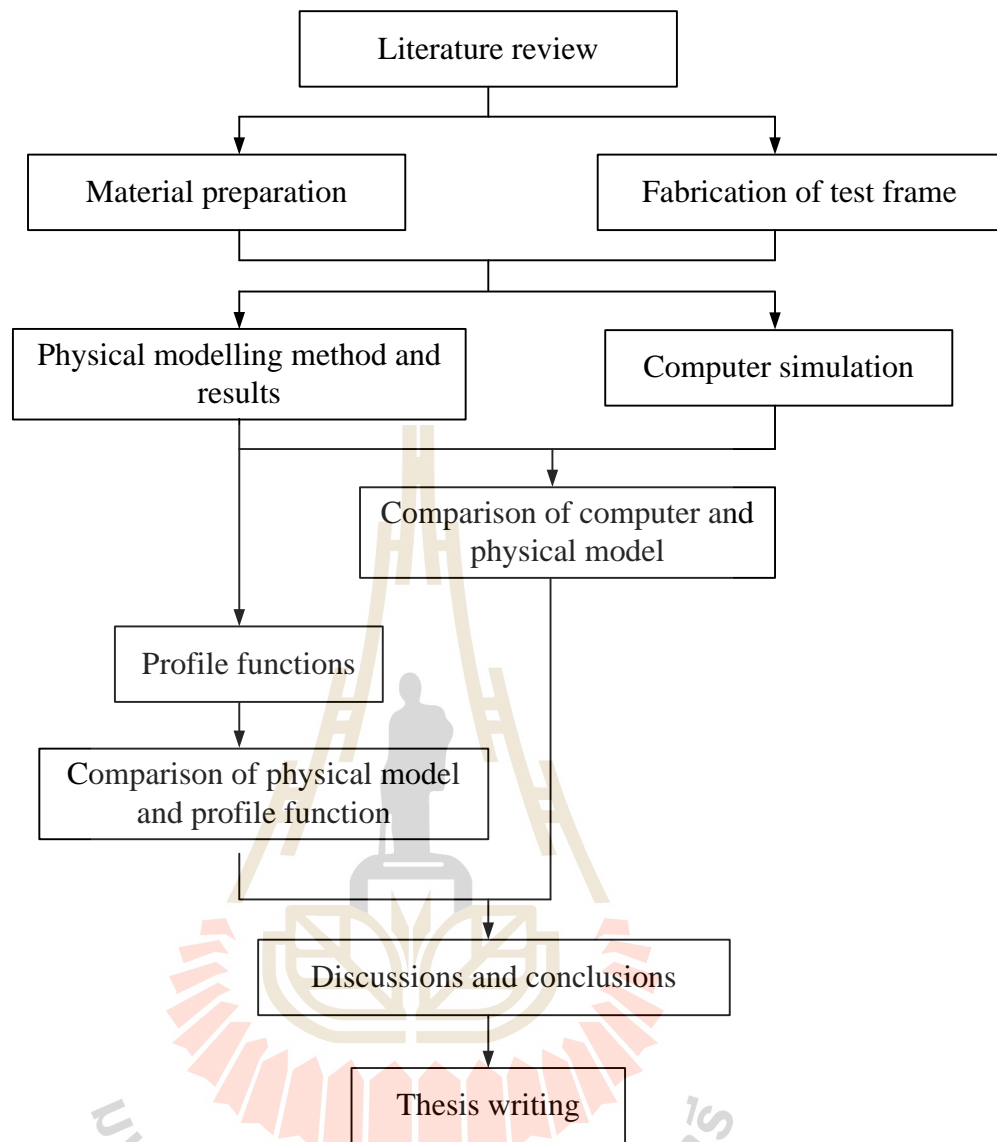


**Figure 1.1** Research Methodology.

#### 1.4.1 Literature review

Literature review are carried out to improve an understanding of sub-critical surface subsidence knowledge and case studies in Thailand and abroad. The sources of information are from journals, technical reports and conference papers. A summary of the literature review are given in the thesis.

### **1.4.2 Material preparation**

The synthetic gel and paraffin wax are prepared to simulate the overburden in the physical model. The main factor of the material used to simulate the overburden is universally obtainable and non-toxic. The physical properties of the overburden are independent of variations of temperatures and humidity. The mixing ratios of the synthetic gel to paraffin wax are varied to obtain 3 different properties. The uniaxial compression tests are performed to determine the elastic modulus and Poisson's ratio of the material.

### **1.4.3 Fabrication of the test frame**

A trap door apparatus is made to simulate surface subsidence in three dimensions and to assess the effect of the overburden properties on the surface subsidence. The testing space is  $0.75 \times 0.75 \times 0.30 \text{ m}^3$ . The mine opening simulator is an array of plastic blocks with sizes of  $50 \times 100 \times 200 \text{ mm}^3$ . The blocks can be gradually and systematically moved down to simulate underground openings with different geometries. The laser scan is used to measure the top profile of the material before and after the overburden deformation is induced. The results are recorded and plotted as three-dimensional profiles. The maximum subsidence value, angles of draw, slopes, curvature and volume of the subsidence trough are readily determined for all cases.

### **1.4.4 Physical modelling method**

The physical model testing in this study is to assess the effects of the opening geometry and depth on the surface subsidence. Based on the similarity theory, the mechanical and physical properties of the gel and the opening geometries are correlated with the overburden and geometry of actual mines in the Maha Sarakham

formation. The opening width is simulated from 50, 100, 150, 200 to 250 mm. The overburden thickness or opening depth is varied from 40, 60, 80 to 100 mm. The opening length and height are maintained constant at 200 and 10 mm, respectively. Each testing are simulated under different elastic moduli, including 1, 3 and 5 MPa. The subsidence profiles are used to calculate the subsidence components, including the angle of draw, maximum subsidence, trough volume, surface slope, curvature and horizontal strains.

#### **1.4.5 Physical model results**

The angle of draw, trough volume, surface slope, strains and curvature are used to develop a set of empirical equations as a function of opening width-to-depth ratios and elastic moduli of the gel using SPSS statistical software. The equations can be correlated with the actual field condition based on the scale law.

#### **1.4.6 Comparison of computer and physical model**

The finite difference analyses using finite difference code (FLAC 4.0) (Itasca, 1992) to simulate the surface subsidence profiles correlated with the overburden elastic properties and underground opening configurations. The results obtained from the FLAC are compared with the physical model simulations.

#### **1.4.7 Profile functions**

The analytical methods given by Singh (1992) are used to calculate the subsidence components as affected by the opening geometries and overburden properties. The maximum subsidence, slope, curvature, horizontal displacement and strain are estimated using different profile functions. The analytical results are compared and verified with the laboratory model.

#### **1.4.8 Discussions, conclusion and thesis writing**

All study activities, methods, and results are documented and compiled in the thesis.

### **1.5 Thesis contents**

**Chapter I** describes the objectives, the problems and rationale, and the methodology of the research. **Chapter II** present results of the literature review to improve an understanding of surface subsidence knowledge and case studies in Thailand and abroad. **Chapter III** describes the material preparation. **Chapter IV** describes the design and fabrication of the test frame. **Chapter V** describes the physical model method and similarity theory. **Chapter VI** presents the physical model results under a variety of opening depths and widths and overburden properties. **Chapter VII** proposes subsidence prediction using FLAC 4.0 and compared with the physical model simulations. **Chapter VIII** presents the analytical methods given by Singh (1992) for used to calculate the subsidence components and compared with the laboratory model. **Chapter IX** presents discussions, conclusions and recommendation for future studies.

## **CHAPTER II**

### **LITERATURE REVIEW**

#### **2.1 Introduction**

Relevant topics and previous research results are reviewed to improve an understanding of surface subsidence and case studies. These include the effects of underground opening geometries and overburden properties on surface subsidence, surface subsidence prediction, similarity theory (scale law), physical modeling, empirical subsidence calculation and numerical simulations. The review results are summarized below.

#### **2.2 Calculation and prediction of surface subsidence**

Singh (1992) states that subsidence is an inevitable consequence of underground mining – it may be small and localized or extend over large areas, it may be immediate or delayed for many years. During recent years, with the expansion of urbanization and increased concern for the environment, it is no longer possible to ignore its aftermath.

The major objectives of subsidence engineering are

- 1) Prediction of ground movement.
- 2) Determining the effects of such movements on structures and renewable resource.
- 3) Minimizing damage due to subsidence.

Whenever a cavity is created underground, due to the mining of minerals or for any other reason, the stress field in the surrounding strata is disturbed. These stress changes produce deformations and displacements of the strata, the extent of which depends on the magnitude of the stresses and the cavity dimensions. With time, supporting structures deteriorate and the cavity enlarges, resulting in instability. This induces the superjacent strata to move into the void. Gradually, these movements work up to the surface, manifesting themselves as a depression. This is commonly referred to as subsidence. Thus mine subsidence may be defined as ground movements that occur due to the collapse of overlying strata into mine voids. Surface subsidence generally entails both vertical and lateral movements.

Subsidence consists of five major components, which influence damage to surface structures and renewable resources are vertical displacement, slope, curvature, horizontal displacement and horizontal strain (Figure 2.1).

Calculation by profile function;

Vertical displacement:

$$S(x) = \frac{1}{2} S_{\max} [1 - \tanh (cx/B)] \quad (2.1)$$

Slope (or tilt):

$$G(x) = S'(x) = -\frac{1}{2} S_{\max} (c/B) \operatorname{sech}^2 (cx/B) \quad (2.2)$$

Curvature:

$$\rho(x) = S''(x) = S_{\max} (c^2/B^2) [\operatorname{sech}^2 (cx/B) \tanh (cx/B)] \quad (2.3)$$



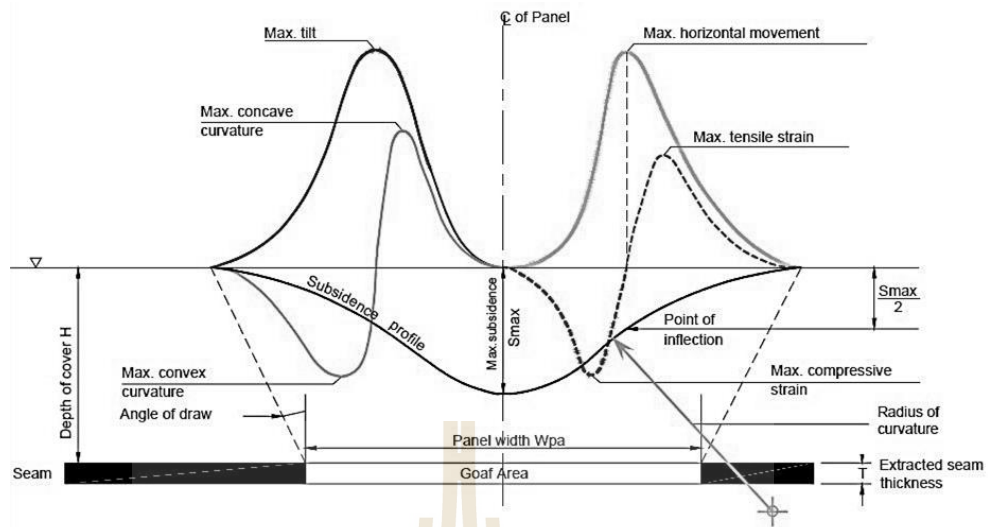


**Figure 2.1** Schematic of ground movements caused by subsidence (Singh, 1992).

Horizontal displacement (lateral movement):

$$u(x) = -\frac{1}{2} S_{\max} (bc/B) \operatorname{sech}^2 (cx/B) \quad (2.4)$$

Horizontal strain:

$$\varepsilon(x) = S_{\max} (bc^2/B^2) [\operatorname{sech}^2 (cx/B) \tanh (cx/B)] \quad (2.5)$$

where  $S_{\max}$  is the maximum subsidence,

$D$  is depth of cavern,

$\gamma$  is angle of draw,

$x$  is horizontal distance,

$c$  is arbitrary constant, where  $c = 1.8$  for critical and supercritical widths, and  $c$

$= 1.4$  for subcritical widths

$b$  is constant, and

$B$  is maximum radius of cavern area.

Peck (1969) describes settlement data from over twenty case histories. It follows that the short-term transverse settlement trough in the ‘Greenfield’ could be approximated by a normal distribution or Gaussian curve, as shown in Figure 2.2. The equation representing the assumed trough shape is as follows:

$$\delta = \delta_{\max} \exp\left(-\frac{x^2}{2i^2}\right) \quad (2.6)$$

where  $\delta$  is the surface settlement,  $\delta_{\max}$  is the maximum vertical settlement,  $x$  is the transverse distance from tunnel centerline, and  $i$  is the width of settlement trough, which is the distance to the point of inflection of the curve (corresponding to one standard deviation of the normal distribution curve), and is determined by the ground conditions.

In practice, the following relationship suggested by Rankin (1988) is often used:

$$i = k \cdot Z_0 \quad (2.7)$$

where  $k$  is a dimensionless constant, depending on soil type:  $k = 0.5$  for clay;  $k = 0.25$  for cohesionless soils,  $Z_0$  is the depth of the tunnel axis  $Z$  is shown in Figure 2.2 below ground level. Peck established a correlation between the relative depth of tunnel and the point of inflection of transverse surface settlement trough for various soil types.

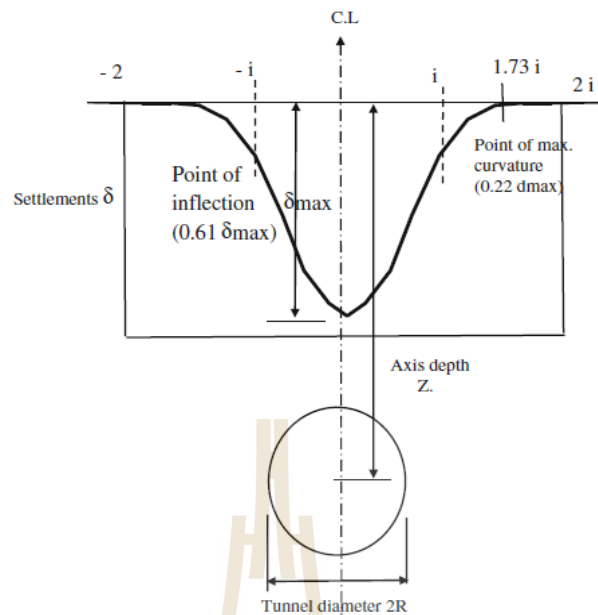


**Figure 2.2** Properties of error function curve to represent cross-section settlement trough above tunnel (Peck, 1969).

### 2.3 Numerical simulations for subsidence prediction

FLAC (Itasca, 1992) is a two dimensional explicit finite difference program for engineering mechanics computation. This program simulates the behavior of structures built of soil, rock or other materials that may undergo plastic flow when their yield limits are reached. Materials are represented by elements or zones, which form a grid that is adjusted by the user to fit the shape of the object to be models. Each element behaves according to a prescribed linear or nonlinear stress/strain law in response to the applied forces or boundary restraints. The material can yield and flow and the grid can deform (in large-strain mode) and move with the material that is represented. The explicit, Lagrangian calculation scheme and the mixed

discretization zoning technique used in FLAC ensure that plastic collapse and flow are modeled very accurately. Because on matrices are formed, large two-dimensional calculations can be made without excessive memory requirements. The drawbacks of the explicit formulation (i.e., small time step limitation and the question of required damping) are overcome to some extent by automatic inertia scaling and automatic damping that do not influence the mode of failure.

Though FLAC was originally developed for geotechnical and mining engineers, the program offers a wide range of capabilities to solve complex problems in mechanics. Several built-in constitutive models are available that permit the simulation of highly nonlinear, irreversible representative of geology, or similar, materials.

Shahriar et al. (2009) study the surface subsidence due to inclined very shallow coal seam mining of two underground coal mines by FLAC3D code which is based on finite difference method (FDM). FDM results are compared with measured profile and profile function method. FDM underestimated  $S_{\max}$  up to three per cent in comparison with surveying and profile function. The reason is that the residual subsidence is neglected in this research but the profile function method predicts final subsidence trough. Furthermore in both cases, FDM in contrast with measured profiles obtained by surveying and profile function method, predicted uplift over the panels rise side at the surface in which is confirmed by local observations. The reason that no uplift is observed in measured profile provided by Asadi et al. (2004, 2005). The position of  $S_{\max}$  in shallow coal seams shifted towards panel rise side which is totally in contrast with deep seam mining. Sensitivity analysis showed that by increasing the depth, this point gradually shifts toward the panel dip side (Figures 2.3

and 2.4). It was also found that critical width to depth ratio is between 1.0 and 1.4 for both panels. This range is a little lower than the range of critical W/H ratio which has been found by National Coal Board of UK (1975). This might be related to very low depth situation of both panels. Numerical methods can illustrate subsidence mechanism better than profile function due to taking into account the geomechanical material properties. Accordingly profile function results can hardly be extrapolated from one coal mining area to another, and even sometimes from panel to panel. Empirical methods have their own advantageous because of their simple and inexpensive applications.

For initial stress regimes with a high coefficient of lateral earth pressure at rest it has been shown by several studies that the transverse settlement trough predicted by (2D) finite element analysis is too wide when compared with field data. It has been suggested that 3D effects and/or soil anisotropy could account for this discrepancy.

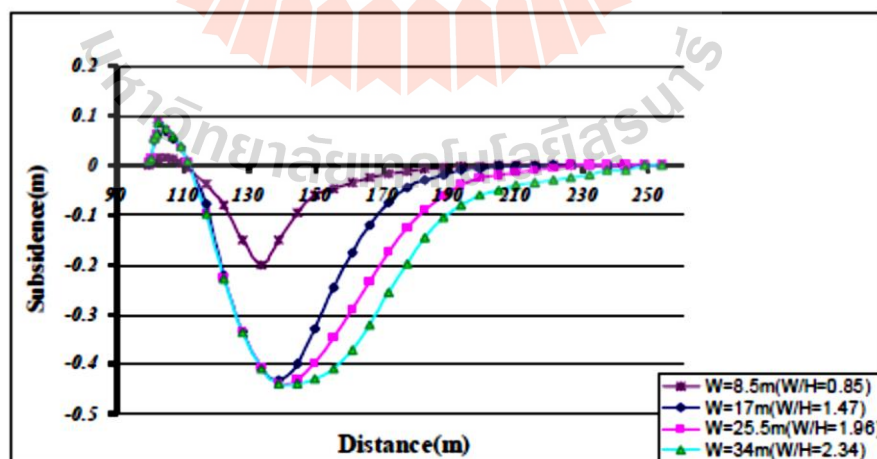


**Figure 2.3** Sensitivity analysis on panel width (Shahriar et al., 2009).

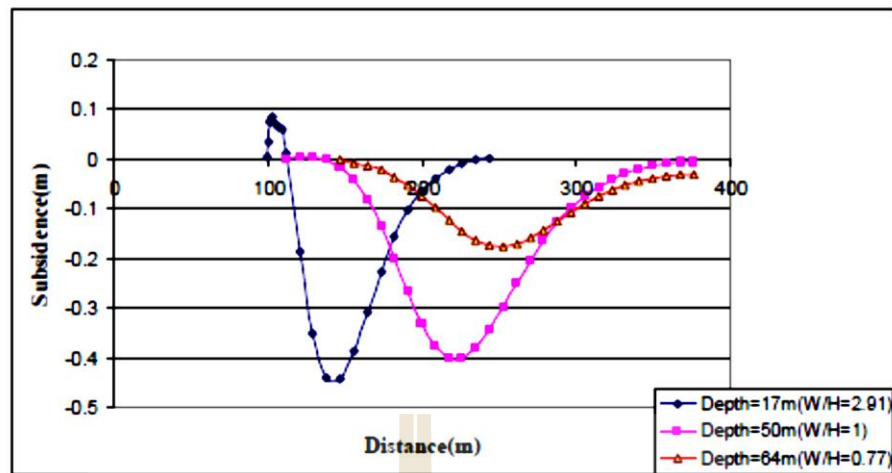


**Figure 2.4** Sensitivity analysis on seam depth (Shahriar et al., 2009).

Migliazza et al. (2009) study the surface subsidence from the extension of the Milan underground by using 3D finite element model (ABAQUS) with experimental subsidence measurements. Figure 2.5 presents the comparison between monitored and computed (FEM) surface vertical displacement at different distances from the tunnel face. It can be seen that even though the two diagrams have almost the same shape and the same intermediate and final values, there is a shift between an experimental and a numerical diagram. The computed vertical settlements reach the same values as those of the measured vertical settlements in a simulated advancing excavation phase, which is about 6 m ahead of the real excavation phase. The most probable reason for this difference is due to the pressure imposed in the FEM on the excavation wall in the shield area. Fifty Mega Pascal of radial pressure applied in the model to simulate fluid injection was evidently not measured in situ but represents the minimum pressure for allowing the numerical convergence of the FEM simulations.

Franzius et al. (2005) present a suite of both 2D and 3D FE analyses of tunnel construction in London Clay. Both isotropic and anisotropic nonlinear elastic pre-yield models were employed, and it was shown that, even for a high degree of soil anisotropy, the transverse settlement trough remains too shallow. By comparing longitudinal settlement profiles obtained from 3D analyses with field data, it was demonstrated that the longitudinal trough extends too far in the longitudinal direction, and that consequently, it is difficult to establish steady-state settlement conditions behind the tunnel face. Steady-state conditions are achieved only when applying an unrealistically high degree of anisotropy combined with a low- $K_0$  regime, leading to an unrealistically high volume loss.

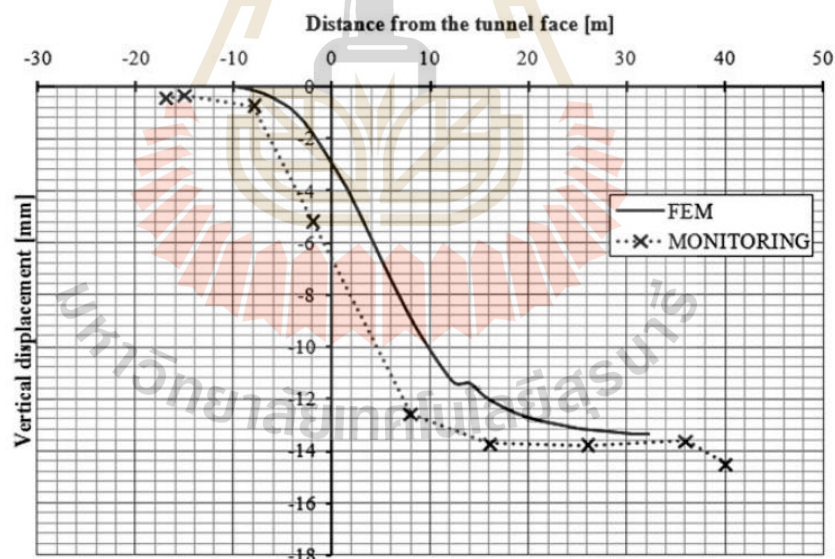


**Figure 2.5** Comparison between monitored and computed (FEM) vertical displacements corresponding to the tunnel section with a centerline depth of 11.5 m as a function of the distance from the tunnel face (Migliazza et al., 2009).

Ren and Li (2008) study the extent of mining subsidence affected area which is defined by the limit angles, which is predominantly controlled by geological conditions of the overburden strata and the mining configurations, including seam inclination angle. From observational data worldwide and numerical modeling analysis the following conclusions are drawn: The stiffness, strength and failure of the overburden play an important role in the characteristics of subsidence limit. When overburden rocks are sufficiently strong and no major failure or break up taking place in the roof, the limit angle would tend to be greater in roof rocks with higher stiffness. However, if the roof collapses, stronger strata would produce lower limit angle at the surface and weak roof strata would result in greater limit angle. When there is an adequately strong and stiff rock bed in the overburden, it is possible for a sub-critical subsidence profile to be developed over a panel of super-critical width. The rock strength and stiffness also affect the magnitude of the maximum subsidence. Generally the maximum subsidence over a strong overburden is less than that over a weak overburden. The finite element model represents a vertical section perpendicular to the longwall face with various extraction widths, as shown in Figure 2.6. The boundary conditions at the roof in the goaf area are prescribed by assuming that the roof is in contact with the floor after the extraction. A generalized elasto-plastic material using a Mohr-Coulomb failure criterion is assumed for the rock strata in the numerical analysis. A range of internal frictional angles and apparent cohesion values as the equivalent strength of the overburden strata are used to ensure that the models would not prematurely fail before reaching the prescribed boundary conditions. Numerical model is demonstrated that the effect of seam inclination is such that it increases the limit angle at the dip-side of the panel and



reduces the limit angle at the rise-side. The values of limit angles over inclined seams may be established from observed data set. Empirical relationship between the limit angles and the seam inclination angle may be derived either using numerical modeling techniques or observed data set in a specific mining field.

Dai et al. (2011) study the relationship between the unconsolidated layers thickness and surface movement by employed FLAC 3D. They found that the surface subsidence extends widely and the surface deformations are decreased with the increase of the unconsolidated layer thickness (Figure 2.7). This study is significant to predict surface subsidence of thick unconsolidated layers for coal mine and take effective measures to control surface subsidence.

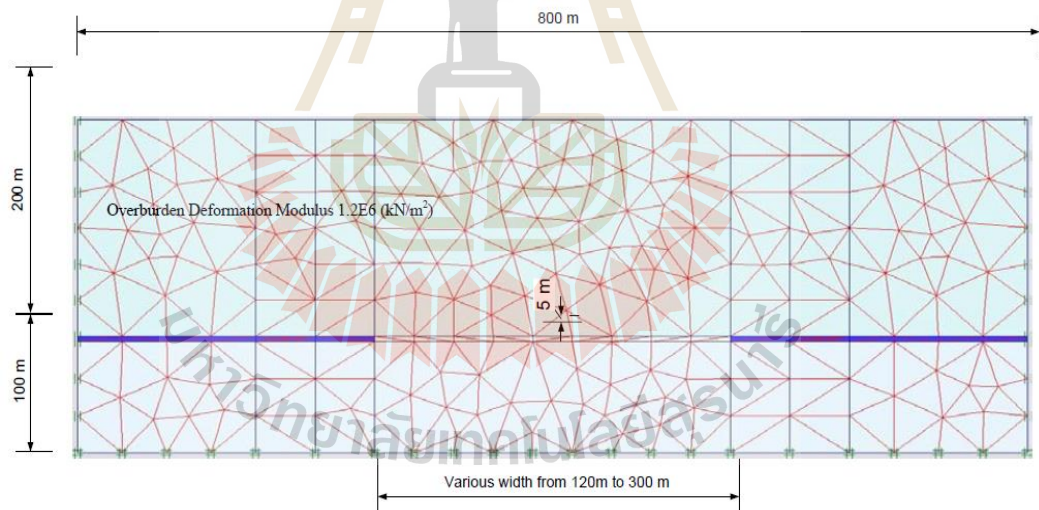


**Figure 2.6** Basic subsidence mesh and model dimensions (Ren and Li, 2008).

## 2.4 Similarity theory (Scale law)

Yavuz and Fowell (2003) study the mechanisms and the deformations of strata during mining operations. Success of the physical models to predict the strata behavior depends on satisfaction of the scaling requirements in modelling material used. The results from a laboratory work carried out into the factors influencing the strength and elastic properties of a physical model material to satisfy the scaling requirements determined from application of dimensional analysis to the pertinent variables affecting the deformation and failure of the underground structures.

A physical model is a representation of a section of disturbed ground (prototype) reproduced in the laboratory. This requires appropriate scaling of the body in terms of dimensions and strength. Relations between the parameters affecting

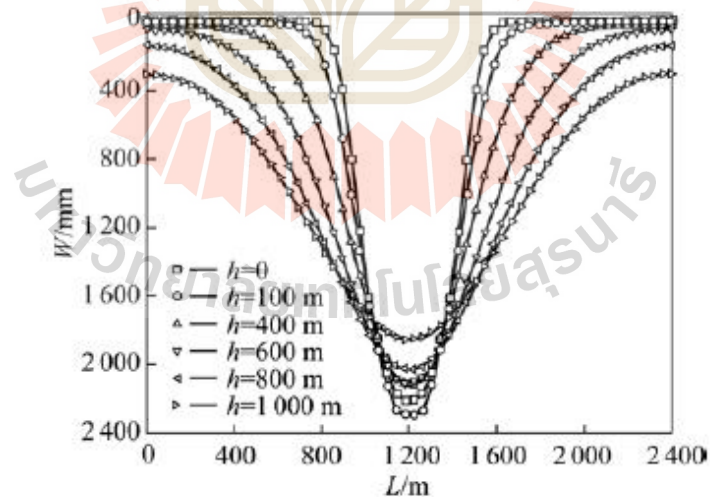


**Figure 2.7** Surface subsidence curves of different unconsolidated layers thickness

(Dai et al., 2011).

behavior of the prototype are established by using dimensional analysis. Dimensionless products obtained from dimensional analysis are related to the model by Buckingham's Pi theorem (Obert and Duvall, 1967).

The distance between two points in the model system ( $L_m$ ) must be a constant ratio to the corresponding points in the prototype ( $L_p$ ). The geometric scale factor ( $l$ ) is determined independently, and justified according to financial and laboratory constraints as follows:

$$L_m/L_p = l \quad (2.8)$$

From the application of the dimensional analysis to the pertinent variables affecting the deformation of the underground structures, the following dimensionless product was obtained:

$$S_p/\gamma_p l_p = 1 \quad (2.9)$$

where  $S_p$  is the strength of prototype,  $\gamma_p$  is the unit weight of prototype.

If this dimensionless product is referred to as the  $\pi_p$  term for the prototype and  $\pi_m$  for the model,  $\pi_p$  should be equal to  $\pi_m$  according to Buckingham's Pi theorem.

The strength scale is found as follows:

$$S_m/S_p = (\gamma_m/\gamma_p)/(L_m/L_p) \quad (2.10)$$

Where subscripts m and p refer to model and prototype. Equation 2.10 can be expressed as:

$$S = \gamma \cdot l \quad (2.11)$$

where  $S$  is the strength scale factor and  $\gamma$  is the unit weight scale factor. Unit weight scale factor changes from simulation of one stratum to another because of the changing density of the strata. Therefore, an average density of the structures modelled could be employed.

The Poisson's ratio and angle of internal friction and ultimate strain by considering maximum yield point are dimensionless parameters and should be equal in model and prototype. The following dimensionless ratios (strength and modulus ratios) should be as close to each other as possible:

$$E_p/\sigma_{cp} = E_m/\sigma_{cm} \quad \text{and} \quad \sigma_{cp}/\sigma_{tp} = \sigma_{cm}/\sigma_{tm} \quad (2.12)$$

where  $\sigma_{cp}$  and  $\sigma_{cm}$  are compressive strengths of the prototype and model material,  $\sigma_{tp}$  and  $\sigma_{tm}$  are the tensile strengths of the prototype and model material and  $E_p$  and  $E_m$  are elasticity moduli of the prototype and model material.

Investigation of the impact of mining subsidence on surface structure can be done through the physical modelling. Four types of physical model can be identified following the size of the model: full-scale field tests, small-scale physical field tests, small-scale physical laboratory tests (1g) and, finally, small-scale centrifuge tests (Allersma, 1995). The small-scale physical model is adopted in the present study because of its benefits: size reduction, simplification and convenience, possible analysis of situations for which analytical models are too complex, and ultimately possible use of the experimental data as base for the validation of theoretical or numerical models (Wood, 2004). A summary of scale factors is given in Table 2.1. The factors listed symbolically under the heading 'general' indicate the fundamental linkage between the various modeling decisions that might be taken: these are the

**Table 2.1** Scale factors (Wood, 2004).

Scale factors			
Quantity	General	1g (laboratory)	ng (centrifuge)
Length	$n_l$	$1/n$	$1/n$
Mass density	$n_\rho$	1	1
Acceleration	$n_g$	1	$n$
Stiffness	$n_G$	$1/n^\alpha$	1
Stress	$n_\rho n_g n_l$	$1/n$	1
Force	$n_\rho n_g n_l^3$	$1/n^3$	$1/n^2$
Force/unit length	$n_\rho n_g n_l^2$	$1/n^2$	$1/n$
Strain	$n_\rho n_g n_l^3 / n_G$	$1/n^{1-\alpha}$	1
Displacement	$n_\rho n_g n_l^2 / n_G$	$1/n^{2-\alpha}$	$1/n$
Pore fluid viscosity	$n_\mu$	1	1
		or* $n^{1-\alpha/2}$	or* $n$
Pore fluid density	$n_{pf}$	1	1
Permeability (Darcy's Law)	$n_{pf} n_g / n_\mu$	1	$n$
		or* $1/n^{1-\alpha/2}$	or* 1
Hydraulic gradient	$n_\rho / n_{pf}$	1	1
Time (diffusion)	$n_\mu n_l^2 / n_G$	$1/n^{2-\alpha}$	$1/n^2$
		or* $1/n^{1-\alpha/2}$	or* $1/n$
Time (creep)	1	1	1
Time (dynamic)	$n_l (n_\rho / n_G)^{1/2}$	$1/n^{1-\alpha/2}$	$1/n$
Velocity	$n_g n_l (n_\rho / n_G)^{1/2}$	$1/n^{1-\alpha/2}$	1
Frequency	$(n_G / n_\rho)^{1/2} / n_l$	$n^{1-\alpha/2}$	$n$
Shear wave velocity	$(n_G / n_\rho)^{1/2}$	$1/n^{\alpha/2}$	1

\* scaling of pore fluid viscosity introduced in order to force identity of scale factors for diffusion time and dynamic time

ratios of model and prototype values. The particular factors listed under ‘1g (laboratory)’ and ‘ng (centrifuge)’ are the results of typical modeling choices.

Tunsakul et al. (2013) study the failure behavior of rock mass around gas storage cavern with physical model test. They use a series of scaled-down physical model test under normal gravity (1g). The physical model test are performed on synthetic rock samples with a 200 times scaled down geometry and properties. They designed the physical character of model test is a silo, 0.1 meter in diameter, 0.2 meter high and the location of the cavern center is 0.5 meter under the ground surface. The rocks are simulated from mixture of plaster, sand and water. The test arrangement is shown in Figure 2.8. They conclude that the lateral earth pressure coefficient at rest, in-situ stress ratio has strong influence on the position of the initial points as obtained by numerical analyses.

Heib et al. (2013) present a small-scale physical model to study the soil structure interaction effect of large vertical displacement owing to underground mines. The soil used in the physical model is Fontainebleau sand. The simple masonry structure was built using different materials: polycarbonate, silicone, wood

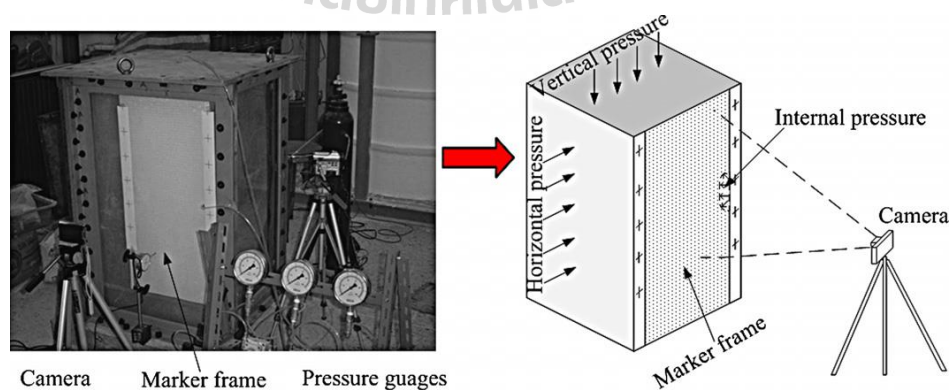


**Figure 2.8** Experimental setup (Tunsakul et al., 2013).

and sugar (Figure 2.9). The apparatus enables the effect at the ground surface of the failure of the typical case of a mine located 20 m below ground level with a  $10 \times 10$  m<sup>2</sup> cross-sectional area of extraction to be reproduced with a scale factor of 1/40. The result shows that the damages to the structure are located clearly in the zone of maximum tilt. The open cracks in the structure model made of sugar blocks are more than the ones in the model made of wood blocks perhaps owing to the differing dimensions of the blocks and the friction angle between blocks. With either type of block, it is possible to determine during the subsidence the location and the size of damages in masonry structures.

Ghabraie et al. (2015) study the mechanisms of multiple-seam subsidence by using small scale physical models. Due to the difference in scale between coal fields and laboratory experiments, the similarity theory is used. A mixture of sand-plaster and water is chosen to be used for the physical modelling. The mixtures has been tested and its strength parameters with the prototype rock mass properties are shown in Table 2.2. The physical dimensions are 200 cm long, 52 cm high and 15 cm thick.

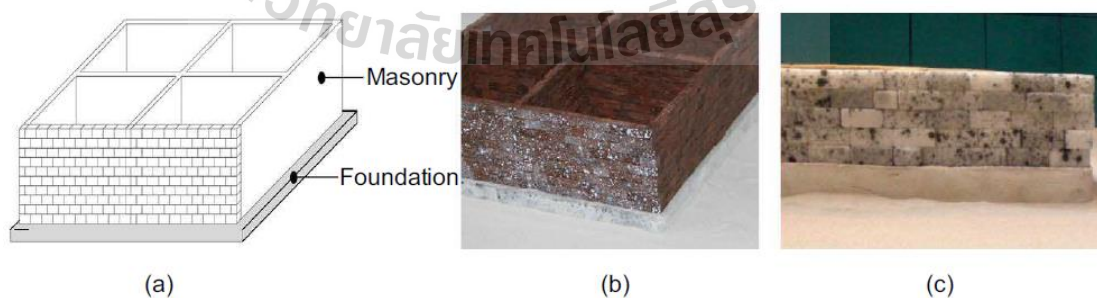


**Figure 2.9** Small-scale model of masonry structure (wood or sugar blocks) and foundation (silicon): (a) model; (b) wood; (c) sugar (Heib et al., 2013).

**Table 2.2** Similarity theory constants (Ghabraie et al., 2015).

	<b>Density (kg/m<sup>3</sup>)</b>	<b>Uniaxial compressive strength (MPa)</b>	<b>Geometry (m)</b>
Prototype case	2700	16700	150
Physical model	1909	52	0.66
Similarity theory	$C_\rho = 1.41$	$C_\sigma = 319.5$	$C_L = 1/226$

\*  $C_\rho$  = constant of density similarity,  $C_\sigma$  = constant of strength similarity and  $C_L$ = constant of geometry similarity

The displacements within the models are measured using combination of optical transducers, photogrammetry and laser scanning. The results are compared with finite element models. The incremental subsidence and substrata movement profiles after lower seam extraction can be separated into three different zones (Figure 2.10). These zones undergo different horizontal and vertical movement characteristics.

Ren et al. (2010) conduct a series of 1g small-scale physical model to determine the parameters of the subsidence. Bachmann et al. (2006) performs a three-dimensional physical modelling of large-scale gravitational rock mass movements. Analogue materials and original experimental gravity loading device, allowing tests to be carried out in compliance with the different scaling laws.



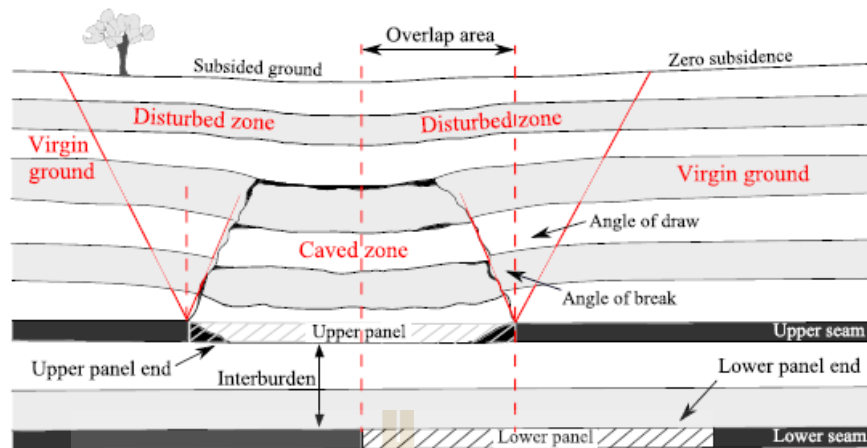


**Figure 2.10** Angles of draw and break and terminology for referring to different areas around first and second extractions (Ghabraie et al., 2015).

## 2.5 Physical modeling

Terzaghi (1936) used a model, characterized as the trap-door model. He explained the arching theory based on the translation of a trap door into the soil (passive mode) or away from it (active mode), as shown in Figure 2.11. The passive mode can be used to evaluate of the uplift force of anchors and other buried structures that can be idealized as anchors. The active mode can be used to study the silo problem or the earth pressure on a tunnel lining. According to this model, the deforming arch of a tunnel can be investigated by a downward moving trap-door while the soil above the tunnel can be represented by a layer of granular or slightly cohesive soil. Based on this simple model, the evolution of the mean vertical pressure acting on the trap-door during its downward movement can be studied. The physical model allowed him to represent a case study and to determine it completely with a limited set of parameters.

Following from Terzaghi's work, several researchers conducted 1g trapdoor tests using either aluminum rods or dry to simulate the response of granular materials to trap door displacement under plane strain conditions.

Fuenkajorn and Archeeploha (2009) develop an analytical method to predict the location, depth and size of caverns created at the interface between salt and overlying formations. A governing hyperbolic equation is used in a statistical analysis of the ground survey data to determine the cavern location, maximum subsidence, maximum surface slope and surface curvature under the sub-critical and critical conditions. A computer program is developed to perform the regression and produce a set of subsidence components and a representative profile of the surface subsidence under sub-critical and critical conditions. Finite difference analyses using FLAC code correlate the subsidence components with the cavern size and depth under a variety of strengths and deformation moduli of the overburden. Set of empirical equations correlates these subsidence components with the cavern configurations and overburden

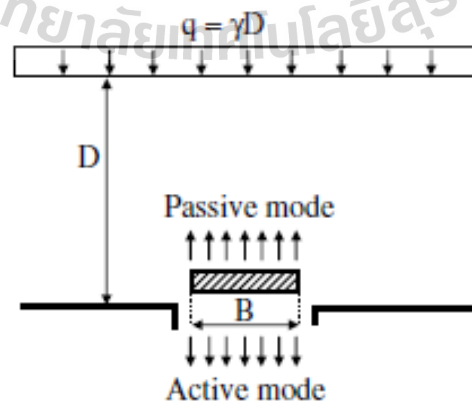


**Figure 2.11** Classical trap door problem (Terzaghi, 1936).

properties. For the super-critical condition a discrete element method (using UDEC code) is used to demonstrate the uncertainties of the ground movement and sinkhole development resulting from the complexity of the post-failure deformation and joint movements in the overburden. The correlations of the subsidence components with the overburden mechanical properties and cavern geometry are applicable to the range of site conditions specifically imposed here (e.g., half oval-shaped cavern created at the overburden-salt interface, horizontal rock units, flat ground surface, and saturated condition). These relations may not be applicable to subsidence induced under different rock characteristics or different configurations of the caverns. The proposed method is not applicable under super-critical conditions where post-failure behavior of the overburden rock mass is not only unpredictable but also complicated by the system of joints, as demonstrated by the results of the discrete element analyses. The proposed method is useful as a predictive tool to identify the configurations of a solution cavern and the corresponding subsidence components induced by the brine pumping practices (Figure 2.12).

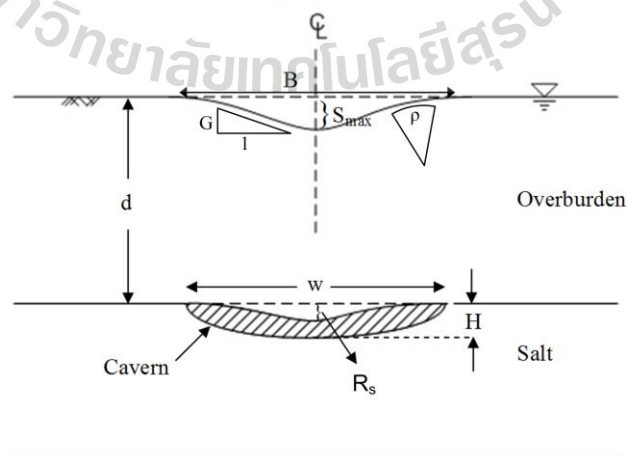


**Figure 2.12** Variables used by Fuenkajorn and Aracheeploha (2009).

Meguid et al. (2008) present the physical models that have developed and used in soft ground tunneling research. Physical modeling of soft ground tunnels is an essential part of the analysis and design of tunnels. Physical models can provide data that can validate and calibrate numerical models. For several decades, numerous researchers around the world have developed and implemented a variety of techniques to simulate the tunnel excavation process. Reduced scale tests under 1g conditions provide full control over the excavation method. However, they do not accurately simulate the in situ stress conditions. Centrifuge testing makes a more realistic simulation of in-situ stresses possible but the tunnel construction process has to be simplified. Different methods have been developed to simulate the process of tunnel construction in soft ground. Soil arching around excavated tunnels has been successfully simulated using the trap door method. Vertical stresses as well as surface displacements can be investigated by lowering a trap door under 2D or 3D conditions. Stability of the tunnel face can be investigated using a rigid tube with flexible membrane at the face. Tunnel excavation is simulated, in this case, by reducing the air pressure inside the tunnel and monitoring the soil movements. Other methods include the dissolvable polystyrene core showed some success; however, the tunneling induced surface settlement is not uniform. In addition test results were less satisfactory when the excavation is made under water. Techniques based on hand or mechanical augering to represent tunnel excavation and progressive face advance seem more realistic, however, mechanizing the test in the centrifuge is very expensive.

Park et al. (1999) conduct a series of 1g trap door experiments to investigate the response of inclined layers to tunnel excavations. The tested material consisting

of aluminum rods (unit weight =  $21.1 \text{ kN/m}^3$  and friction angle =  $30^\circ$ ) and aluminum blocks (unit weight =  $26.4 \text{ kN/m}^3$  and friction angle =  $20^\circ$ ) is arranged in layers making angles,  $\theta_1$ , of  $30^\circ$ ,  $60^\circ$ , and  $90^\circ$  with the horizontal. The setup composed of 40 supporting blocks, 2.45 cm in width arranged over a supporting plate installed along the base of the apparatus (Figure 2.13). Forty load cells were installed between each supporting block and the supporting plate so that the distribution of earth pressure on the trap door can be measured. The interaction between two adjacent blocks is avoided by setting the spacing at 0.05 mm. The tunneling process is simulated by lowering the trap door using a control jack. Figure 2.13 shows an example of the surface settlement profiles induced by lowering the trap door 2 mm for different layer inclination angles and overburden pressures. The inclination angle is found to have a significant effect on the surface settlement trough. Symmetrical settlement profiles are observed for the vertically arranged blocks ( $\theta_1 = 90^\circ$ ). For the  $\theta_1 = 30^\circ$ , the maximum surface settlement shifted towards a direction normal to the layer inclination angle (left of the trap door). Different behavior is found for the case of  $\theta_1 = 60^\circ$  where the maximum surface settlement shifted in the direction of the layer inclination angle (right of the trap door).

Adachi et al. (2003) investigate the 3D effect of the trap door system on the induced pressure and surface settlement under 1g condition (Figure 2.14). The soil used is silica sand No. 6 with friction angle of  $36^\circ$ . For a given overburden pressure and a trap door displacement the earth pressure measured around the 2D trap door is found to be greater than that measured around the 3D trap door tests.

The base friction method has been used to reproduce the effect of gravity and visualize displacements in 2D physical models of mainly rock tunnels. Gravity is simulated by the drag of a belt moving along the model base. The method allows one

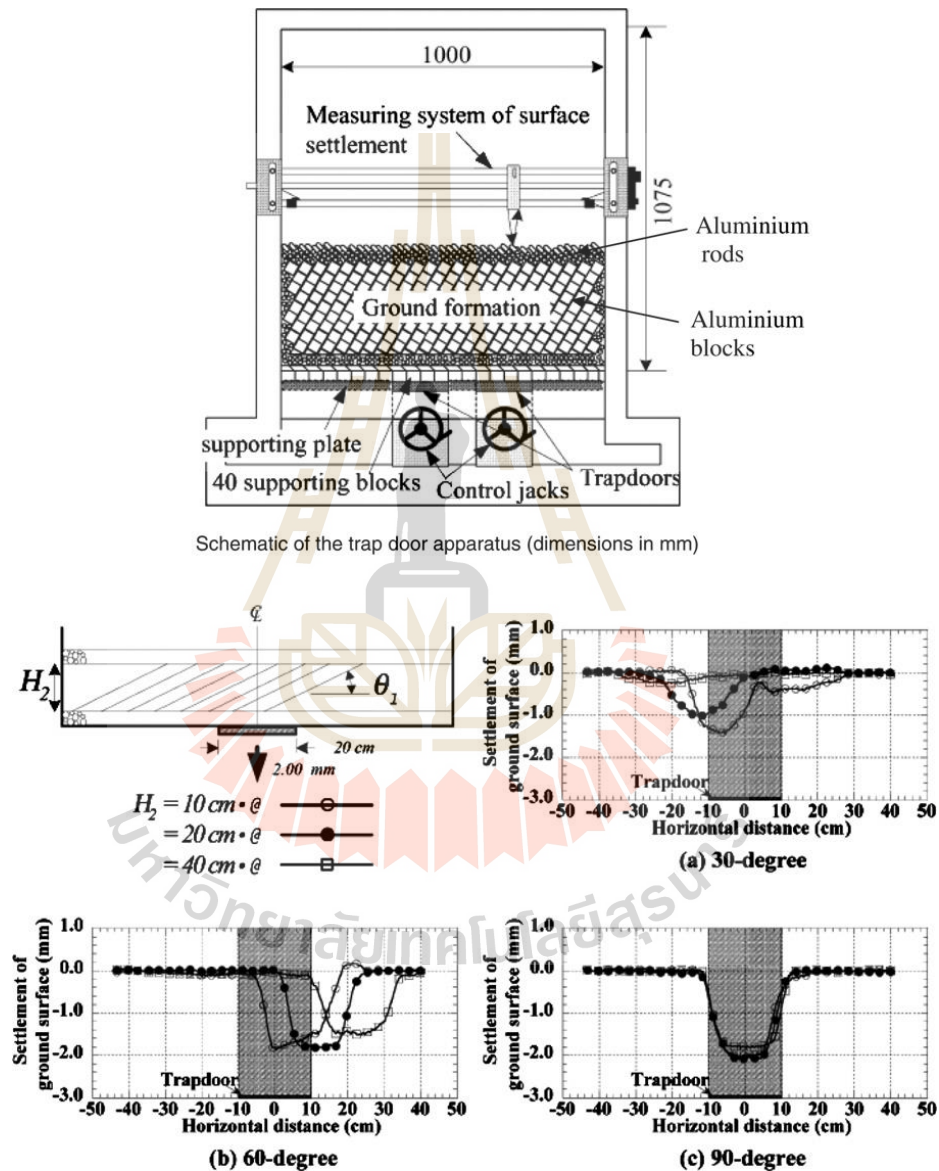


**Figure 2.13** Surface settlement measured for applied displacements of 1 mm and 4 mm (Park et al., 1999).

to visually observe the ground movement and the failure mechanisms resulting from tunnel excavation.

A large scale 3D model of a tunnel heading has been developed by Sterpi et al. (1996). This 1g model (Figure 2.15) consists of a 1.1 m long, horse shoe shaped steel pipe, with width and height of 1.32 m and 1.145 m, respectively. A vinyl bag is inserted within the pipe and air pressure is applied to support the tunnel face. The pluviial deposition technique is adopted to fill the container with medium uniform sand (friction angel =  $32^\circ$ ) leveled in layers of constant thickness (about 30 cm). Figure 2.15 shows the failure pattern resulting from air pressure reduction at the tunnel face.

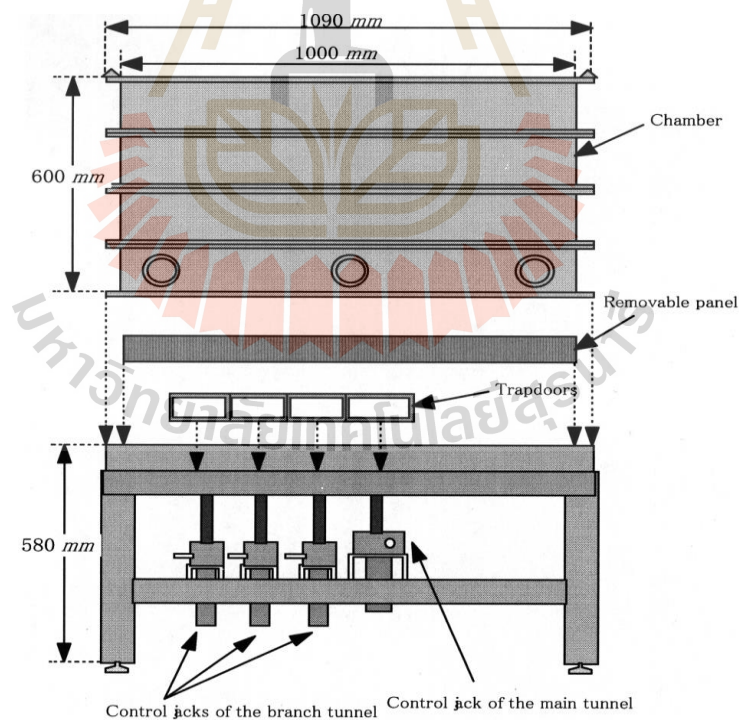


**Figure 2.14** Three-dimensional trapdoor tester (side view) (Adachi et al., 2003).

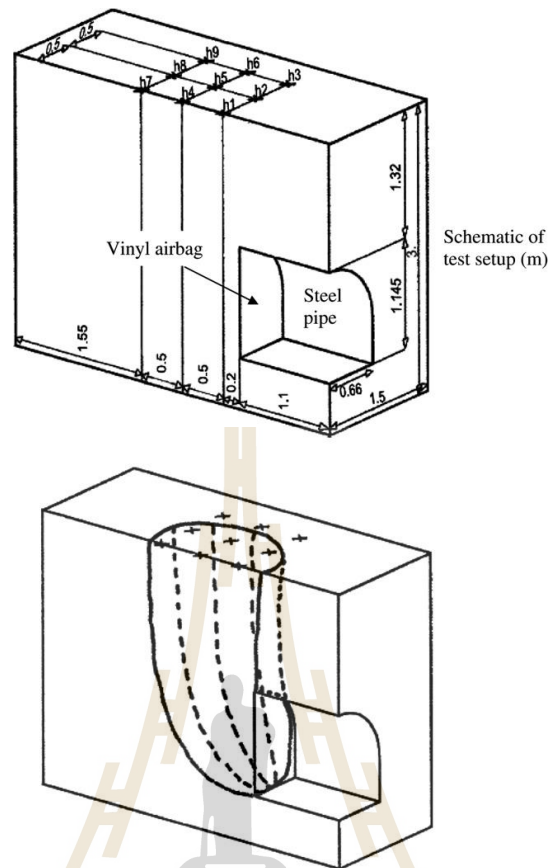
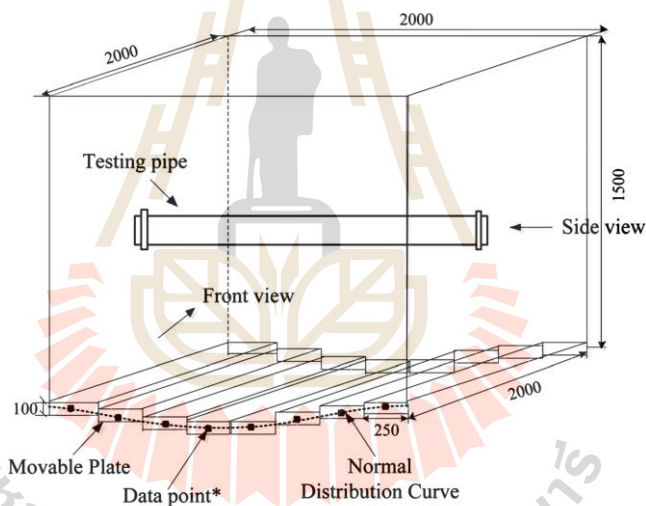


**Figure 2.15** Test setup and failure mechanism (Sterpi et al., 1996).

Wang et al. (2015) study the effects of the existence of the service pipelines on the ground movement induced by tunneling. The system included a model box, a pipe fixing frame, and a number of settlement plates (Figure 2.16). The plates are lowered down at four levels of maximum vertical distance (10, 20, 30, and 40 mm) to form normal distribution curves, simulating tunneling effects in the sand stratum. Four normal distribution curves are created with maximum lowering distances of the movable plates of 10, 20, 30, and 40 mm to simulate different volumes of ground loss in the tunnel. Prior to filling, the required density of backfilled sand is determined using a self-designed instrument. The HDPE pipes, with two diameters, are installed



in the model box at two different buried depths using a custom-made fixing frame. The test results demonstrate that the existence of the HDPE pipes resulted in a wider but shallower settlement trough than in the greenfield (without pipe) case. The width of the settlement trough at a given depth decreased with decreasing buried depth of the pipe, whereas it increased with decreasing pipe diameter. The volume of the settlement trough at a given depth is approximately constant, regardless of the existence of pipes, and the vertical displacement of the pipes increased with decreasing diameter and buried depth of the pipe.



\* The lowering distance of the moveable plates in this study refers to the lowering distance of the data points.

**Figure 2.16** Schematic diagram of the model box (Wang et al., 2015).

## 2.6 Effect of underground opening geometries and overburden properties on surface subsidence

Yao et al. (1991) introduce an analytical calculation model for the angle of draw by the use of a finite element model proposed by Reddish (1989) at the Nottingham University. They studied the influence of overburden strength and different rock mass properties, and the presence of a distinct bed, on subsidence limit characteristics. Their results show that the angle of draw is related to the overburden properties, depth and configurations of the mine openings. Five cases have been studied in order to investigate the effect of different rock mass properties on the angle of draw. The relationship between the percentage of maximum subsidence and the relevant angle of draw for each case has been examined. The results show that increasing the strength of the cover rock mass reduces the angle of draw (Figure 2.17).

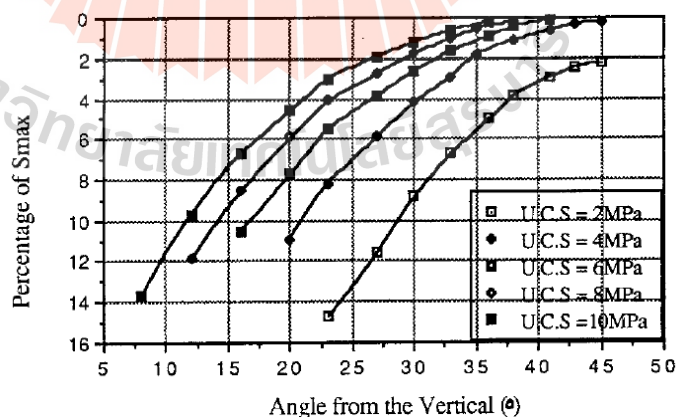


**Figure 2.17** Effect of different overburden properties on the angle of draw (Yao et al., 1991).

For the effect of strong and weak beds in the overburden on the angle of draw, it can be seen that the weak bed in the overburden increases the angle of draw. Additionally, it is also important to note that a decrease in the uniaxial compressive strength in the weak bed causes a significant increase in the angle of draw. However, it seems that with an increase in the uniaxial compressive strength of the strong bed, the angle of draw decreases only slightly.

Cai et al. (2014) propose some improvements to the original influence function method to take the topography influence on subsidence due to horizontal underground mining into account. The original influence function method is well adapted for predicting subsidence induced by the extraction of horizontal stratiform layer from an underground mine beneath a flat surface, but provides improper results when the surface is not flat. Therefore, new asymmetrical influence functions have been suggested to compute the vertical and horizontal element subsidence. They are based on the probability density functions of normal distributions corrected by complementary error functions. The parameters of these asymmetrical influence functions can be described by the surface dip angle and mean mining depth, meaning that the new influence functions take topographic variations into account. Full scale subsidence can then be computed using the new functions according to a standard summation method. This improved influence function method can take the known expected maximum subsidence and influence angle obtained from field data into account. Some other parameters can also be adjusted from surveying subsidence data to enhance the computational precision.

Thongprapha et al. (2015) study the effects of underground opening configurations on surface subsidence under super-critical conditions. A trap door apparatus has been fabricated to perform the scaled-down simulations of surface subsidence. Clean gravel is used to represent the overburden in order to exhibit a cohesionless behavior. The effects of opening length ( $L$ ) and opening height ( $H$ ) are assessed by simulating the  $L/W$  from 1, 2, 3, 4 to 5 and  $H/W$  from 0.2, 0.4, 0.6, 0.8 to 1, where  $W = 50$  mm. The effect of opening depth ( $Z$ ) is investigated here by varying  $Z/W$  from 1 to 3 to 4. The results indicate the angle of draw the maximum subsidence and the volume of trough are controlled by the width, length, height and depth of the underground openings. The angle of draw and maximum subsidence increase with increasing  $L/W$  ratio and tends to approach a limit when  $L/W$  equals 3. For the same  $L/W$  ratio and  $H/W$  ratio, increasing the  $Z/W$  ratio reduces the angle of draw and maximum subsidence. The volume of subsidence trough observed from the physical model is always less than the opening volume (Figure 2.18). This is due to settlement in the physical model has created new voids above the opening. However, the subsidence trough volume tends to decrease as the opening depth increases, particularly for short opening.

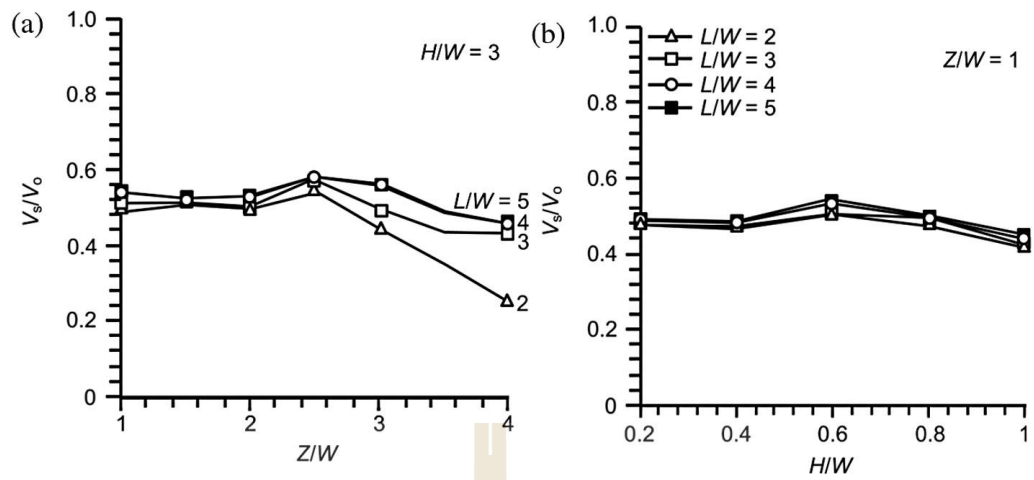


**Figure 2.18** Volumetric ratio of trough volume to excavation volume ( $V_s/V_o$ ) as a function of opening depth ratio  $Z/W$  (a) and opening height ratio  $H/W$  (b) for four values of length to width ratio  $L/W$  (Thongprapha et al., 2015).

## **CHAPTER III**

### **MATERIAL PREPARATION**

#### **3.1 Introduction**

This chapter describes the material used to simulate overburden in the physical model simulations. The types of material used in this study are elastic materials (synthetic gel mixed with paraffin wax). These materials are used to simulate the settlement of overburden under sub-critical condition. The materials are subjected to uniaxial compression testing. Their mechanical properties are used as parameters in the computer simulations.

#### **3.2 Overburden simulator**

The main factor of the material used to simulate the overburden is universally obtainable and non-toxic. The physical properties of the overburden are independent of the variations of temperatures and humidity. The mixing ratio of these materials are varied to obtain 3 different properties.

Figure 3.1 shows the synthetic gel mixed with paraffin wax under the temperature of 60°C in the oven, and then poured into the PVC pipe with size of 12.5 mm diameter and 25.4 mm length. After cooling down to 32°C the gel becomes semi-solid (Figure 3.2). The synthetic gel to paraffin wax ratios range from 100:0 to 50:50 by weight. The uniaxial compression test is performed to determine the elastic modulus and Poisson's ratios of the gel by using universal testing machine (UTM)



**Figure 3.1** Synthetic gel mixed with paraffin under 60°C.

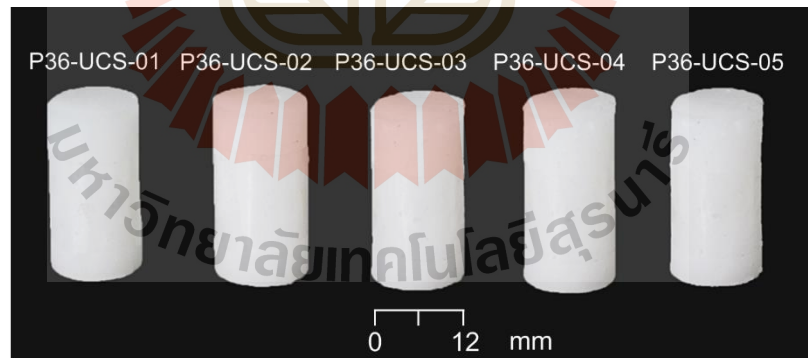


**Figure 3.2** Some gel specimens prepared for uniaxial compression test.

(Figure 3.3). The test method and calculation follow the ASTM standard practice (ASTM D695-10, 2010). Table 3.1 summarizes the specimen number, dimensions, volume and density. The average density of gel specimens is  $0.99 \pm 0.01 \text{ g/cm}^3$ . Figures 3.4 through 3.8 show the stress-strain curves obtained the testing. Figure 3.9 shows the elastic modulus and Poisson's ratios under various different mixtures. The elasticity of the gels ( $E_m$ ) increases exponentially with the paraffin additive. The Poisson's ratios ( $\nu_m$ ) are however not sensitive to the paraffin content. The elastic modulus of 1, 3 and 5 MPa are selected in this study, primarily because they can be correlated with that of the Maha Sarakham formation in the mine area. The selected value corresponds to the Poisson's ratio of 0.35, 0.36 and 0.36, and the density of  $0.99 \text{ g/cm}^3$ .



**Figure 3.3** Gel specimen placed in a universal testing machine (UTM).



**Table 3.1** Specimen dimensions prepared for uniaxial compression testing.

<b>Specimen No.</b>	<b>Weight (g)</b>	<b>Diameter (mm)</b>	<b>Height (mm)</b>	<b>Volume (cm<sup>3</sup>)</b>	<b>Density (g/cm<sup>3</sup>)</b>
P10-UCS-01	3.05	12.49	25.42	3.11	0.98
P10-UCS-02	3.02	12.51	25.31	3.11	0.97
P10-UCS-03	3.06	12.48	25.54	3.12	0.98
P10-UCS-04	3.06	12.49	25.21	3.09	0.99
P10-UCS-05	3.04	12.52	24.89	3.06	0.99
P32-UCS-01	3.05	12.51	25.22	3.10	0.98
P32-UCS-02	3.07	12.52	25.31	3.12	0.99
P32-UCS-03	3.05	12.49	25.34	3.10	0.98
P32-UCS-04	3.00	12.48	25.41	3.11	0.97
P32-UCS-05	3.01	12.51	24.89	3.06	0.98
P36-UCS-01	3.05	12.48	25.31	3.10	0.99
P36-UCS-02	3.05	12.48	25.14	3.08	0.99
P36-UCS-03	3.10	12.51	25.41	3.12	0.99
P36-UCS-04	3.01	12.47	24.89	3.04	0.99
P36-UCS-05	2.98	12.50	24.89	3.05	0.98
P40-UCS-01	3.07	12.49	25.22	3.09	0.99
P40-UCS-02	3.08	12.50	25.31	3.11	0.99
P40-UCS-03	3.05	12.48	25.34	3.10	0.98
P40-UCS-04	3.03	12.49	24.89	3.05	0.99
P40-UCS-05	3.04	12.51	25.31	3.11	0.98
P45-UCS-01	3.06	12.50	25.34	3.11	0.98
P45-UCS-02	3.02	12.51	24.89	3.06	0.99
P45-UCS-03	3.02	12.48	24.89	3.04	0.99
P45-UCS-04	3.10	12.49	25.54	3.13	0.99
P45-UCS-05	3.05	12.51	25.22	3.10	0.98

**Table 3.1** Specimen dimensions prepared for uniaxial compression testing (cont.).

<b>Specimen No.</b>	<b>Weight (g)</b>	<b>Diameter (mm)</b>	<b>Height (mm)</b>	<b>Volume (cm<sup>3</sup>)</b>	<b>Density (g/cm<sup>3</sup>)</b>
P50-UCS-01	3.07	12.47	25.31	3.09	0.99
P50-UCS-02	3.06	12.50	25.34	3.11	0.98
P50-UCS-03	3.02	12.49	24.89	3.05	0.99
P50-UCS-04	3.07	12.50	25.22	3.09	0.99
P50-UCS-05	3.06	12.51	25.31	3.11	0.98
Average					0.99 ± 0.01

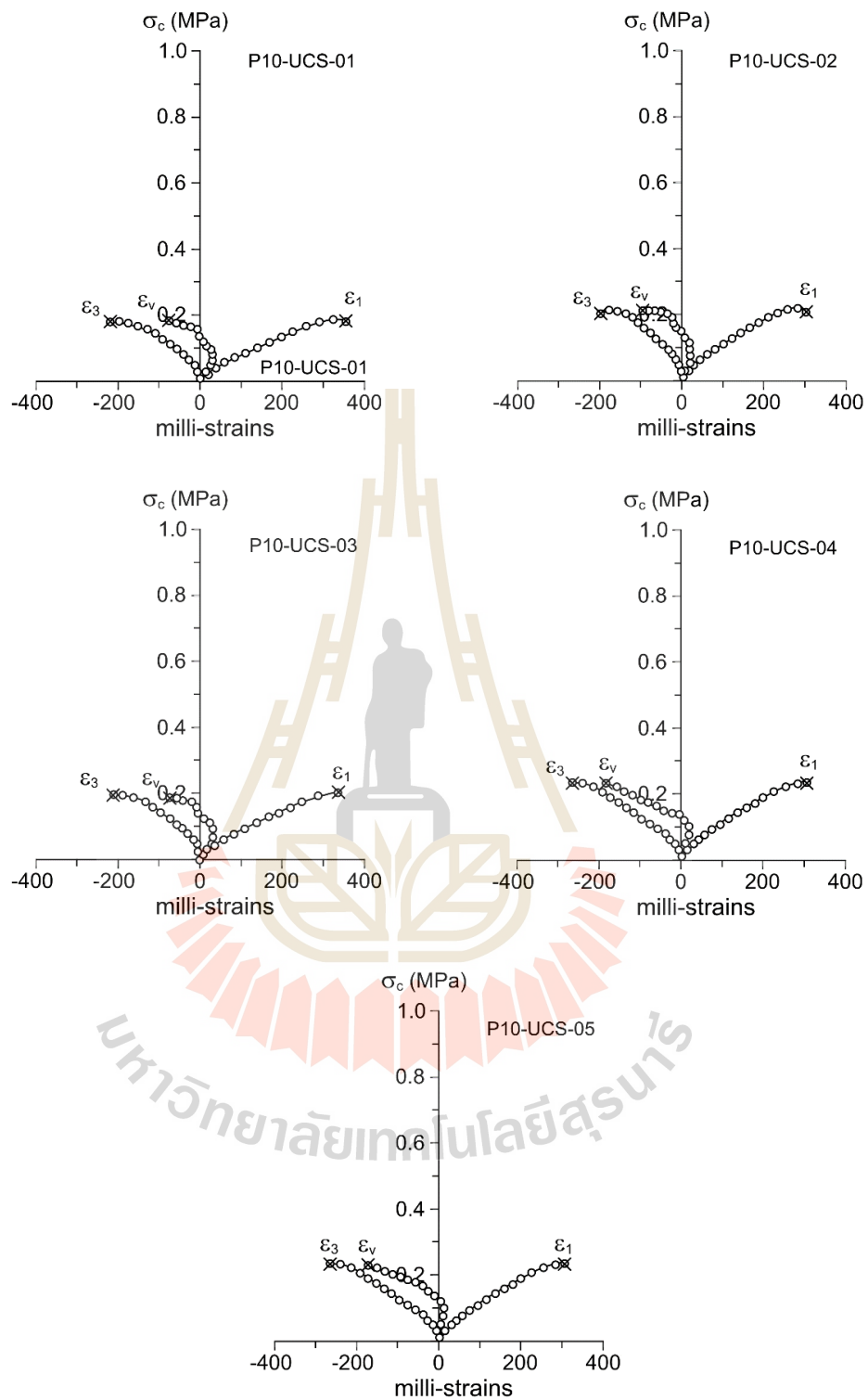


**Figure 3.4** Stress-strain curves obtained from gel specimens with paraffin contents 10% by weight.

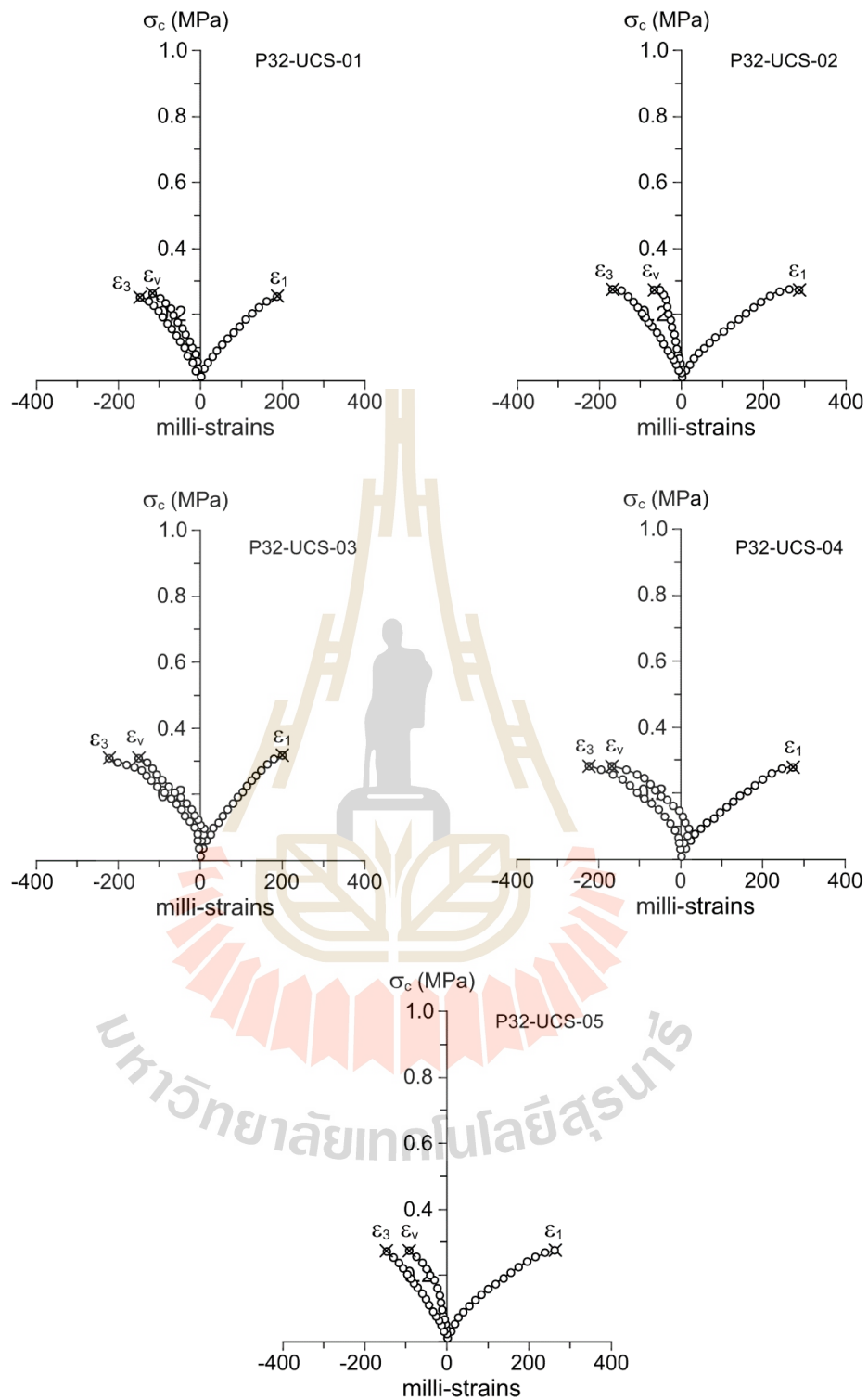


**Figure 3.5** Stress-strain curves obtained from gel specimens with paraffin contents 32% by weight.

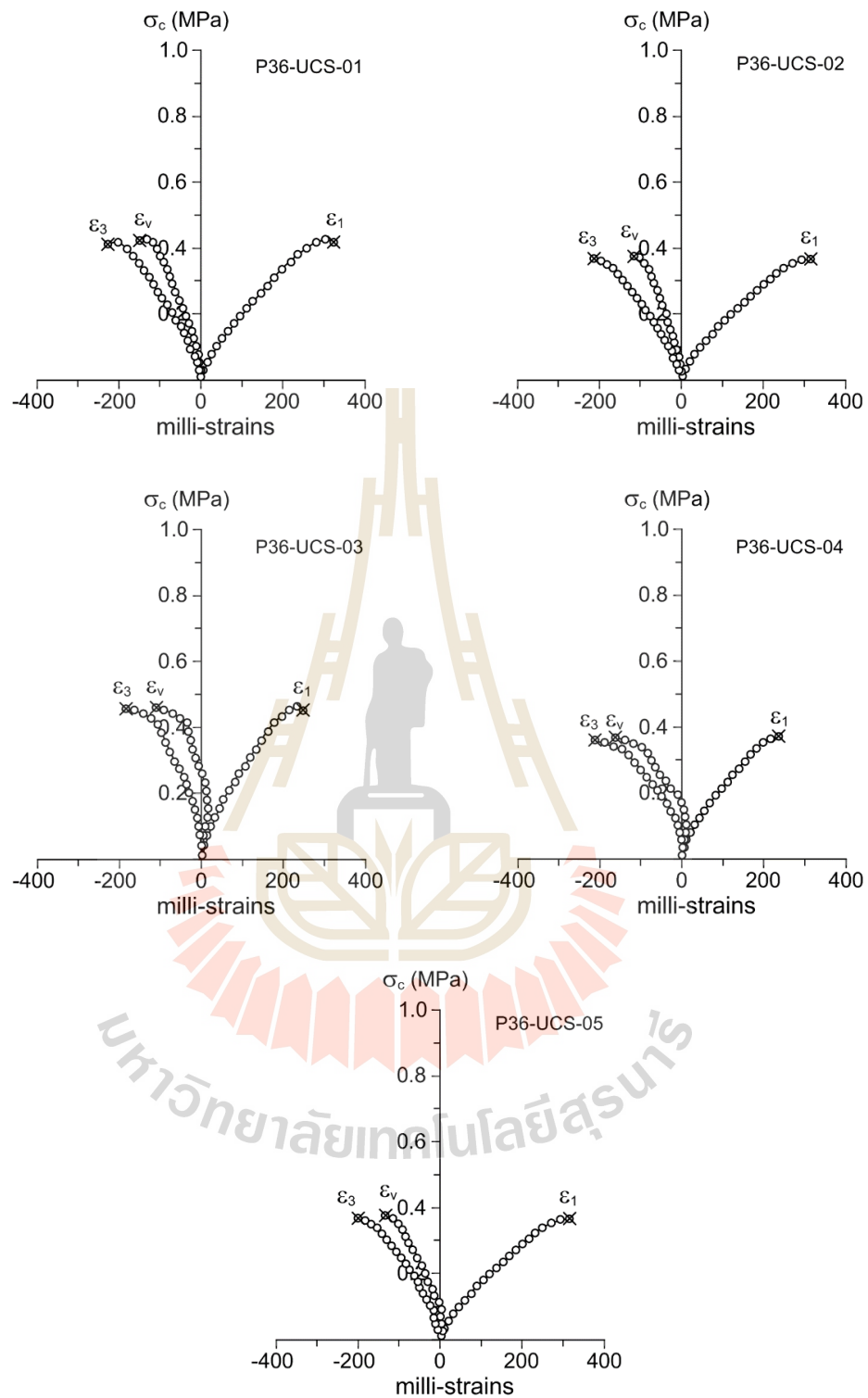


**Figure 3.6** Stress-strain curves obtained from gel specimens with paraffin contents 36% by weight.

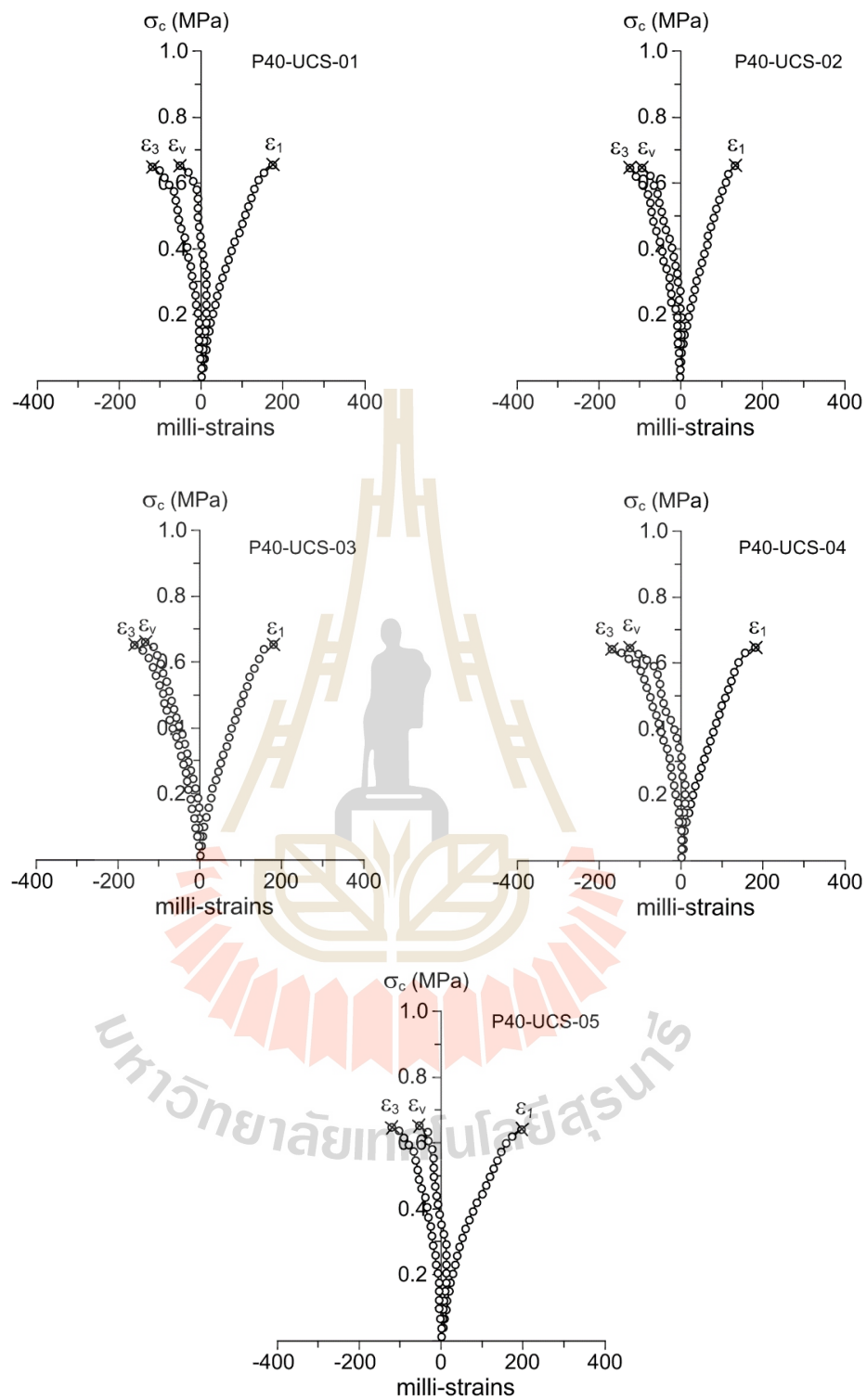


**Figure 3.7** Stress-strain curves obtained from gel specimens with paraffin contents 40% by weight.

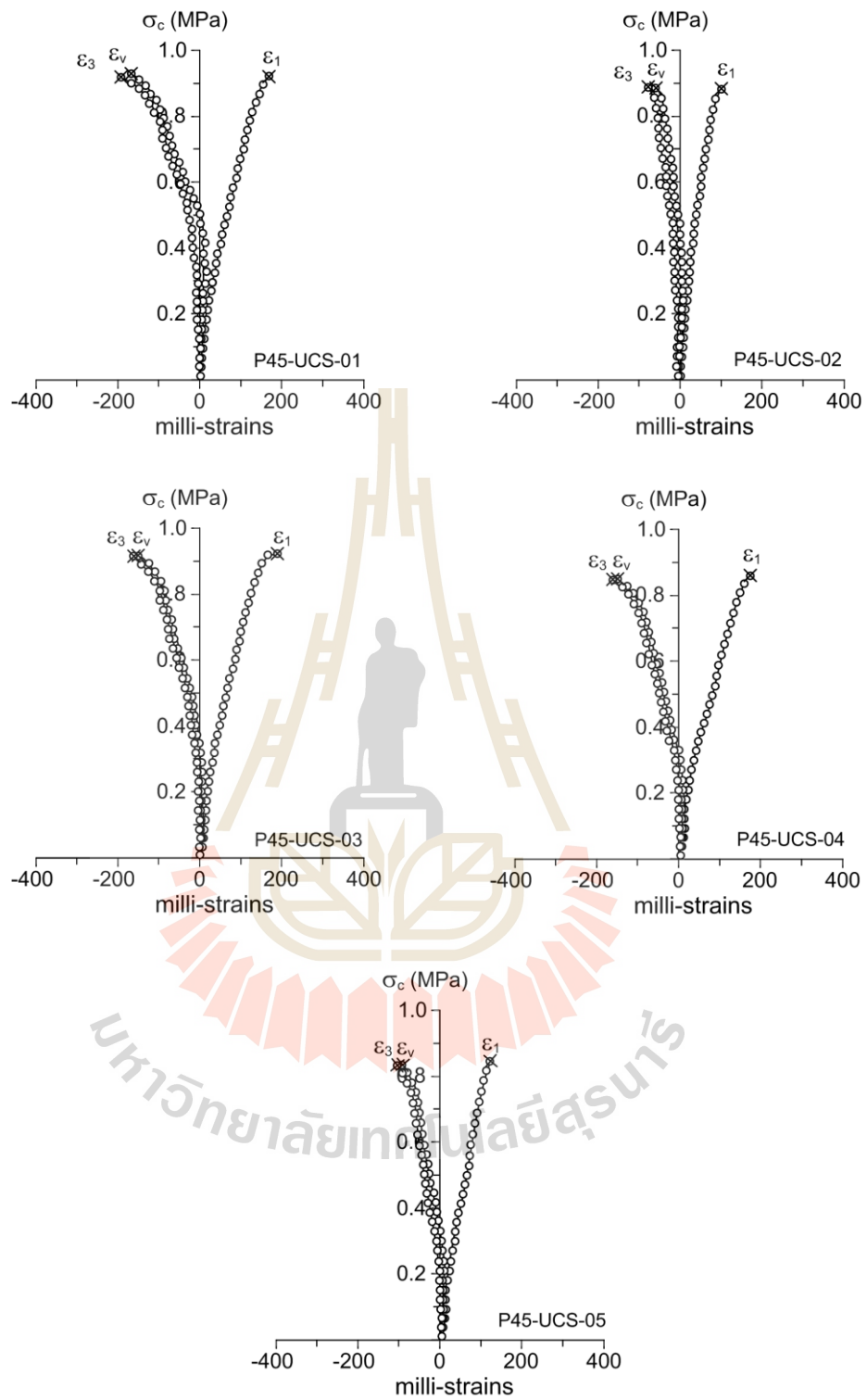


**Figure 3.8** Stress-strain curves obtained from gel specimens with paraffin contents 45% by weight.

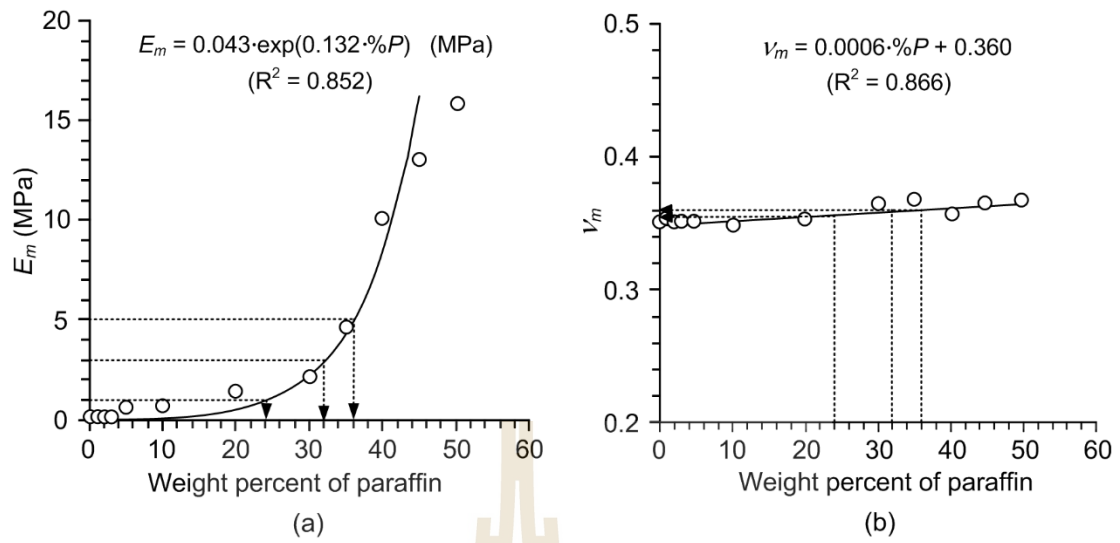


**Figure 3.9** Elastic modulus (a) and Poisson's ratio (b) of synthetic gel as a function of paraffin additive content.



## CHAPTER IV

### FABRICATION OF THE TEST FRAME

#### 4.1 Introduction

A trap door apparatus is used to simulate the surface subsidence as affected by the opening width and depth. This chapter describes the design requirements and components of the apparatus.

#### 4.2 Design and fabrication of the test apparatus

The functional requirements for the test frame are (1) to simulate subsidence of overburden in three-dimension, (2) to assess the effect of overburden properties and of the geometries of underground openings on the surface subsidence, (3) to observe subsidence of overburden in three-dimension, and (4) to induce subsidence of overburden using real gravitational force.

The apparatus (Figure 4.1) comprises three main components: the material container, the mine opening simulator, and the surface measurement system. A custom-made  $0.95 \times 0.95 \text{ m}^2$  clear acrylic plate with 15 mm thick is placed in the grooves of the square steel frame. Four acrylic sheets are secured with a steel plate at each side. The testing space is  $0.75 \times 0.75 \times 0.30 \text{ m}^3$ . The mine opening simulator is an array of plastic blocks (50 mm wide, 10 mm high and 200 mm long). These blocks are used to simulate the openings by first placing them above the surface of the material container. After the synthetic gel is installed, these blocks are

gradually and systematically moved down, and hence induces the vertical settlement of the gel above.

The measurement system includes a sliding rail with laser scanner. The laser scanner can be moved horizontally in two perpendicular directions. The precision of the measurements is one micron. The results are recorded and plotted in three-dimensional profiles. The maximum subsidence values, angles of draw, slopes and volume of the subsidence trough can be readily determined for each opening configuration. Figures 4.2 through 4.6 illustrate the schematic drawings of the test apparatus.

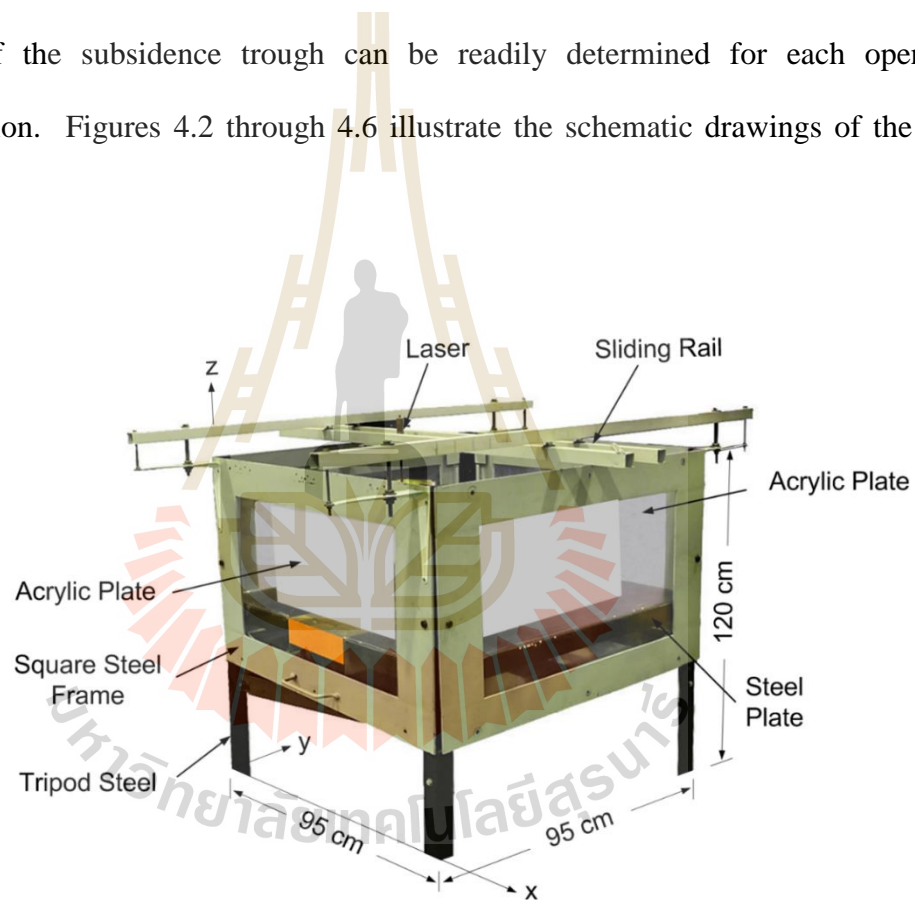


**Figure 4.1** Trap door apparatus used for physical model testing.

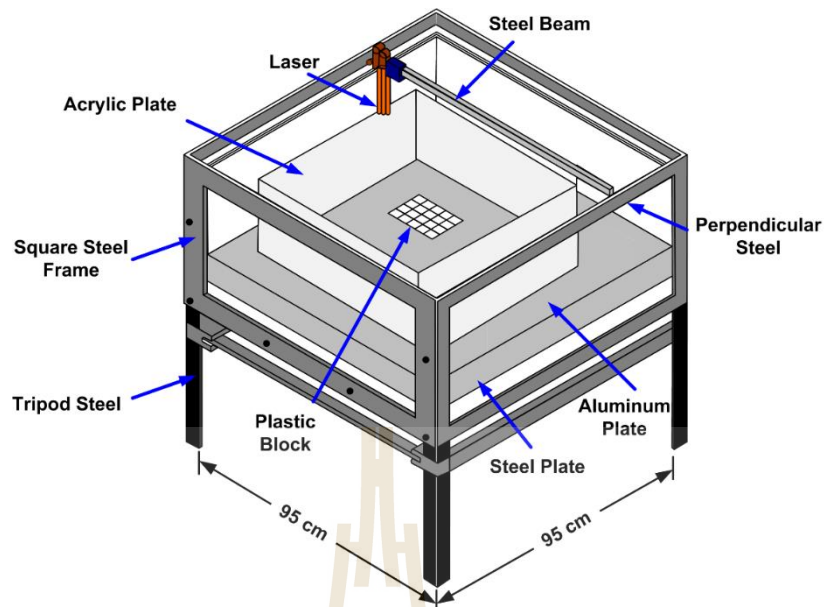


**Figure 4.2** Perspective view of trap door apparatus.

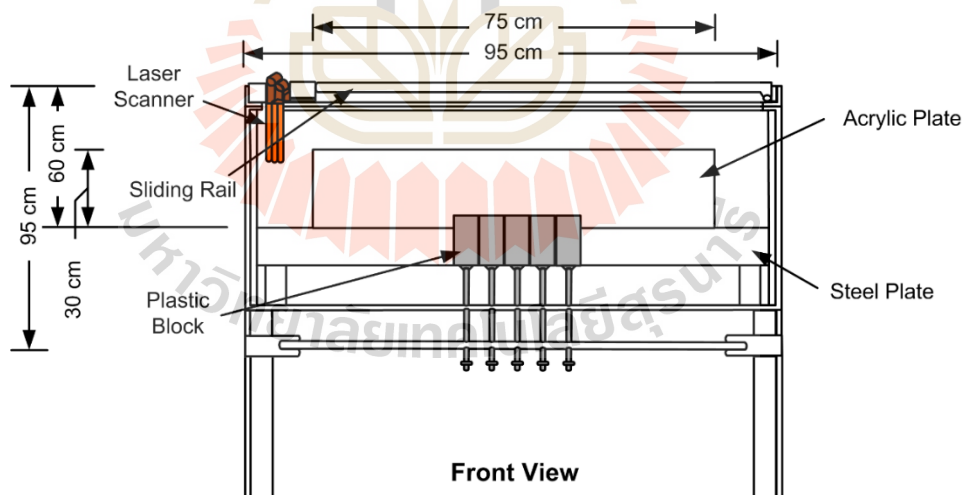


**Figure 4.3** Front view of trap door apparatus.

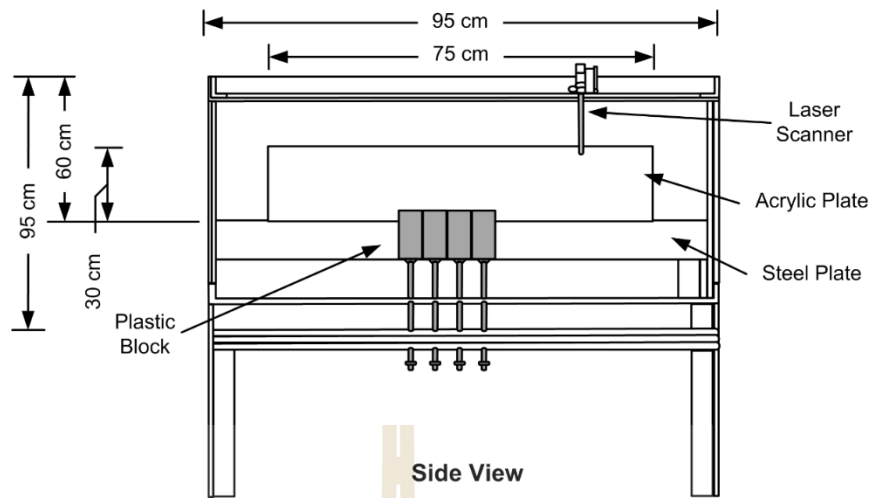


**Figure 4.4** Side view of trap door apparatus.

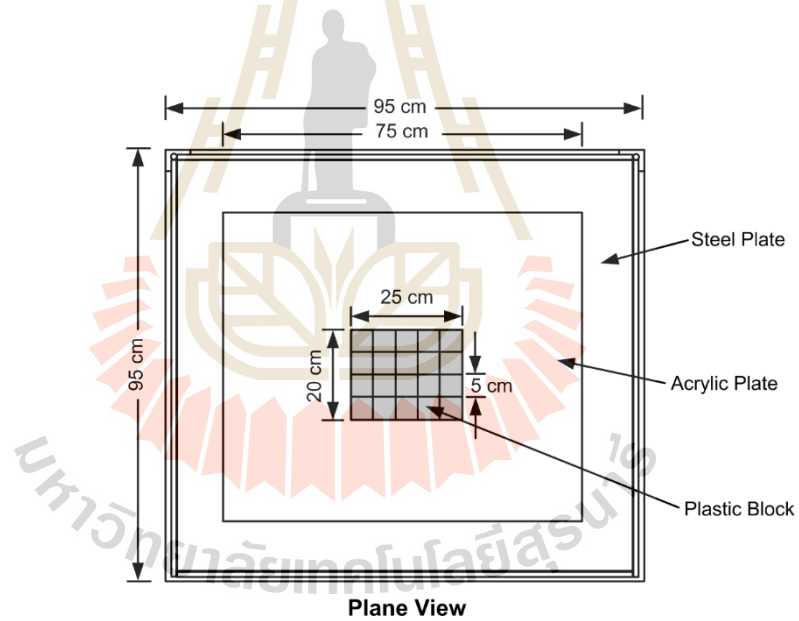


**Figure 4.5** Plane view of trap door apparatus.

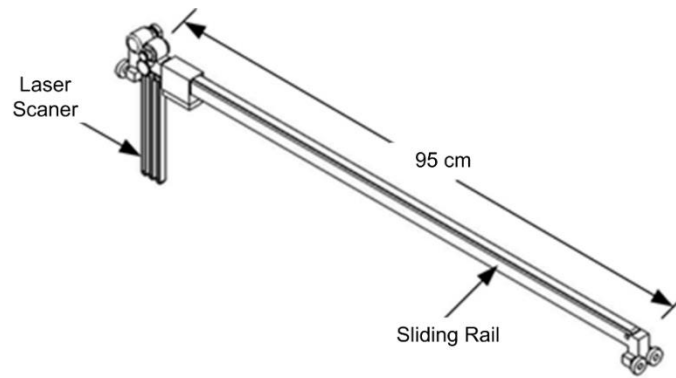
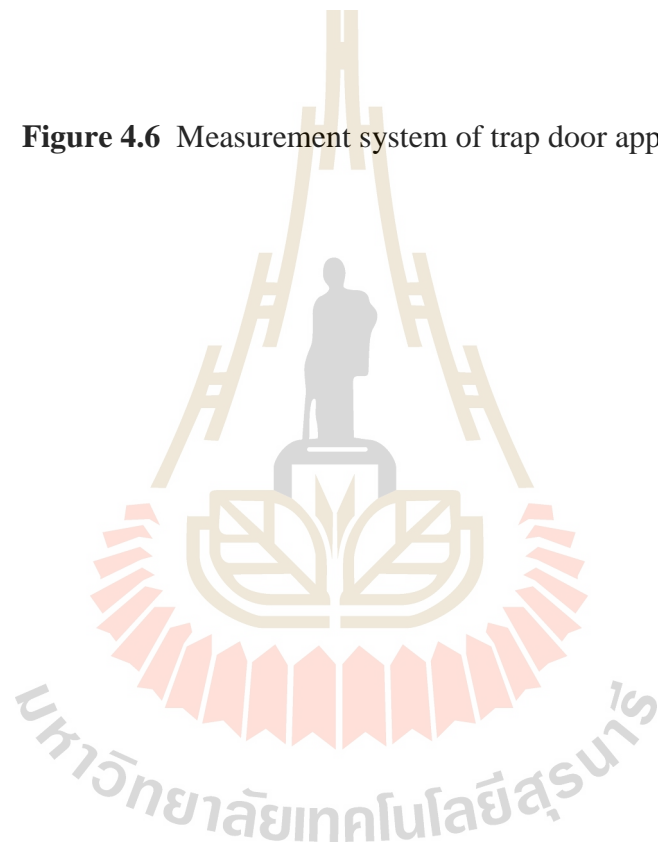


**Figure 4.6** Measurement system of trap door apparatus.



## CHAPTER V

### PHYSICAL MODELLING METHOD

#### 5.1 Introduction

The objective of the physical model testing in this study is to assess the effects of the opening geometry and depth on the surface subsidence. Based on the similarity theory, the mechanical and physical properties of the gel and the opening geometries are correlated with the overburden and geometry of actual mines in the Maha Sarakham formation.

#### 5.2 Similarity theory (scale law)

Due to the scale differences between the field (prototype) and laboratory experiment (model), the model material is selected to maintain meaningful physical proportional to the field conditions. The modeling materials need to be tested and its properties should satisfy similarity theory principles.

According to the similarity theory, sometimes called “scale law”, (Yavuz and Fowell, 2013), the elastic modulus and density of the synthetic gel, and model dimensions can be correlated with those of the prototypes representing the rock sequences above the mine openings in the Maha Sarakham formation. The similarity theory developed by Wood (2004) is used here to correlate the physical model with the prototype:

$$\frac{C_E}{C_p \cdot C_L} = 1 \quad (5.1)$$

where  $C_E$ ,  $C_\rho$  and  $C_L$  are the similarity constants for the elastic modulus, density and dimension (or ratios of the prototype-to-model properties). These constants can be presented as:

$$C_E = \frac{E_p}{E_m}, C_\rho = \frac{\rho_p}{\rho_m}, C_L = \frac{L_p}{L_m} \quad (5.2)$$

where  $E_p$ ,  $\rho_p$  and  $L_p$  are the elastic moduli, density and dimension of prototypes, and  $E_m$ ,  $\rho_m$ , and  $L_m$  are properties of the models.

The prototypes of the overburden in this study represent three locations: (1) Ban Waeng Ton, Wapi Pathum district, Maha Sarakham, (2) Ban Khao, Muang district, Udon Thani and (3) Ban Nong Plue, Borabue district, Maha Sarakham in the northeast of Thailand, as shown in Figure 5.1. Figure 5.2 shows typical stratigraphic sections of the boreholes. The prototype density and elastic modulus are averaged from the overburden above the mine openings in salt at 500 m depth. Their numerical values are shown in Table 5.1. The corresponding similarity constants can then be calculated, as shown in Table 5.2.

### 5.3 Physical model testing

Physical model simulations have been performed to determine the effects of underground opening configurations (widths and depths) and properties of the overburden on surface subsidence under sub-critical condition. The subsidence components considered here include angle of draw, maximum subsidence, maximum slope, horizontal strain, curvature and trough volume. A trap door apparatus is used

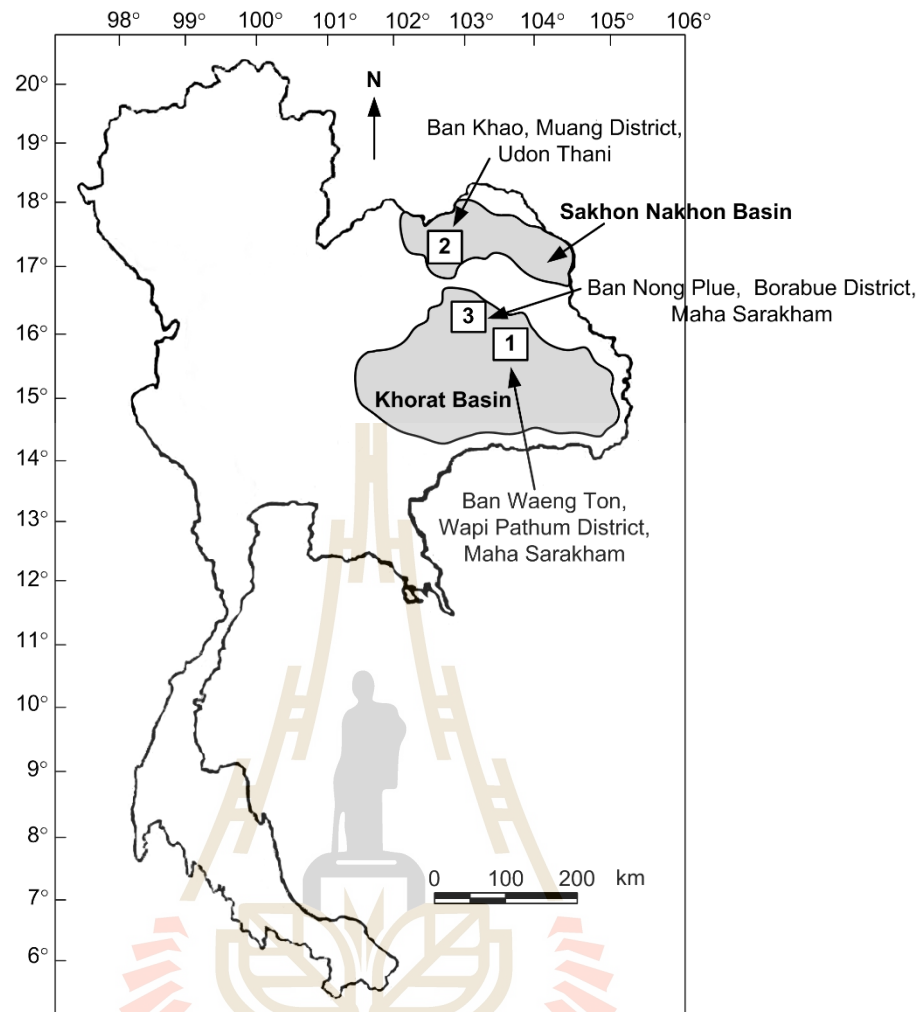


**Figure 5.1** Locations of overburden above salt openings in the Maha Sarakham formation.

to represent the scaled-down three-dimensional simulations of surface subsidence which allows fully controlled test conditions (Figure 5.3(a)). The opening width ( $W$ ) is simulated from 50, 100, 150, 200 to 250 mm. The overburden thickness ( $Z$ ) or opening depth is varied from 40, 60, 80 to 100 mm. The opening length ( $L$ ) and height ( $H$ ) are maintained constant at 200 and 10 mm, respectively. Each testing are simulated under different elastic moduli, including 1, 3 and 5 MPa. The opening



width is normalized by the depth ( $W/Z$ ), as shown in Table 5.3. The plastic blocks equivalent to the predefined  $W$ ,  $H$  and  $L$  are placed above the surface of the material container. For each series of simulations the synthetic gel are melted to obtain viscous fluid under the temperature of  $60\text{ }^{\circ}\text{C}$  (Figure 5.4). It is poured in the material container to a pre-defined thickness (Figure 5.5). The thickness of the synthetic gel layer represents the opening depth or the thickness of overburden. After the synthetic gel becomes semi-solid under temperature of  $32\text{ }^{\circ}\text{C}$ , the blocks are gradually and systematically moved down, and hence induces the vertical settlement of the synthetic gel above (Figure 5.3(b)). The measurement system includes a sliding rail with laser scanner. The laser scanner can be moved horizontally in two mutually perpendicular directions. The precision of the measurements is one micron. The laser scanner measures the surface profile of the gel before and after the subsidence is induced. The results are recorded and plotted in two-dimensional profiles. The subsidence profiles are used to calculate the subsidence components, including the angle of draw, maximum subsidence, trough volume, surface slope, curvature and horizontal strains.

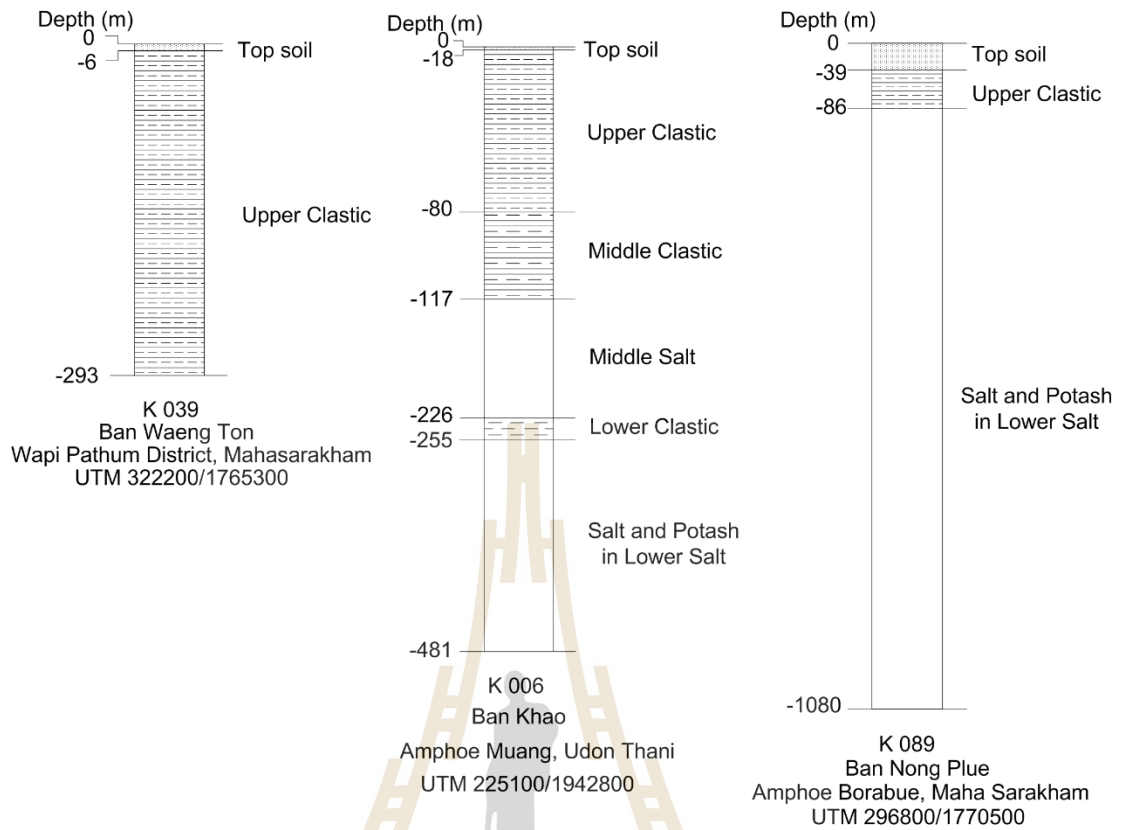


**Figure 5.2** Stratigraphic units of three boreholes drilled in the Maha Sarakham formation.

**Table 5.1** Density ( $\rho_p$ ) and elasticity ( $E_p$ ) of Maha Sarakham formation used as prototype properties (Crosby, 2007; Wetchasat, 2002).

Location	No.(i)	Rock unit	Thickness, $T_i$ (m)	Density, $\rho_i$ (kg/m <sup>3</sup> )	Elastic modulus, $E_i$ (GPa)	Average density, $\rho_p^*$ (kg/m <sup>3</sup> )	Average elastic modulus, $E_p^*$ (GPa)
1	1	Top soil	6	2,160	0.08	2,486	3.76
	2	Upper Clastic	494	2,490	3.80		
2	1	Top soil	18	2,160	0.08	2,178	10.96
	2	Upper Clastic	62	2,490	3.80		
	3	Middle Clastic	37	2,110	0.47		
	4	Middle Salt	109	2,140	2.42		
	5	Lower Clastic	29	2,160	3.24		
	6	Lower Salt	245	2,130	19.90		
3	1	Top soil	39	2,160	0.08	2,166	16.84
	2	Upper Clastic	47	2,490	3.80		
	3	Lower Salt	414	2,130	19.90		

Note: \*  $\rho_p = \frac{\sum_{i=1}^n \rho_i T_i}{\sum_{i=1}^n T_i}$ .

$$E_p = \frac{\sum_{i=1}^n E_i T_i}{\sum_{i=1}^n T_i} ; i = \text{no. of rock units}$$

**Table 5.2** Similarity theory constants.

Locations	Elastic modulus, E (MPa)		$C_E = E_p/E_m$	Density, $\rho$ (kg/m <sup>3</sup> )		$C_\rho = \rho_p/\rho_m$	Geometry (Opening width, depth, height, length), L (m)		$C_L = L_p/L_m$
	Model (E <sub>m</sub> )	Prototype (E <sub>p</sub> )		Model (E <sub>m</sub> )	Prototype (E <sub>p</sub> )		Model (E <sub>m</sub> )	Prototype (E <sub>p</sub> )	
1	1	3,755	3,755	980	2,486	2.53	0.05	74	1,484
2	3	10,964	3,655	990	2,178	2.20	0.05	83	1,661
3	5	16,841	3,368	990	2,146	2.19	0.05	77	1,538



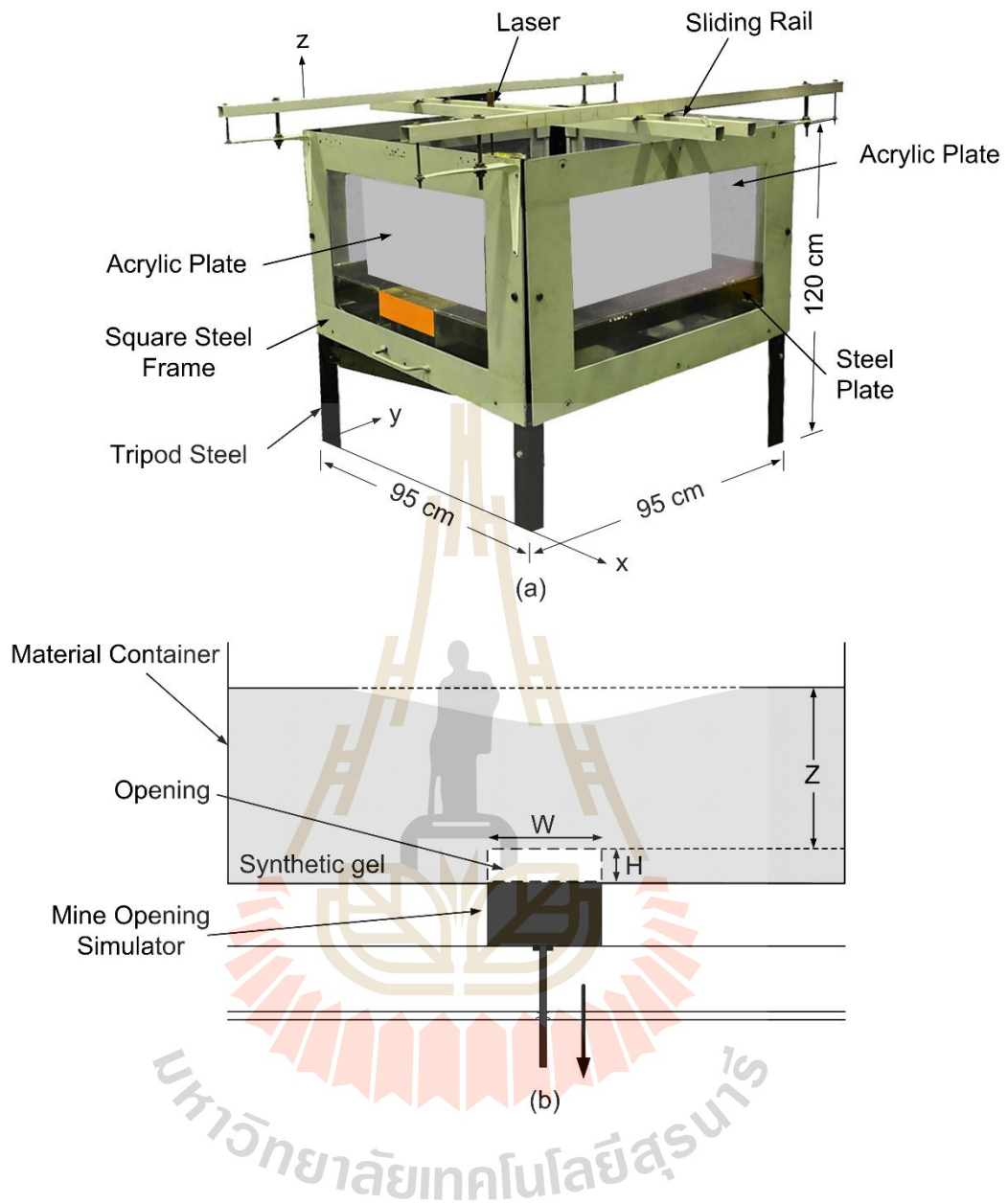


**Figure 5.3** Trap door apparatus used in physical model simulations.

**Table 5.3** Test variables

$E_m$ (MPa)	$E_p$ (GPa)	$W_m$ (mm)	$W_p$ (m)	$Z_m$ (mm)	$Z_p$ (m)	$W_m/Z_m = W_p/Z_p$
1	3.76	50	74	100	148	0.5
		100	148	100	148	1.0
		200	297	100	148	2.0
				60	89	3.3
				40	59	5.0
3	10.97	50	88	100	166	0.5
		100	166	100	166	1.0
		200	332	100	166	2.0
				60	100	3.3
				40	66	5.0
5	16.84	50	77	40	62	1.3
				60	92	0.8
				80	123	0.6
				100	154	0.5
		100	154	40	62	2.5
				60	92	1.7
				80	123	1.3
				100	154	1.0
		150	231	40	62	3.8
				60	92	2.5
				80	123	1.9
				100	154	1.5
		200	308	40	62	5.0
				60	92	3.3
				80	123	2.5
				100	154	2.0
		250	385	40	62	6.3
				60	92	4.2
				80	123	3.1
				100	154	2.5



**Figure 5.4** Synthetic gel melted into viscous fluid under temperature of 60 °c.



**Figure 5.5** Filling synthetic gel into material container.

## CHAPTER VI

### PHYSICAL MODEL RESULTS

#### 6.1 Introduction

The angle of draw, trough volume, surface slope, strains and curvature measured under a variety of opening depths and widths are presented in this chapter. They are used to develop a set of empirical equations as a function of opening width-to-depth ratios and elastic moduli of the gel using SPSS statistical software (Wendai, 2000).

#### 6.2 Test results

The results are presented in terms of the maximum subsidence-to-opening depth ratio ( $S_{\max}/Z$ ), angle of draw ( $\gamma$ ), maximum surface slope ( $G_{\max}$ ), maximum horizontal displacement-to-opening depth ratio ( $U_{\max}/Z$ ), maximum horizontal strain ( $\epsilon_{\max}$ ), curvature angle ( $\psi$ ) and volumetric ratio of trough-to-opening ( $V_s/V_o$ ). Figure 6.1 shows the test parameters and variables defined in the simulations. The angle of draw is a parameters used for defining the position of the limit of subsidence at the surface. The angle of draw is the angle between a vertical line from the edge of the underground opening and a line from the edge of the opening to the point of zero surface subsidence. The point of maximum surface subsidence is located in the center of the trough. Slope is calculated as the change in subsidence between two points divided by the distance between those points or the first derivative of the subsidence



profile. The maximum slope occurs at the inflection point in the subsidence trough. Curvature is the second derivative of subsidence, and is calculated as the change in slope between two adjacent sections of the profile divided by the average length of those sections. The horizontal displacement due to mine opening occurs in such a way that points on the surface move in towards the center of the subsidence trough. The horizontal displacement is greatest at the point of maximum slope and decreases to zero at the limit of subsidence and at the point of maximum subsidence. The horizontal strain is the difference in horizontal displacement between any two points divided by the distance between the two points.

An example of a scanned image and its cross section are shown in Figure 6.2. Tables 6.1 through 6.3 show the results for each set of the test variables. Figure 6.3(a) shows the angle of draw as a function of the opening width-to-depth ratio ( $W/Z$ ). The angle of draw increases with increasing elastic modulus and tends to be independent of the opening width-to-depth ratio. The observations agree reasonably with those obtained by Yao et al. (1991) who suggest that the stiffer overburden results in higher angle of draw.

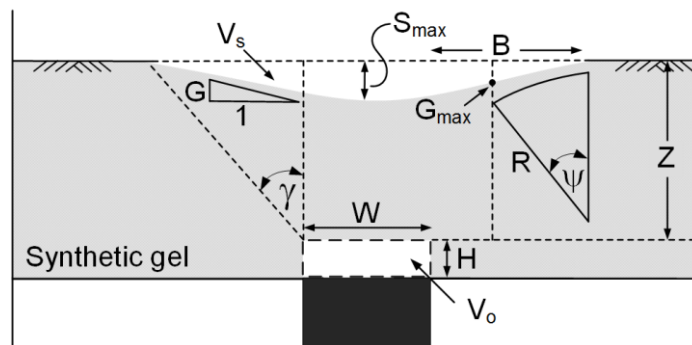


**Figure 6.1** Variables used in physical model simulations.

Figure 6.3(b) shows the  $S_{\max}\text{-}Z$  as a function of the  $W/Z$  with varying elastic moduli ( $E_m$ ). The  $S_{\max}\text{-}Z$  increases with increasing  $W/Z$  ratios. The maximum subsidence for the elastic overburden when  $E_m = 1$  MPa is approximately 10% of the overburden thickness (or opening depth). The subsidence decreases to 3% and 2% for  $E_m = 3$  and 5 MPa, respectively. The results suggest that the soft overburden with a relatively soft opening material allows the maximum subsidence than those obtained from rigid overburden. This generally agrees with the results obtained from Iwanec et al. (2016) who performed the surface subsidence prediction above the underground coal seams.

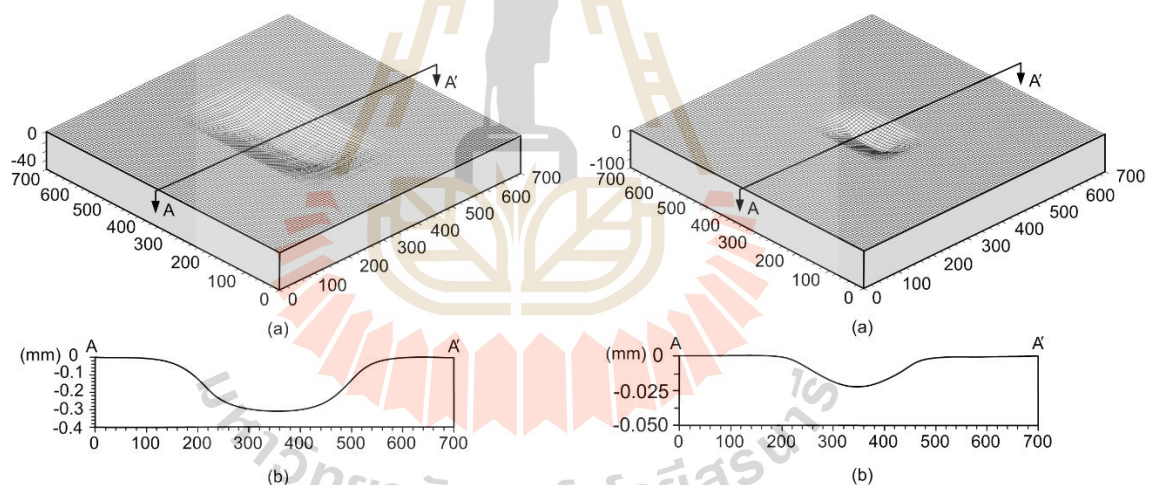


**Figure 6.2** Example of three-dimensional image of gel subsidence for  $Z = 40$  mm and  $W = 250$  mm (a) and cross-section image (b) (left) and  $Z = 100$  mm and  $W = 100$  mm (right). Vertical scale is greatly exaggerated.

**Table 6.1** Physical model results under different opening depths and widths for elastic modulus = 1 MPa.

Test variables			Results						
W (mm)	Z (mm)	W/Z	S <sub>max</sub> /Z	γ (°)	G <sub>max</sub> (×10 <sup>-3</sup> )	U <sub>max</sub> /Z (×10 <sup>-3</sup> )	ε <sub>max</sub> (×10 <sup>-3</sup> )	ψ (°)	V <sub>s</sub> /V <sub>o</sub>
50	100	0.5	0.0003	35.4	0.25	0.0003	0.012	0.014	0.005
100	100	1.0	0.0009	35.0	0.88	0.0007	0.042	0.050	0.011
200	100	2.0	0.0247	35.5	21.50	0.0645	1.032	1.232	0.048
200	60	3.3	0.0103	35.2	9.22	0.0184	0.443	0.528	0.043
200	40	5.0	0.0040	35.5	3.52	0.0042	0.169	0.202	0.034

**Table 6.2** Physical model results under different opening depths and widths for elastic modulus = 3 MPa.

Test variables			Results						
W (mm)	Z (mm)	W/Z	S <sub>max</sub> /Z	γ (°)	G <sub>max</sub> (×10 <sup>-3</sup> )	U <sub>max</sub> /Z (×10 <sup>-3</sup> )	ε <sub>max</sub> (×10 <sup>-3</sup> )	ψ (°)	V <sub>s</sub> /V <sub>o</sub>
50	100	0.5	0.0001	37.6	0.06	0.0001	0.003	0.003	0.001
100	100	1.0	0.0003	37.2	0.24	0.0003	0.012	0.014	0.003
200	100	2.0	0.0104	37.8	5.72	0.0172	0.275	0.328	0.026
200	60	3.3	0.0032	37.2	2.61	0.0052	0.125	0.150	0.017
200	40	5.0	0.0015	37.1	1.28	0.0015	0.061	0.073	0.013

**Table 6.3** Physical model results under different opening depths and widths for elastic modulus = 5 MPa.

Test variables			Results						
W (mm)	Z (mm)	W/Z	S <sub>max</sub> /Z	γ (°)	G <sub>max</sub> (×10 <sup>-3</sup> )	U <sub>max</sub> /Z (×10 <sup>-3</sup> )	ε <sub>max</sub> (×10 <sup>-3</sup> )	ψ (°)	V <sub>s</sub> /V <sub>o</sub>
50	40	1.3	0.0003	38.4	0.22	0.0006	0.010	0.012	0.001
	60	0.8	0.0001	38.7	0.10	0.0002	0.005	0.006	0.001
	80	0.6	0.0001	39.5	0.04	0.0001	0.002	0.002	0.001
	100	0.5	0.0001	39.3	0.03	0.0000	0.001	0.001	0.001
100	40	2.5	0.0008	38.2	0.66	0.0020	0.032	0.038	0.002
	60	1.7	0.0004	39.2	0.30	0.0006	0.014	0.017	0.002
	80	1.3	0.0002	39.9	0.18	0.0003	0.009	0.011	0.002
	100	1.0	0.0002	38.8	0.13	0.0002	0.006	0.008	0.002
150	40	3.8	0.0019	38.7	1.54	0.0046	0.074	0.088	0.005
	60	2.5	0.0010	38.9	0.82	0.0016	0.039	0.047	0.005
	80	1.9	0.0006	39.6	0.46	0.0007	0.022	0.026	0.004
	100	1.5	0.0004	39.9	0.31	0.0004	0.015	0.018	0.004
200	40	5.0	0.0044	39.4	3.64	0.0109	0.175	0.208	0.016
	60	3.3	0.0020	39.2	1.57	0.0031	0.076	0.090	0.009
	80	2.5	0.0013	39.7	0.95	0.0014	0.046	0.055	0.008
	100	2.0	0.0007	39.6	0.59	0.0007	0.029	0.034	0.007
250	40	6.3	0.0078	38.7	6.23	0.0187	0.299	0.357	0.019
	60	4.2	0.0035	39.5	2.73	0.0055	0.131	0.156	0.014
	80	3.1	0.0020	39.9	1.53	0.0023	0.074	0.088	0.012
	100	2.5	0.0014	40.1	1.05	0.0013	0.050	0.060	0.011

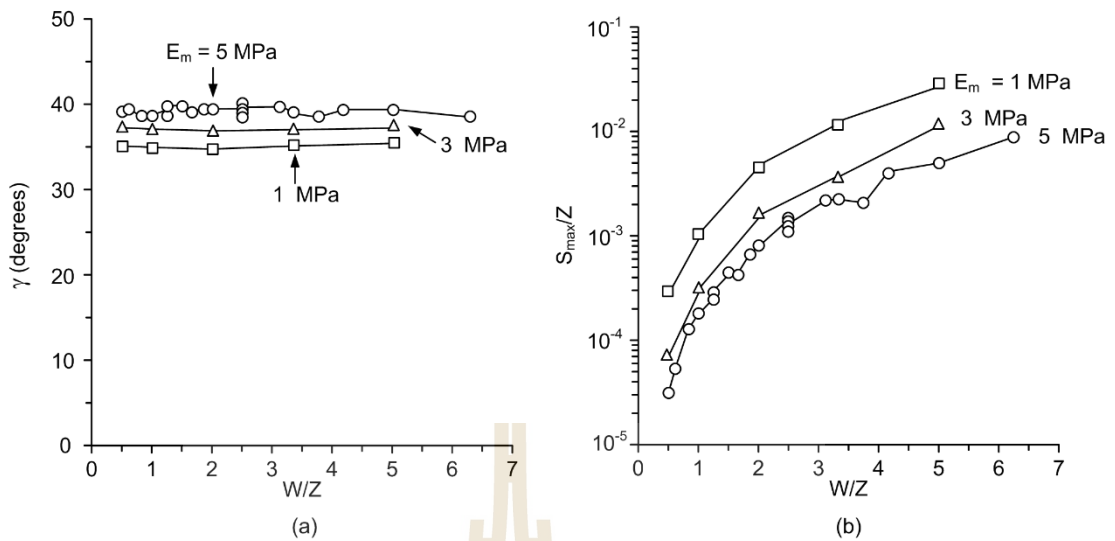


**Figure 6.3** Angle of draw (a) and maximum subsidence-to-opening depth ratio (b) as a function of the opening width-to-depth ratios ( $W/Z$ ) for various elastic modulus of model.

The maximum slope and curvature angle plotted as a function of  $W/Z$  ratio in Figure 6.4. The  $G_{max}$  and  $\psi$  increase with increasing the  $W/Z$  ratio and decrease with increasing  $E_m$ . They are however not that much sensitive to  $E_m$ . The  $G_{max}$  rapidly increases when the  $W/Z$  ratios less than 2.0.

The maximum horizontal displacement-to-opening depth ratios and maximum horizontal strain are plotted as a function of the opening width-to-depth ratios for various elastic modulus of the overburden in Figure 6.5. The results indicate that the  $U_{max}-Z$  and  $\epsilon_{max}$  increase with increasing the  $W/Z$  ratios and decrease with increasing the  $E_m$ .

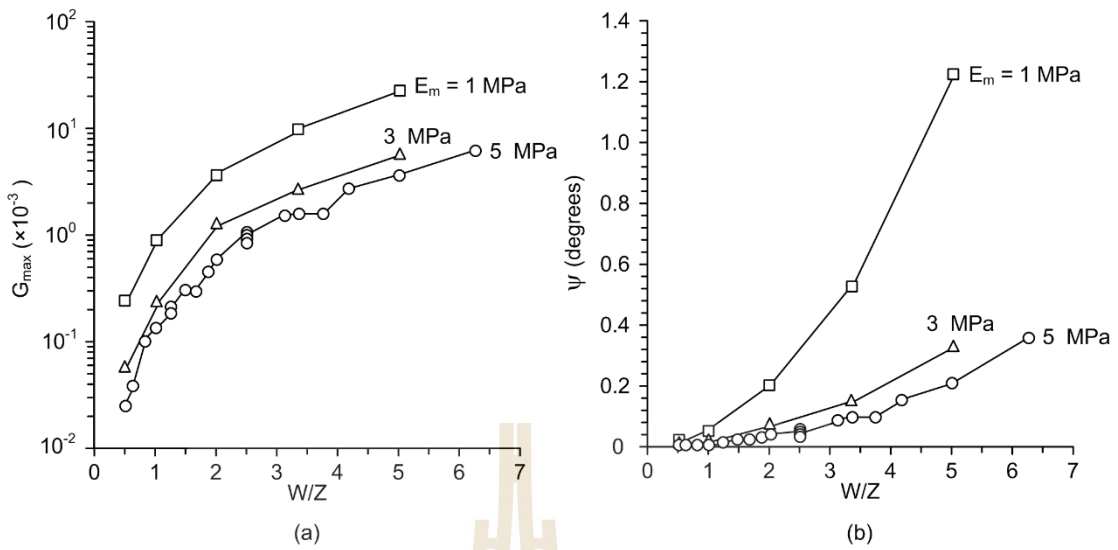


**Figure 6.4** Maximum surface slope (a) curvature angle (b) as a function of the opening width-to-depth ratios for various elastic modulus of model.

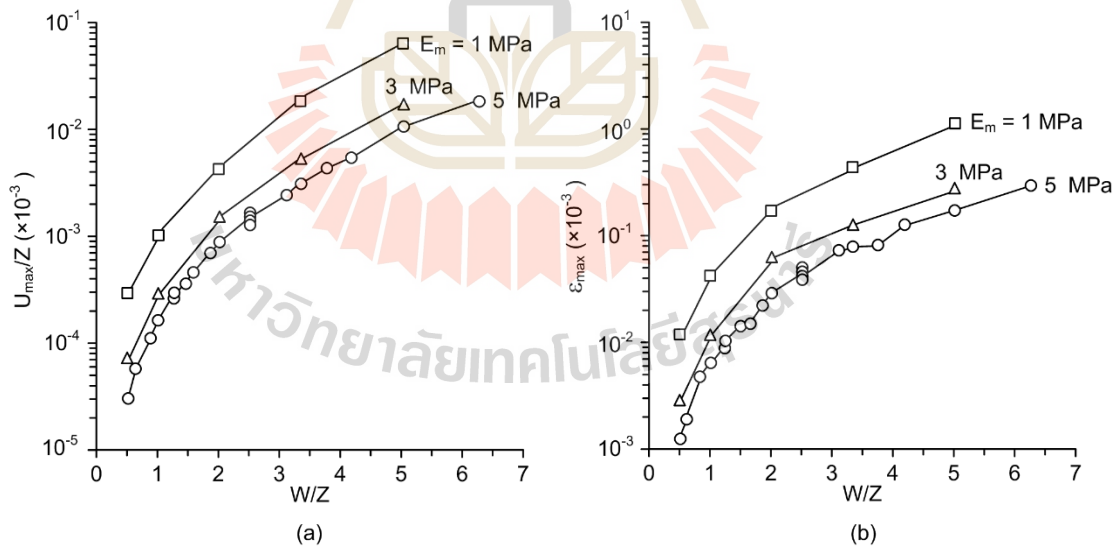


**Figure 6.5** Maximum horizontal displacement-to-opening depth ratio (a) and maximum horizontal strain (b) as a function of the opening width-to-depth ratio for various elastic modulus of model.

Figures 6.6 through 6.11 show the subsidence profiles measured from all cases of the physical model testing. The different opening geometries give different characteristics of subsidence, as discussed above. The volume of subsidence trough per unit length ( $V_s$ ) can be calculated from:

$$V_s = 2 \int_{-W/2}^B S(x) dx \quad (6.1)$$

The widths of the trough are calculated for each case using the angles of draw given in Tables 6.1 through 6.3. An attempt is made here to determine the effects of the opening width and depth on the volume of the subsidence trough. Figure 6.12 plots the subsidence trough volume normalized by the opening volume ( $V_s/V_o$ ) as a function of opening width-to-depth ratio ( $W/Z$ ). The physical model results clearly show that the trough volume is less than the opening volume. This hole true for all opening width used here ( $W/Z = 0.5-6.3$ ). The largest trough volume is obtained for  $W/Z = 5.0$  and  $E_m = 1$  MPa, which is about 5% of the opening volume. The subsidence trough tends to increase as the opening width increases, particularly for soft overburden (lower  $E_m$  value).

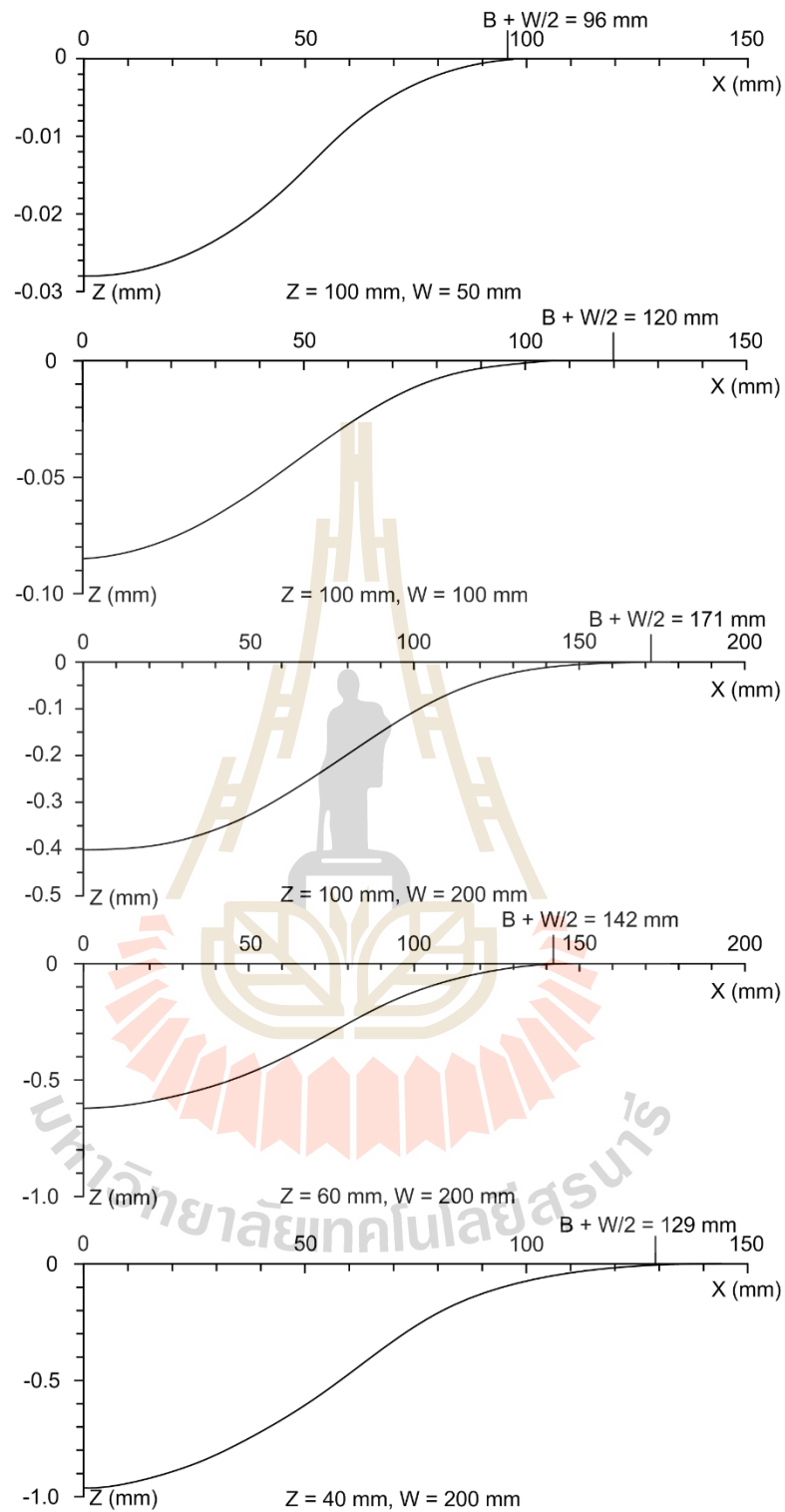


**Figure 6.6** Subsidence profiles measured from physical model test under  $E_m = 1 \text{ MPa}$  for various opening width and depth.



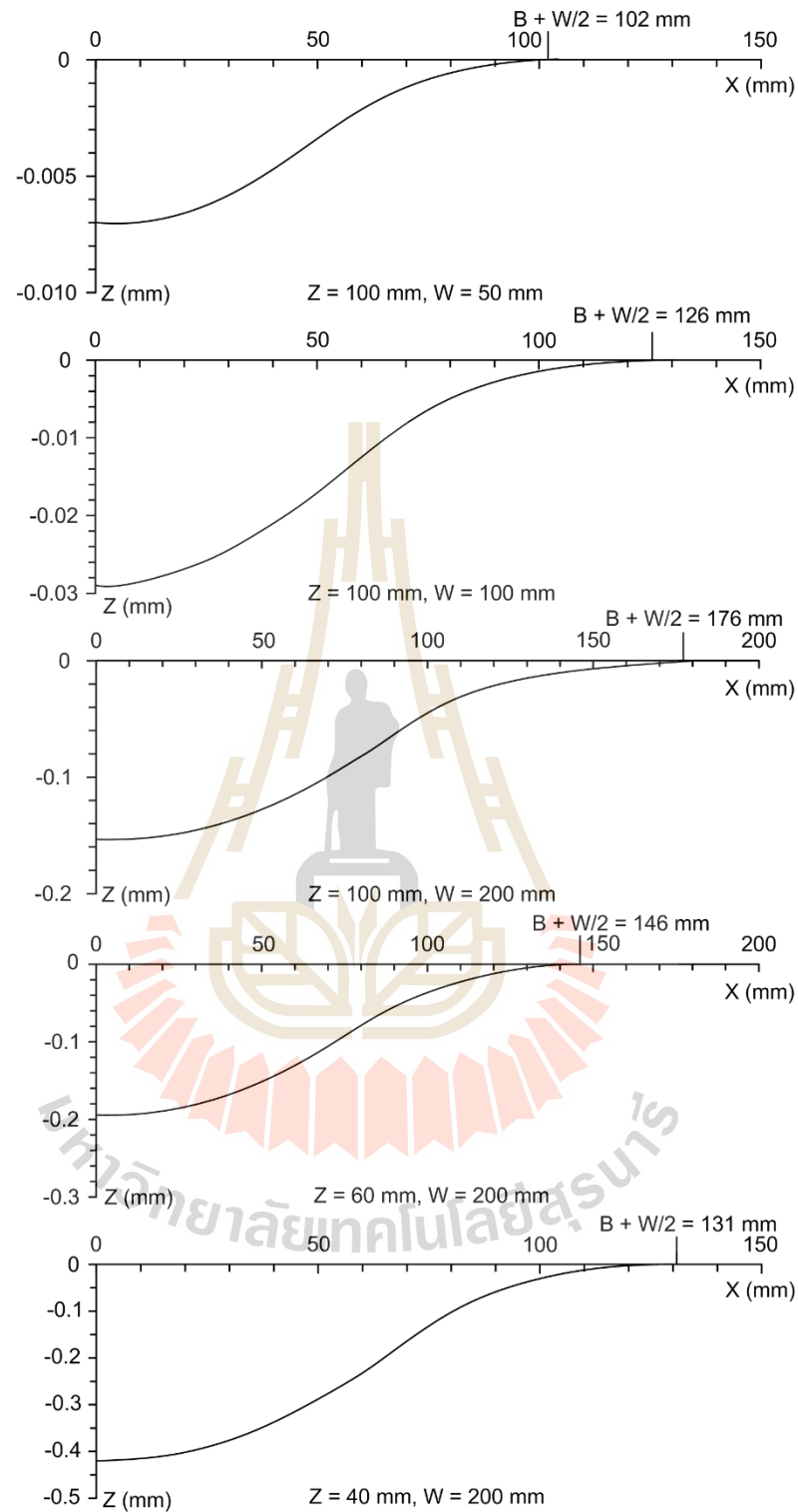


**Figure 6.7** Subsidence profiles measured from physical model test under  $E_m = 3$  MPa for various opening width and depth.

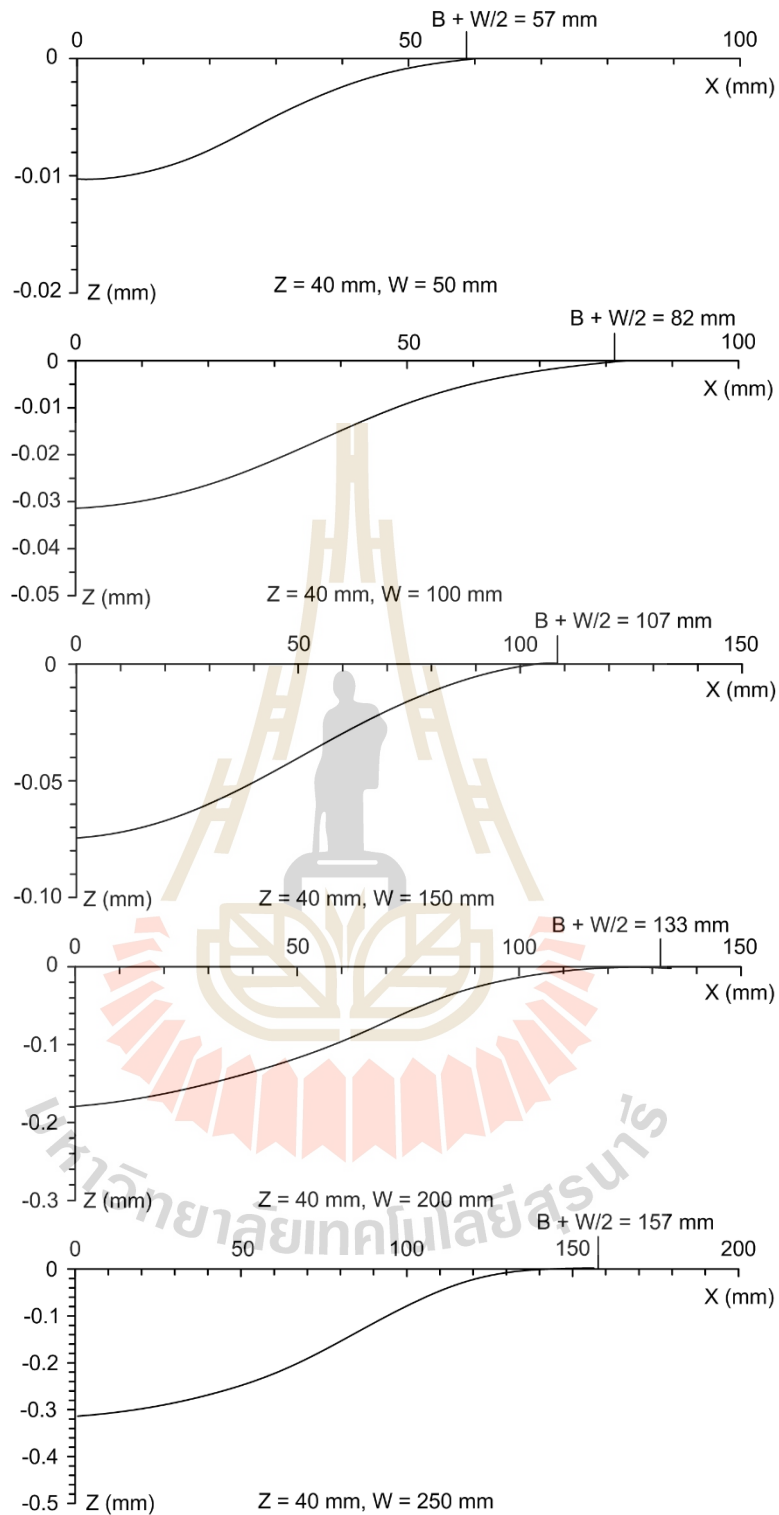


**Figure 6.8** Subsidence profiles measured from physical model test under  $E_m = 5 \text{ MPa}$  and opening depth = 40 mm.

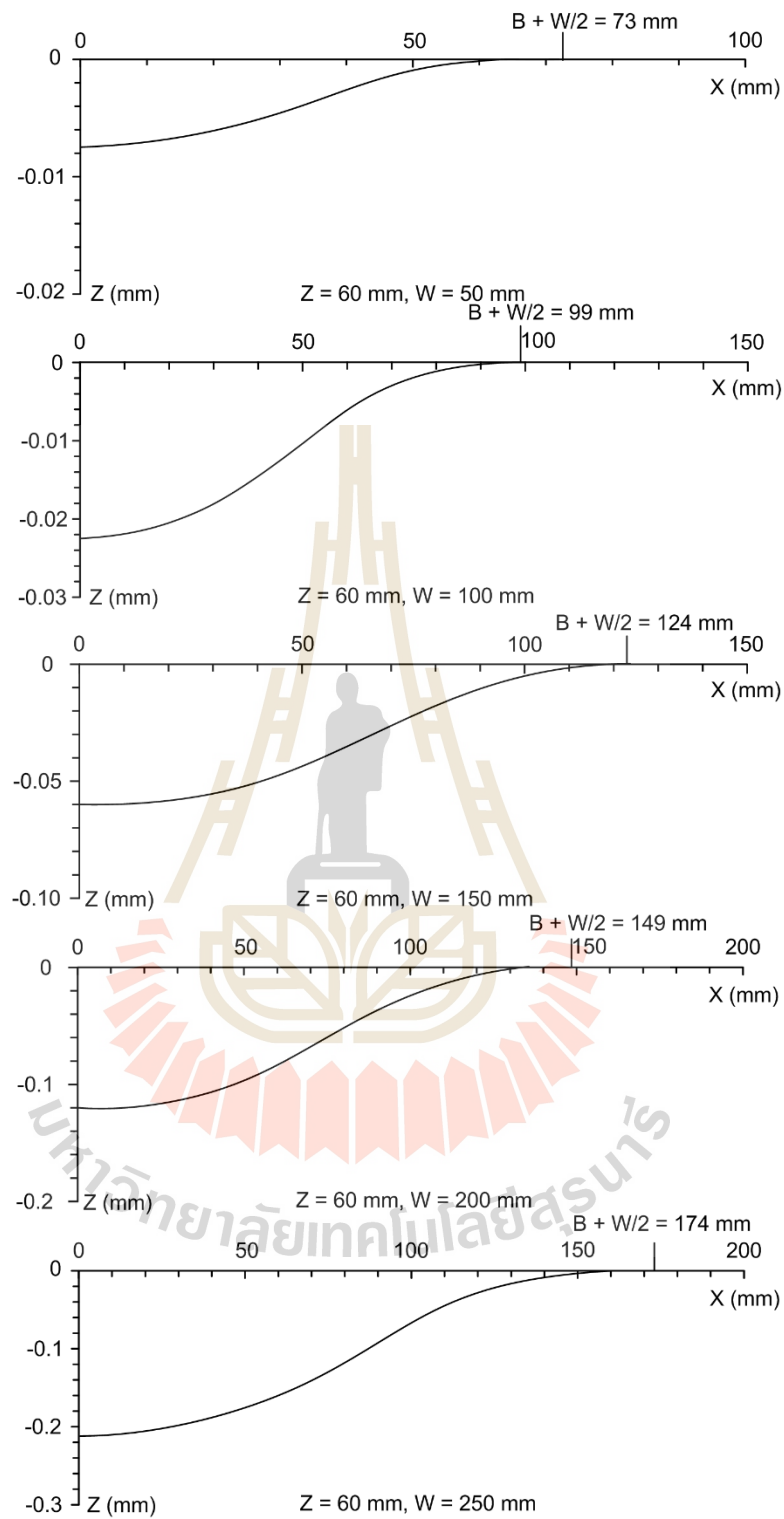


**Figure 6.9** Subsidence profiles measured from physical model test under  $E_m = 5$  MPa and opening depth = 60 mm.

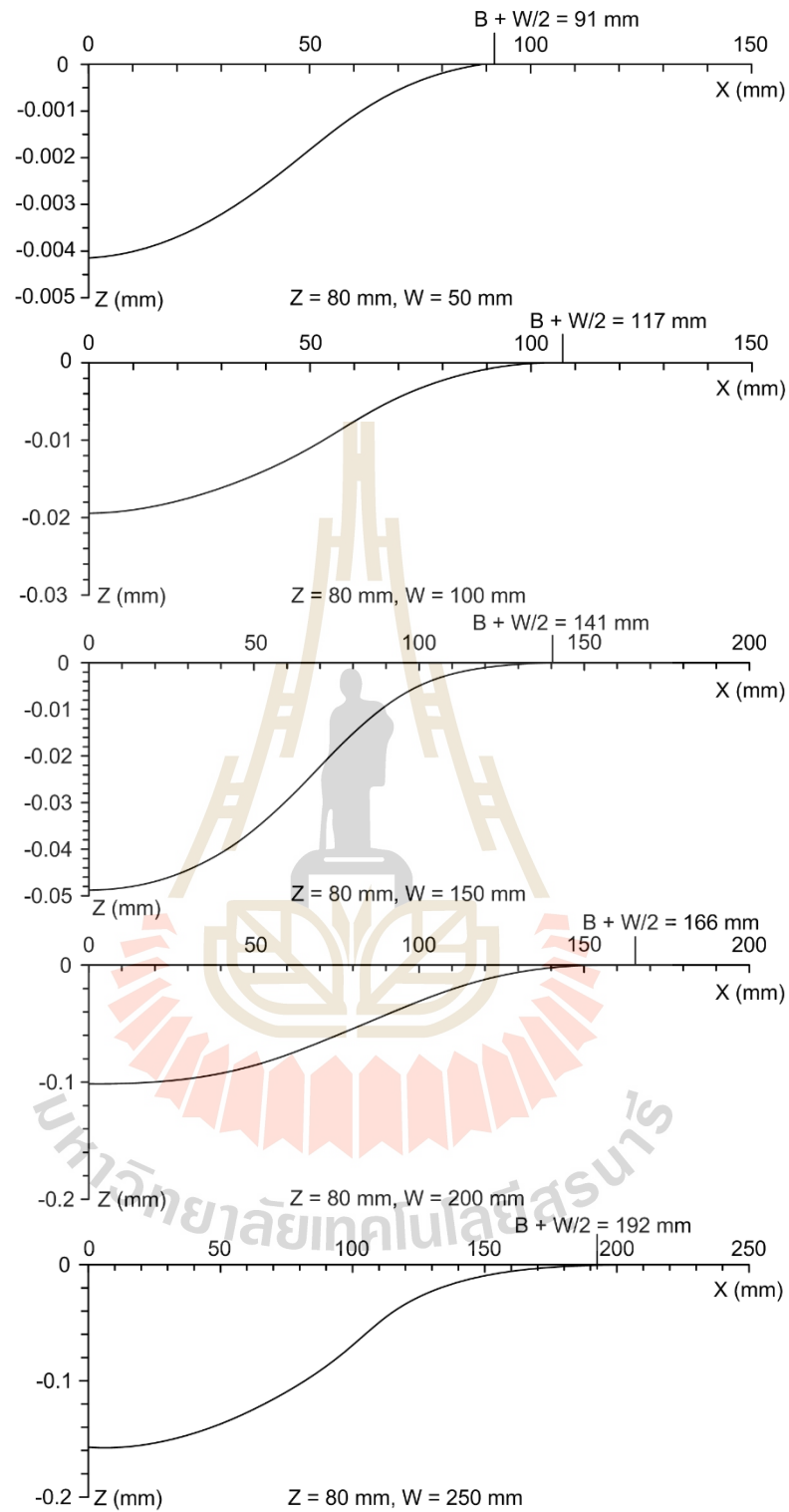


**Figure 6.10** Subsidence profiles measured from physical model test under  $E_m = 5$  MPa and opening depth = 80 mm.

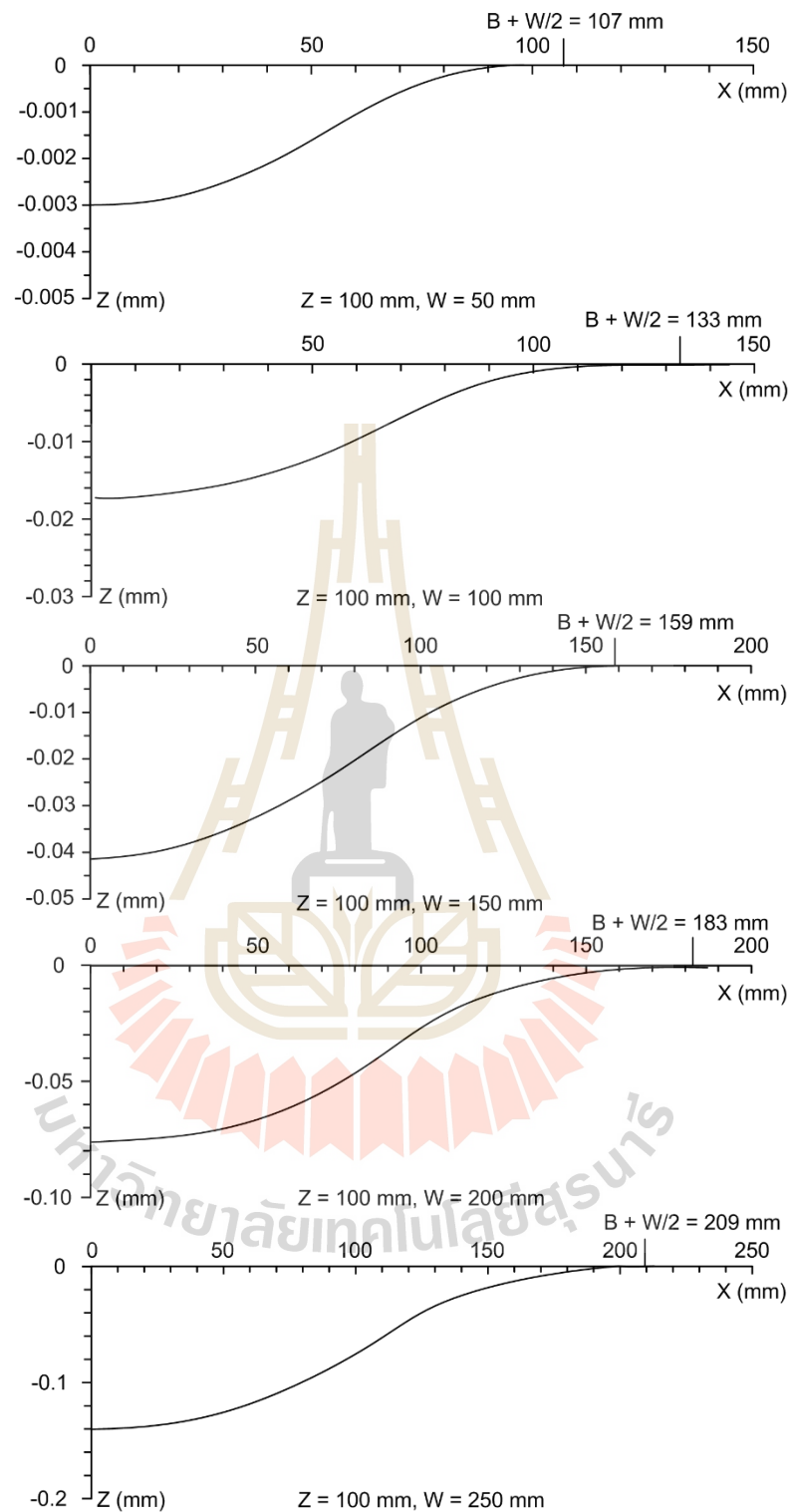


**Figure 6.11** Subsidence profiles measured from physical model test under  $E_m = 5$  MPa and opening depth = 100 mm.

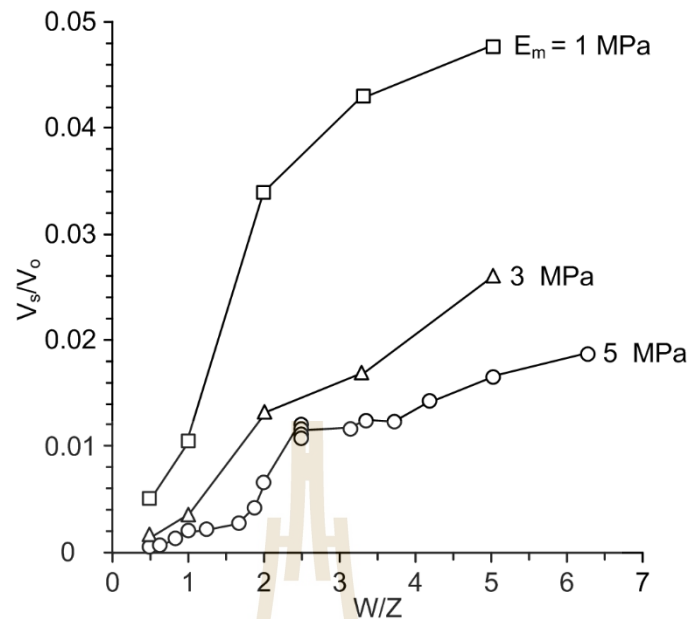


**Figure 6.12** Volumetric ratio of trough volume-to-excavation volume ( $V_s/V_o$ ) as a function of opening width-to-depth ratio for various elastic moduli.

### 6.3 Prediction

The physical model results are used to develop a set of empirical equations. The equations are presented as a function of opening width-to-depth ratio and elastic moduli. Statistical analyses are performed using the SPSS code (Wendai, 2000) to fit the test results with the empirical equations. The predictive capability of these equations is determined and compared using the coefficient of correlation ( $R^2$ ) as an indicator.

The variation of the angle of draw can be observed from the  $\gamma$  -  $W/Z$  diagrams, as shown in Figure 6.13(a). The linear relation between the  $\gamma$  and  $W/Z$  and elastic properties of overburden ( $E_m$ ), and can be best represented by:

$$\gamma = (1.22 E_m + 32.87) + 0.16 W/Z \quad (\text{Degrees}) \quad (6.2)$$

The empirical constants above are obtained from the regression analysis of the physical results. Figure 6.13(a) compares the predictions with the test results. Good correlation is obtained ( $R^2 > 0.9$ ).

An empirical equation is proposed to predict the maximum subsidence-to-opening depth ratio under various opening width-to-depth ratios and elastic moduli:

$$S_{\max}/Z = 1 \times 10^{-3} / E_m \cdot (W/Z)^{2.07} \quad (6.3)$$

Figure 6.13(b) shows that the  $S_{\max}/Z$  increases with  $W/Z$  and  $E_m$ . The equation provides good correlation with the test data, with  $R^2$  greater than 0.9.

The maximum surface subsidence for the all tests are plotted as a function of the opening width-to-depth ratios and elastic moduli.

$$G_{\max} = 0.64 / E_m \cdot (W/Z)^{2.16} \quad (\times 10^{-3}) \quad (6.4)$$

where  $G_{\max}$  is maximum surface slope ( $\times 10^{-3}$ ). Good correlation is obtained ( $R^2 = 0.982$ ). Figure 6.14(a) compares the test results with the back predictions from the proposed equation.

From the physical test results the curvature angle can be presented as a function of the opening width-to-depth ratios and elastic moduli. The equation can be written as:

$$\psi = 0.044 / E_m \cdot (W/Z)^{2.03} \quad (\text{Degrees}) \quad (6.5)$$

Figure 6.14(b) compares the test results with curve fit in terms of  $\psi$  as a function of  $W/Z$  and  $E_m$ .

The maximum horizontal displacement increases with increasing  $W/Z$  and decreases with increasing elastic modulus (Figure 6.15(a)). The maximum horizontal displacement normalized by the opening depth ( $U_{\max}/Z$ ), can be expressed as a function of  $W/Z$  and  $E_m$  as:

$$U_{\max}/Z = 8 \times 10^{-4} / E_m \cdot (W/Z)^{2.55} \quad (6.6)$$

Similar to the prediction above, the relationships for the  $\epsilon_{\max}$  and the  $W/Z$  can be developed (Figure 6.15(b)):

$$\epsilon_{\max} = 0.038 / E_m \cdot (W/Z)^{2.03} \quad (\text{milli-strains}) \quad (6.7)$$

Figure 6.16 plots the subsidence trough volume normalized by the opening volume ( $V_s/V_o$ ) as a function of opening width-to-depth ratio ( $W/Z$ ) for various elastic moduli ( $E_m$ ). For each  $E_m$  value,  $V_s/V_o$  increases with  $W/Z$ , which can be represented by:

$$V_s/V_o = 0.03 E_m^{-0.75} \cdot \ln (W/Z + 0.65) \quad (6.8)$$



The empirical equations developed above can be correlated with the actual field condition based on the scale law, which are presented in Table 6.4.

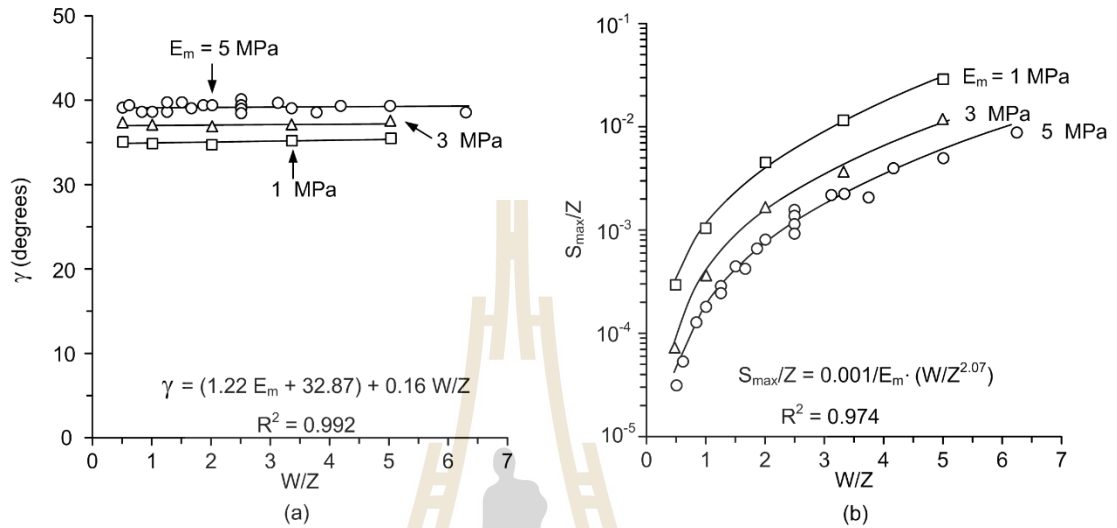


Figure 6.13 Predicted angle of draw (a) and maximum subsidence-to-opening depth ratio (b) as a function of the opening width-to-depth ratios ( $W/Z$ ) for various elastic modulus of model ( $E_m$ ).

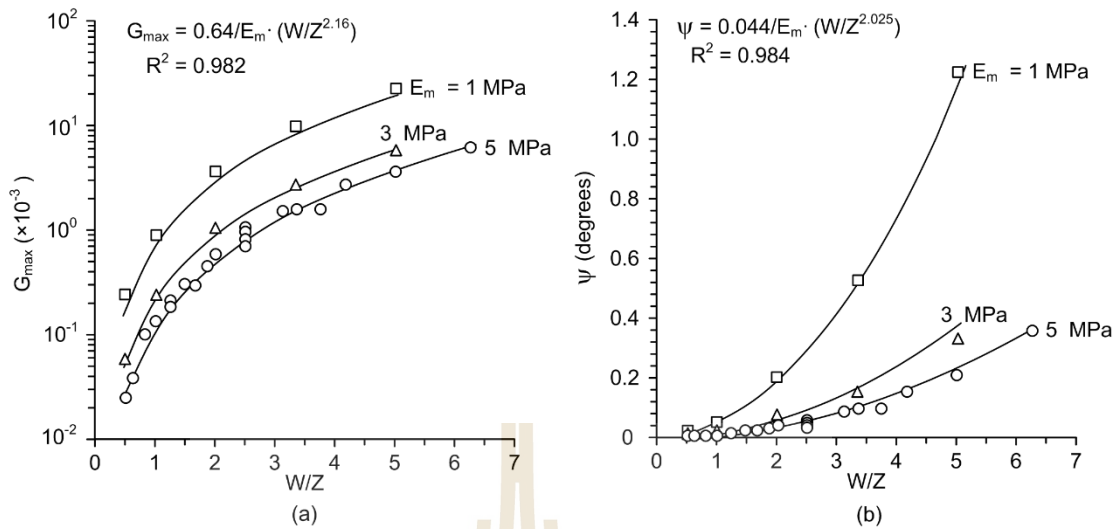


Figure 6.14 Predicted maximum surface slope (a) curvature angle (b) as a function of the opening width-to-depth ratios ( $W/Z$ ) for various elastic modulus of model ( $E_m$ ).

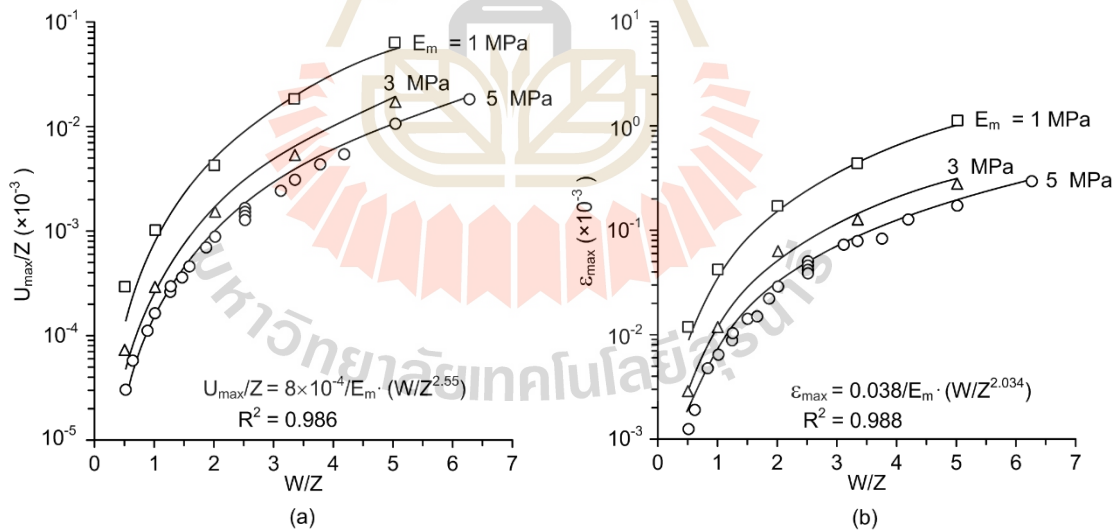


Figure 6.15 Predicted maximum horizontal displacement-to-opening depth ratio (a) and maximum horizontal strain (b) as a function of the opening width-to-depth ratios ( $W/Z$ ) for various elastic modulus of model ( $E_m$ ).

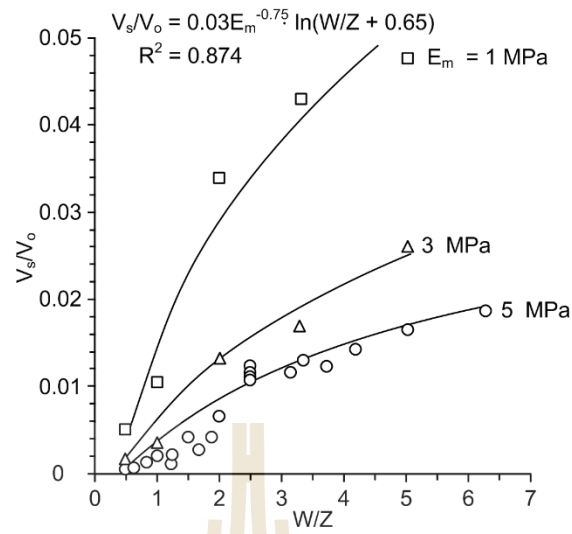


Figure 6.16 Predicted volumetric ratio of trough volume to excavation volume ( $V_s/V_o$ ) as a function of the opening width-to-depth ratios ( $W/Z$ ) for various elastic modulus of model ( $E_m$ ).

**Table 6.4** Physical model results correlated with actual fields conditions.

Test Variables			Model		Prototype	
$E_m$ (MPa)	$E_p$ (GPa)	$W_m/Z_m = W_p/Z_p$	$S_{max,m}$ (mm)	$B_m$ (mm)	$S_{max,p}$ (cm)	$B_p$ (m)
1	3.76	0.5	0.028	77.0	0.42	114.3
		1.0	0.095	76.0	1.41	112.8
		2.0	0.401	75.6	5.95	112.2
		3.3	0.618	45.5	9.17	67.5
		5.0	0.989	31.0	14.68	46.0
3	10.96	0.5	0.007	71.0	0.12	117.9
		1.0	0.029	70.0	0.48	116.3
		2.0	0.152	71.3	2.52	118.5
		3.3	0.193	42.4	3.21	70.4
		5.0	0.416	28.5	6.91	47.3
5	16.84	0.5	0.003	81.9	0.05	126.0
		0.6	0.004	66.0	0.06	101.5
		0.8	0.007	48.0	0.11	73.8
		1.0	0.017	80.5	0.27	123.8
		1.3	0.011	31.7	0.16	48.8
		1.3	0.019	67.0	0.29	103.0
		1.5	0.041	83.5	0.63	128.4
		1.7	0.023	49.0	0.35	75.4
		1.9	0.049	66.2	0.75	101.8
		2.0	0.074	82.8	1.14	127.3
		2.5	0.032	31.5	0.49	48.4
		2.5	0.060	48.5	0.92	74.6
		2.5	0.100	66.5	1.55	102.3
		2.5	0.139	84.2	2.14	129.5
		3.1	0.157	67.0	2.42	103.0
		3.3	0.121	49.0	1.86	75.4
		3.8	0.076	32.0	1.17	49.2
4.2	0.210	49.4	3.23	76.0		
5.0	0.177	32.8	2.72	50.4		
6.3	0.314	32.0	4.82	49.2		

# **CHAPTER VII**

## **COMPARISON OF COMPUTER AND PHYSICAL MODEL**

### **7.1 Introduction**

This chapter describes the finite difference analyses using finite difference code (FLAC 4.0) (Itasca, 1992) to simulate the surface subsidence profiles correlated with the overburden elastic properties and underground opening configurations. The results obtained from the FLAC are compared with the physical model simulations.

### **7.2 Computer simulations**

Thirty models are simulated under various overburden elastic properties and opening geometries. The boundary conditions used in the simulation are identical to those of the physical models. The opening height is maintained constant at 10 mm for all cases. The opening depths vary from 40, 60, 80 to 100 mm. The opening widths are 50, 100, 150, 200 and 250 mm. Each modelling is simulated under different elastic moduli, including 1, 3 and 5 MPa. The material properties used in the FLAC models are shown in Tables 7.1. To cover the entire range of the opening dimensions, over 4,000 meshes have been constructed to obtain accurate simulation results. The analyses are made in plane strain condition. The distance between the center of the opening to the other edge is 0.5 m. The left and right sides of the model did not allow

**Table 7.1.** FLAC simulation parameters.

Model no.	$E_m$ (MPa)	$\rho_m$ (kg/m <sup>3</sup> )	$\nu_m$	$W_m$ (mm)	$Z_m$ (mm)
1	1	980	0.35	50	100
				100	100
				200	100
					60
					40
2	3	990	0.36	50	100
				100	100
				200	100
					60
					40
3	5	990	0.36	50	40
					60
					80
					100
				100	40
					60
					80
					100
				150	40
					60
					80
					100
				200	40
					60
					80
					100
				250	40
60					
80					
100					

horizontal displacement (fixed X-axis), and the bottom boundary did not allow vertical displacement (fixed Y-axis). The upper boundary can move freely in both x and y directions. The smallest mesh simulated around the opening is  $1 \times 2 \text{ mm}^2$  because the stress and strain gradients are high at this zone, and the mesh are gradually larger when the boundary is far from the opening. Figure 7.1 gives an example of mesh models representing the mine openings of 40, 60, 80 and 100 mm depths. The overburden above the opening is assumed to be elastic. Some elements are deleted at defined locations to simulate the opening. The overburden is then deformed. Each numerical model has a processing of approximately 10,000 cycles until the model is under equilibrium condition. The subsidence components considered here include the angle of draw, maximum subsidence, maximum slope, horizontal strain, curvature and trough volume.

### 7.3 Comparison of numerical and physical results

Close agreements of the results are obtained between the FLAC simulation and physical model, in terms of the  $S_{\max}/Z$ ,  $\gamma$ ,  $G_{\max}$ ,  $U_{\max}/Z$ ,  $\epsilon_{\max}$ ,  $\psi$  and  $V_s/V_o$  values. Tables 7.2 through 7.4 show the numerical results for each set of the test variables. Figure 7.2(a) presents the predicted angle of draw as a function of W/Z ratios under various  $E_m$ . The angle of draw tends to be independent of the W/Z ratios. The results show that there is a good agreement between the both methods. For all cases, the  $\gamma$  predicted from numerical simulations is higher than those obtained from physical results by about 1%. This is true for all opening geometries and elastic moduli of overburden.

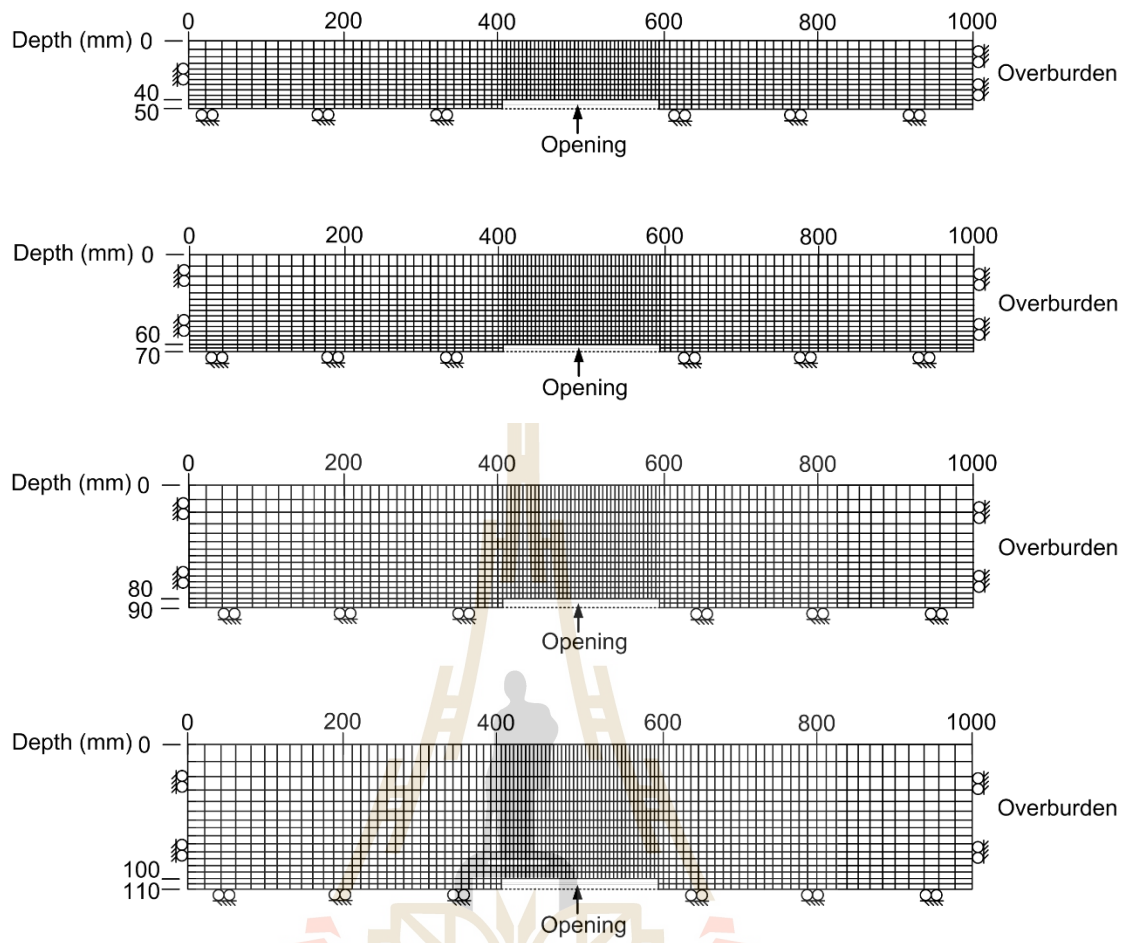


**Figure 7.1** Example of finite difference mesh developed for FLAC simulations.



**Table 7.2** Numerical simulation results under different opening depths and widths for elastic modulus = 1 MPa.

Parameters			Results						
W (mm)	Z (mm)	W/Z	S <sub>max</sub> /Z	γ (°)	G <sub>max</sub> (×10 <sup>-3</sup> )	U <sub>max</sub> /Z (×10 <sup>-3</sup> )	ε <sub>max</sub> (×10 <sup>-3</sup> )	ψ (°)	V <sub>s</sub> /V <sub>o</sub>
50	100	0.5	0.0003	35.4	0.25	0.0003	0.012	0.014	0.005
100	100	1.0	0.0009	35.0	0.88	0.0007	0.042	0.050	0.011
200	100	2.0	0.0040	35.5	3.52	0.0042	0.169	0.202	0.034
200	60	3.3	0.0103	35.2	9.22	0.0184	0.443	0.528	0.043
200	40	5.0	0.0247	35.5	21.50	0.0645	1.032	1.232	0.048

**Table 7.3** Numerical simulation results under different opening depths and widths for elastic modulus = 3 MPa.

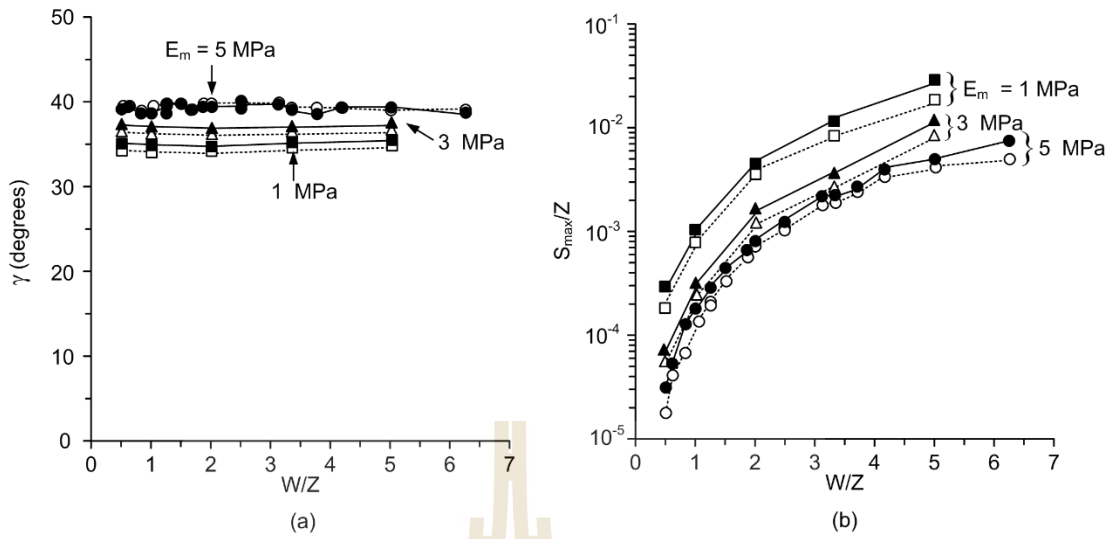
Parameters			Results						
W (mm)	Z (mm)	W/Z	S <sub>max</sub> /Z	γ (°)	G <sub>max</sub> (×10 <sup>-3</sup> )	U <sub>max</sub> /Z (×10 <sup>-3</sup> )	ε <sub>max</sub> (×10 <sup>-3</sup> )	ψ (°)	V <sub>s</sub> /V <sub>o</sub>
50	100	0.5	0.0001	37.6	0.06	0.0001	0.003	0.003	0.001
100	100	1.0	0.0003	37.2	0.24	0.0003	0.012	0.014	0.003
200	100	2.0	0.0015	37.1	1.28	0.0015	0.061	0.073	0.013
200	60	3.3	0.0032	37.2	2.61	0.0052	0.125	0.150	0.017
200	40	5.0	0.0104	37.8	5.72	0.0172	0.275	0.328	0.026

**Table 7.4** Numerical simulation results under different opening depths and widths for elastic modulus = 5 MPa.

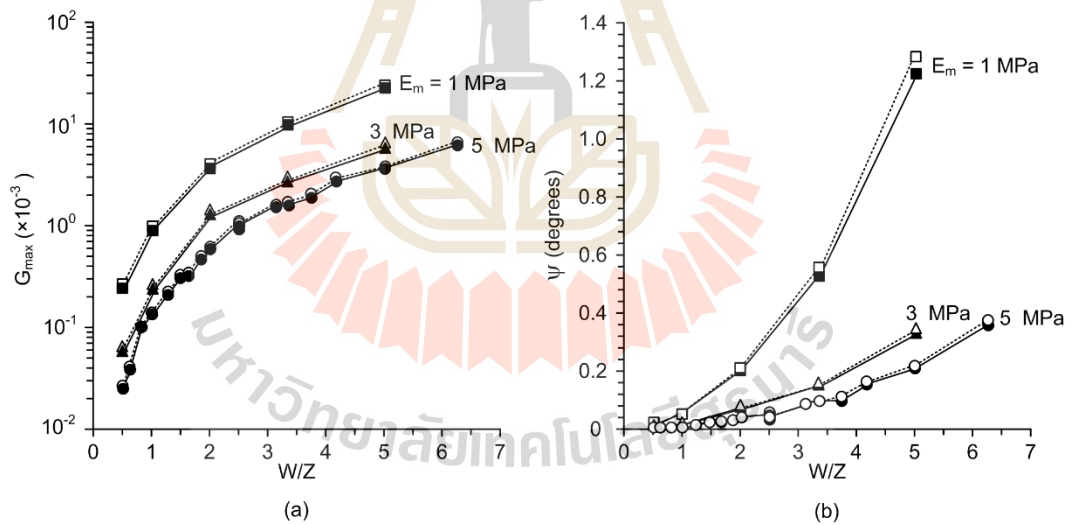
Parameters			Results						
W (mm)	Z (mm)	W/Z	S <sub>max</sub> /Z	γ (°)	G <sub>max</sub> (×10 <sup>-3</sup> )	U <sub>max</sub> /Z (×10 <sup>-3</sup> )	ε <sub>max</sub> (×10 <sup>-3</sup> )	ψ (°)	V <sub>s</sub> /V <sub>o</sub>
50	40	1.3	0.0002	38.2	0.23	0.0007	0.011	0.013	0.002
	60	0.8	0.0001	38.5	0.10	0.0002	0.005	0.006	0.001
	80	0.6	0.0000	39.3	0.04	0.0001	0.002	0.002	0.001
	100	0.5	0.0000	39.5	0.03	0.0000	0.001	0.001	0.001
100	40	2.5	0.0007	38.2	0.69	0.0021	0.033	0.039	0.011
	60	1.7	0.0003	38.8	0.31	0.0006	0.015	0.018	0.006
	80	1.3	0.0002	39.7	0.19	0.0003	0.009	0.011	0.002
	100	1.0	0.0002	39.7	0.14	0.0002	0.007	0.008	0.002
150	40	3.8	0.0018	38.4	1.60	0.0048	0.077	0.091	0.014
	60	2.5	0.0009	38.9	0.83	0.0017	0.040	0.048	0.010
	80	1.9	0.0005	39.7	0.50	0.0007	0.024	0.028	0.007
	100	1.5	0.0004	39.7	0.32	0.0004	0.016	0.019	0.004
200	40	5.0	0.0043	38.2	3.78	0.0113	0.181	0.217	0.015
	60	3.3	0.0019	38.9	1.64	0.0033	0.079	0.094	0.011
	80	2.5	0.0012	39.7	1.01	0.0015	0.049	0.058	0.010
	100	2.0	0.0007	39.7	0.61	0.0007	0.029	0.035	0.008
250	40	6.3	0.0077	39.2	6.60	0.0198	0.317	0.378	0.016
	60	4.2	0.0034	39.1	2.88	0.0058	0.138	0.165	0.014
	80	3.1	0.0019	39.9	1.60	0.0024	0.077	0.092	0.012
	100	2.5	0.0013	40.0	1.10	0.0013	0.053	0.063	0.010

Figure 7.2(b) shows a comparison between the  $S_{\max}/Z$  obtained from the physical and numerical models. The magnitudes of the predicted maximum subsidence are approximately 10% of the opening depth for  $E_m = 1$  MPa, and decrease to 5% and 3% for  $E_m = 3$  and 5 MPa, respectively. The numerical simulations slightly underestimate the  $S_{\max}/Z$  value obtained from the laboratory testings. The discrepancies of the two results are less than 5%.

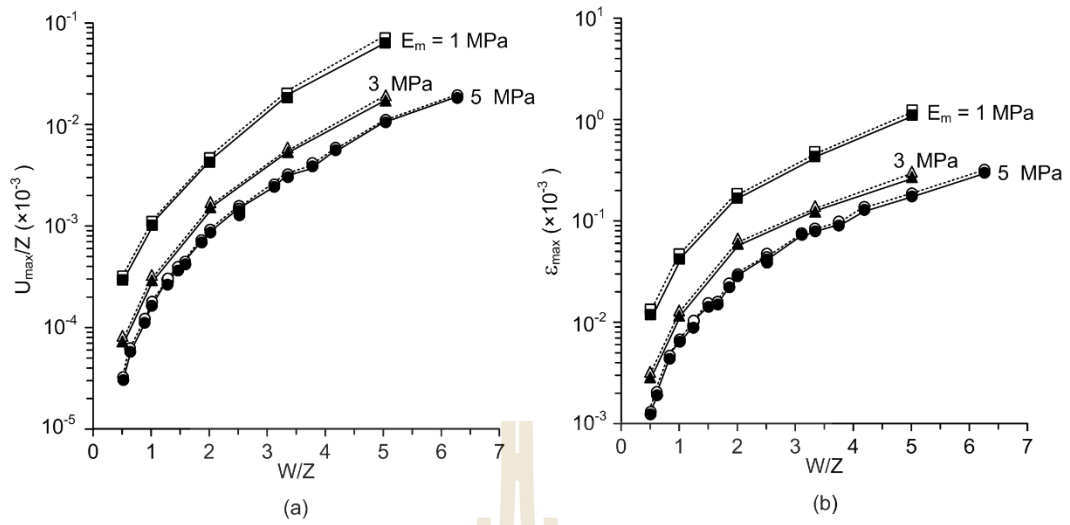
The FLAC simulations show the increasing trends of the maximum surface slope and curvature angle with opening width-to-depth ratio which are similar to those observed from the test models. For all cases the predicted  $G_{\max}$  values slightly overestimate the test results (Figure 7.3). Figure 7.4 shows the horizontal displacement-to-opening depth ratio and maximum horizontal strain increases with increasing  $W/Z$  ratios for each elastic moduli. For all cases the predicted  $U_{\max}/Z$  and  $\epsilon_{\max}$  values agree well with the test results. The volumetric ratio of trough-to-opening ( $V_s/V_o$ ) are plotted as a function of  $W/Z$  ratios in Figure 7.5. The  $V_s/V_o$  ratios increase with increasing  $W/Z$  and decrease with increasing  $E_m$ . The discrepancies between the numerical and physical results are about 10%, 7% and 5% for  $E_m = 1, 3$  and 5 MPa, respectively. The discrepancies are probably due to the sizes and number of the elements used in the mesh model. The smaller elements and larger number of the elements would provide even closer of the numerical solution to the physical model test results.



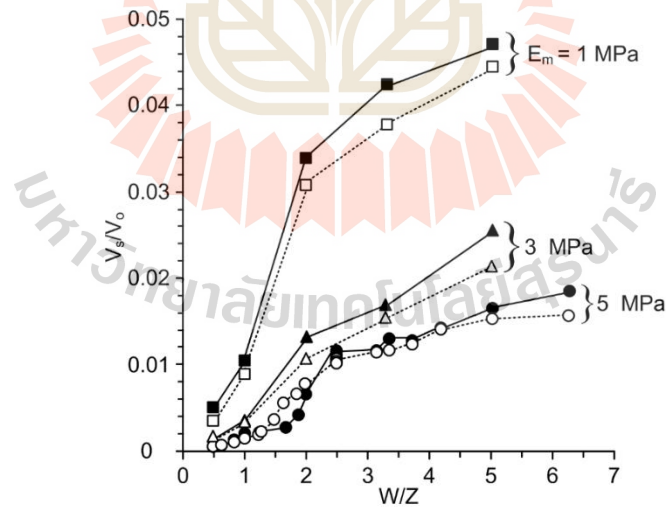
**Figure 7.2** Comparison of angle of draw (a) and maximum subsidence-to-opening depth ratio (b) obtained from FLAC and physical model test.



**Figure 7.3** Comparison of maximum slope (a) and curvature angle (b) obtained from FLAC and physical model test.

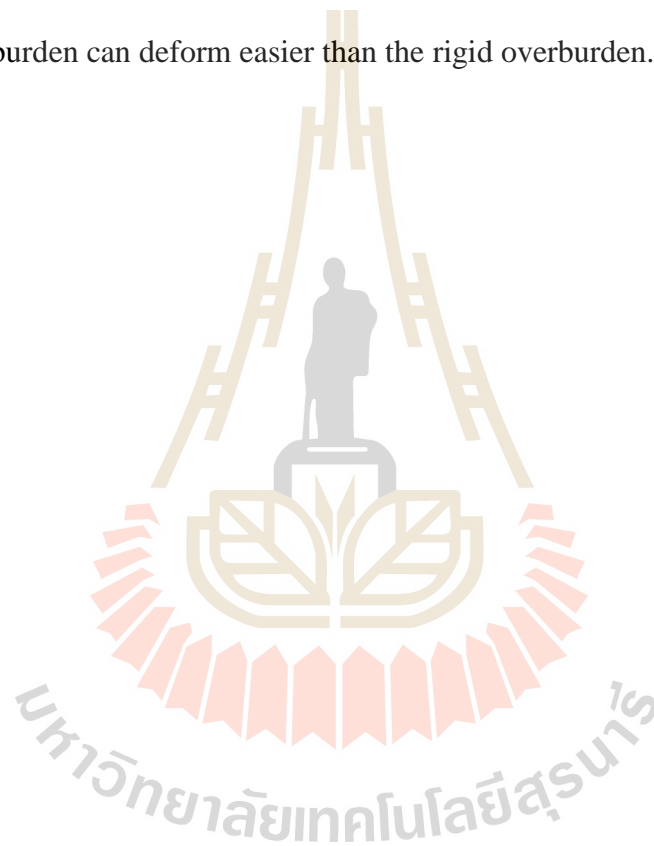


**Figure 7.4** Comparison of maximum horizontal displacement-to-opening depth ratio (a) and maximum horizontal strain (b) obtained from FLAC and physical model test.



**Figure 7.5** Comparison of volumetric ratio of trough-to-opening ( $V_s/V_o$ ) obtained from FLAC and physical model test.

Figures 7.6 through 7.11 show the subsidence profiles measured from the physical model testing and predicted from the FLAC simulation under various the elastic moduli, and opening depths and widths. The subsidence profiles obtained from the numerical model that is shallower and narrower than obtained from those physical model. Under the same opening depth and width, a soft overburden (lower  $E_m$  value) shows deeper subsidence and narrower extent than higher  $E_m$  value because the soft overburden can deform easier than the rigid overburden.



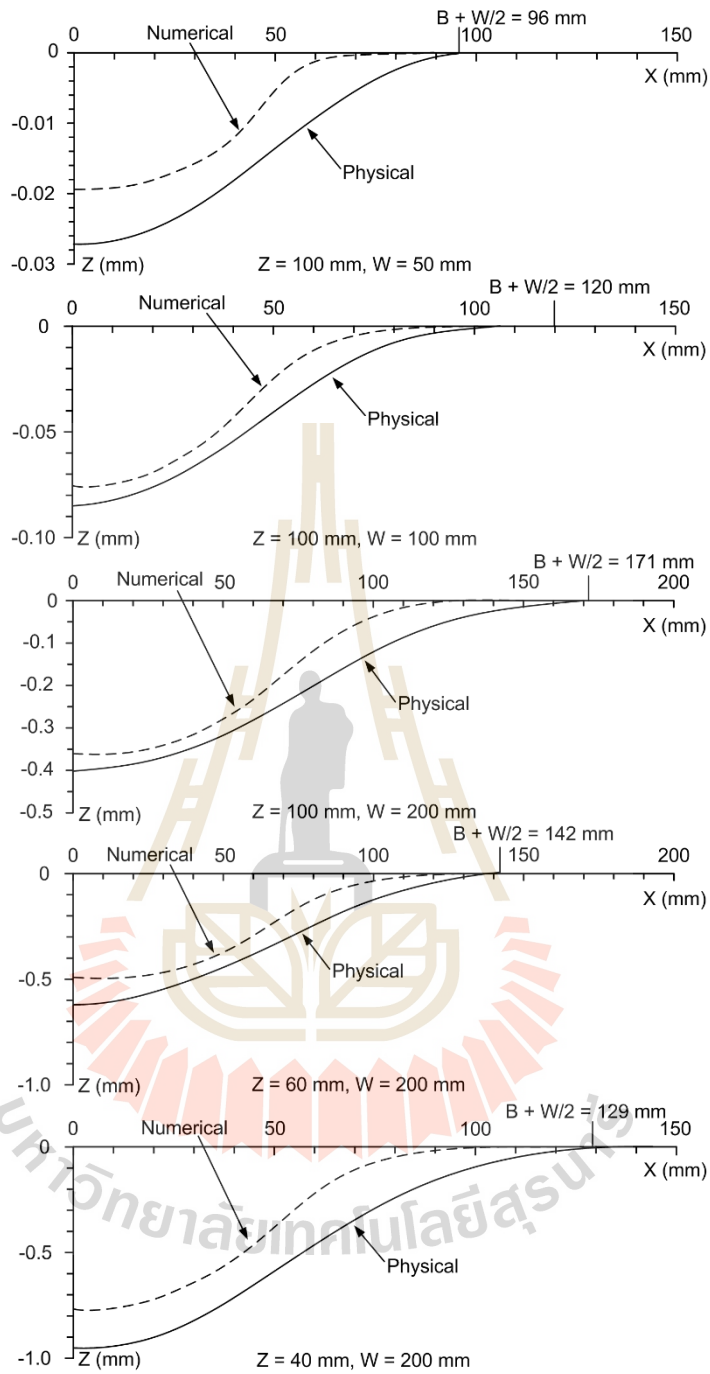


**Figure 7.6** Comparisons of subsidence profiles measured from physical and predicted by numerical model under  $E_m = 1$  MPa for various opening width and depth.

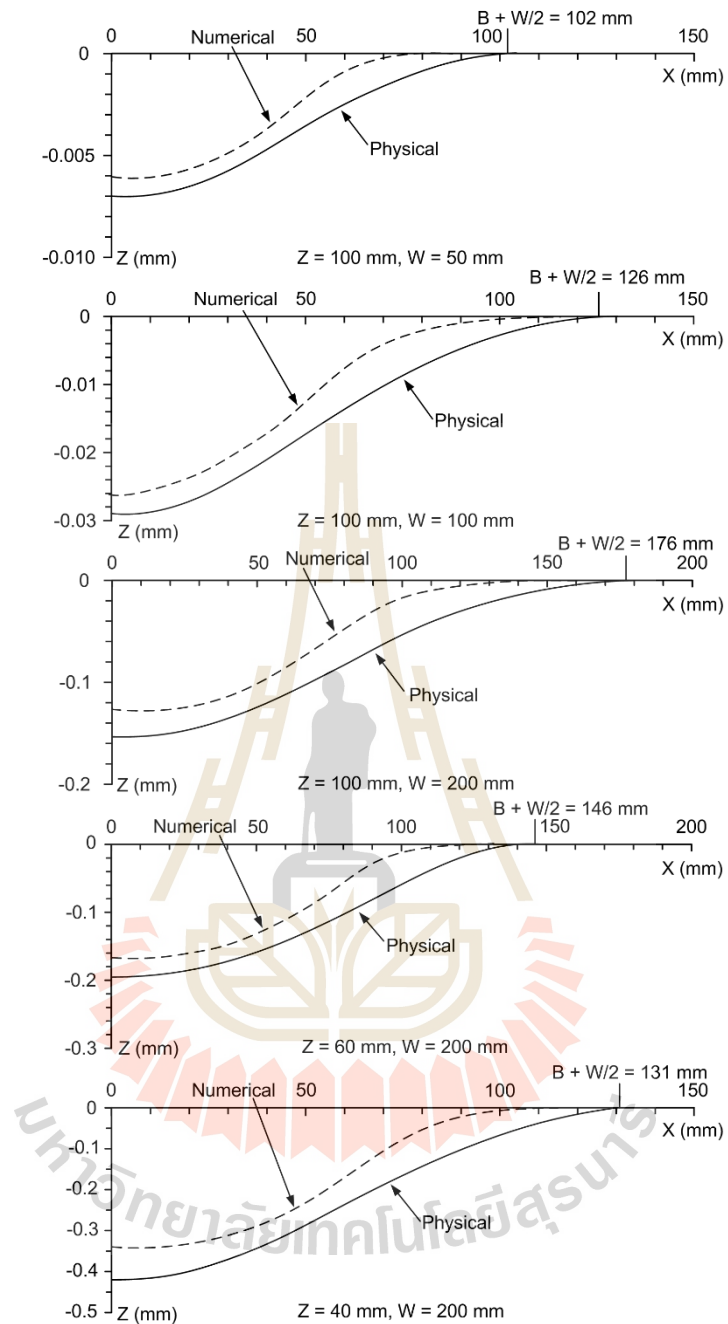


**Figure 7.7** Comparisons of subsidence profiles measured from physical and predicted by numerical model under  $E_m = 3$  MPa for various opening width and depth.



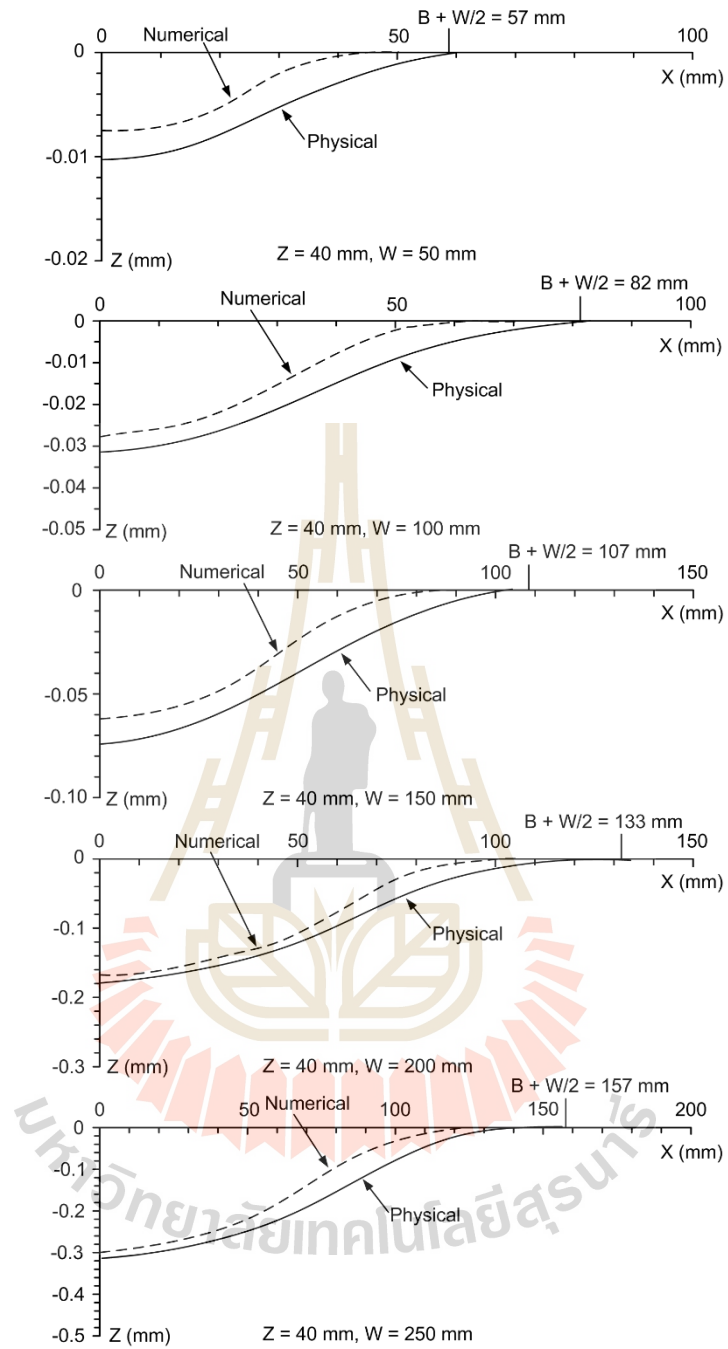


**Figure 7.8** Comparisons of subsidence profiles measured from physical and predicted by numerical model under  $E_m = 5 \text{ MPa}$  and opening depth = 40 mm.

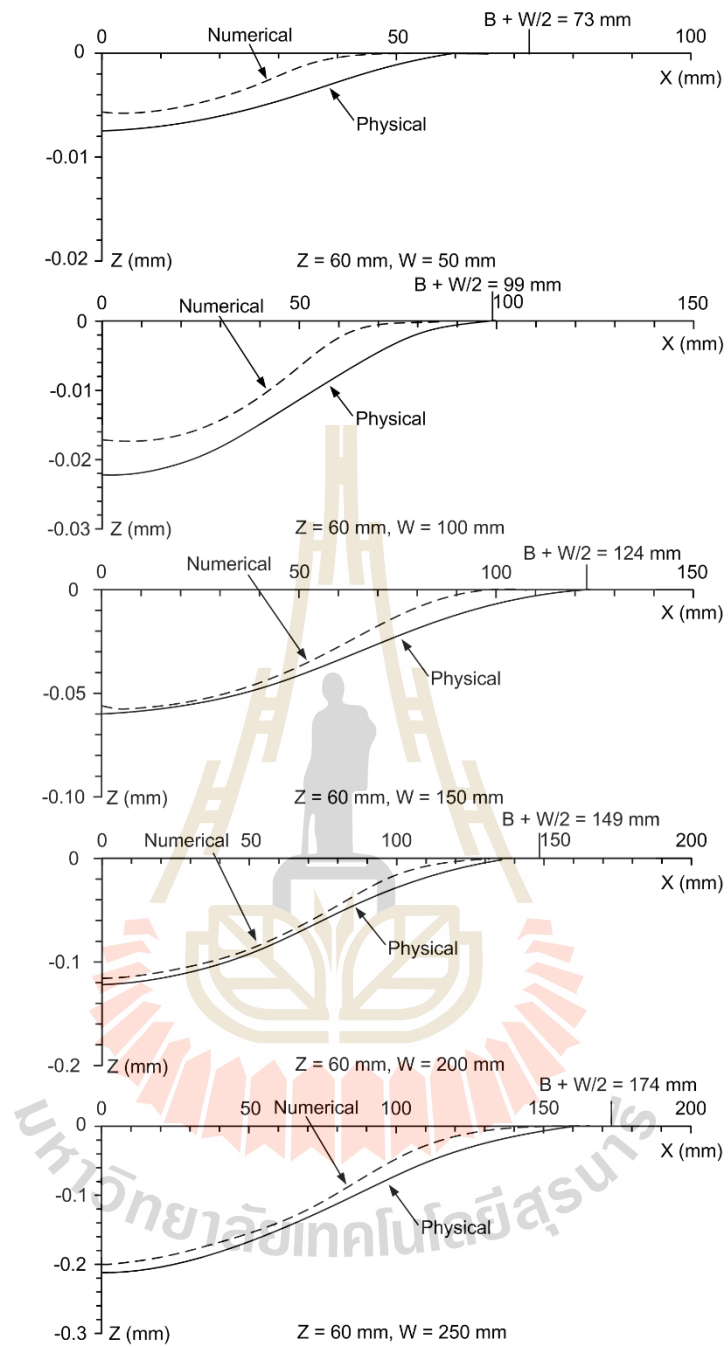


**Figure 7.9** Comparisons of subsidence profiles measured from physical and predicted by numerical model under  $E_m = 5$  MPa and opening depth = 60 mm.

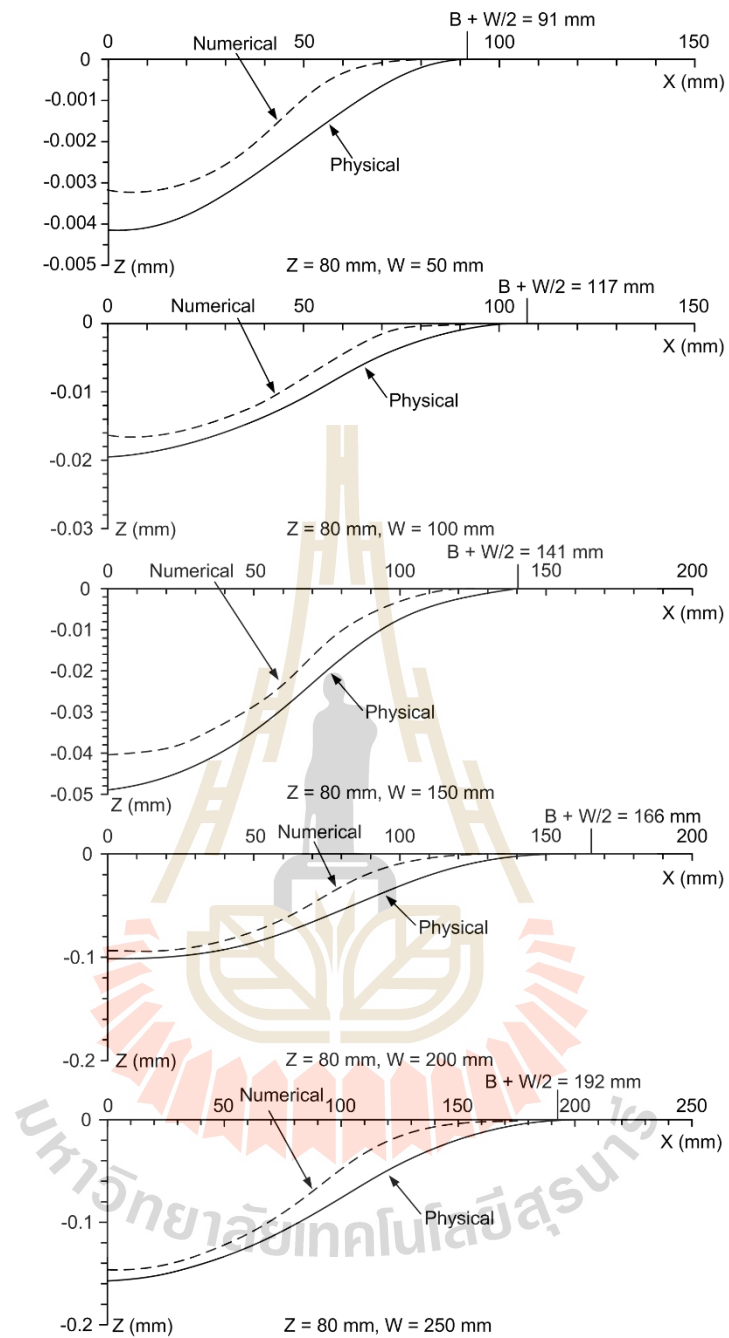


**Figure 7.10** Comparisons of subsidence profiles measured from physical and predicted by numerical model under  $E_m = 5$  MPa and opening depth = 80 mm.

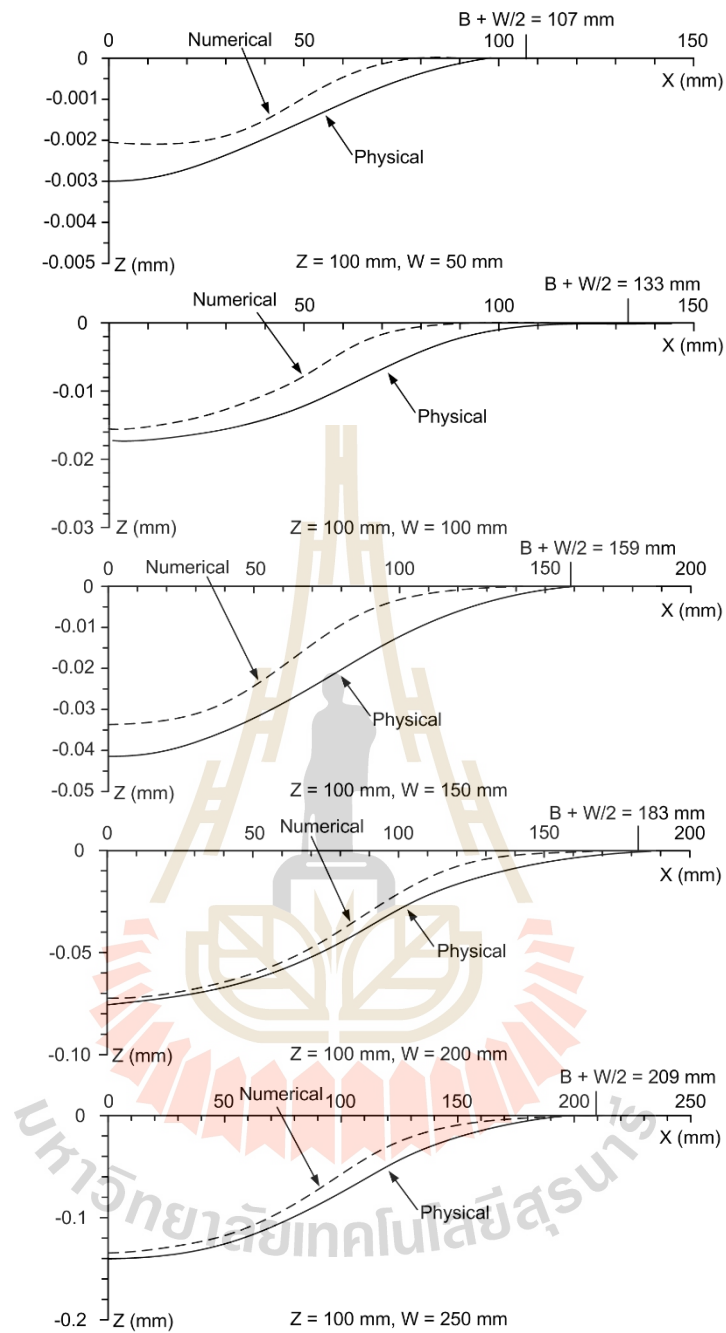


**Figure 7.11** Comparisons of subsidence profiles measured from physical and predicted by numerical model under  $E_m = 5$  MPa and opening depth = 100 mm.

# CHAPTER VIII

## PROFILE FUNCTIONS

### 8.1 Introduction

The analytical methods given by Singh (1992) are used to calculate the subsidence components as affected by the opening geometries and overburden properties. The maximum subsidence, slope, curvature, horizontal displacement and strain are estimated using different profile functions. The analytical results are compared and verified with the laboratory model.

### 8.2 Profile functions

Profile function involves the derivation of a mathematical function that can be used to plot a complete profile of the subsidence trough as the surface. The hyperbolic, exponential and trigonometric functions are used here to predict the subsidence components under the boundary conditions identical to those of the physical models. These functions have been widely used for mine subsidence prediction (Karmis et al., 1984; Singh, 1992; Rafael and Javier, 2000). They are briefly described below:

hyperbolic function : 
$$S(x) = 0.5 \cdot S_{\max} \left[ 1 - \tanh\left(\frac{cx}{B}\right) \right] \quad (8.1)$$

exponential function: 
$$S(x) = S_{\max} \cdot \exp\left[-0.5 \frac{(x+B)^2}{B^2}\right] \quad (8.2)$$

trigonometric function: 
$$S(x) = S_{\max} \cdot \sin^2 \left[ \left( \frac{\pi}{4} \right) \cdot \left( \frac{x}{B} - 1 \right) \right] \quad (8.3)$$

where  $x$  is the horizontal distance from the point of inflection,  $c$  is a arbitrary constant ( $c = 1.4$  for subcritical widths, Singh, 1992) and  $B$  defines the extent of subsidence trough, ( $B = Z \cdot \tan \gamma$ ).

The slope,  $G(x)$ , is determined by taking the first derivative of  $S(x)$  in equations (8.1), (8.2) and (8.3) with respect to  $x$ . The three functions can be written as:

hyperbolic function: 
$$\frac{\partial S(x)}{\partial x} = G(x) = 0.5 \cdot S_{\max} \cdot \frac{c}{B} \cdot \operatorname{sech}^2 \left( \frac{cx}{B} \right) \quad (8.4)$$

exponential function: 
$$\frac{\partial S(x)}{\partial x} = G(x) = \frac{(x+B) \cdot S_{\max} \cdot \exp \left[ -0.5 \frac{(x+B)^2}{B^2} \right]}{B^2} \quad (8.5)$$

trigonometric function: 
$$\frac{\partial S(x)}{\partial x} = G(x) = S_{\max} \frac{\pi \cdot \cos \left( \left( \frac{\pi}{4} \right) \cdot \left( \frac{x}{B} - 1 \right) \right)}{2B} \quad (8.6)$$

The curvature,  $K(x)$ , is determined by taking the first derivative of  $G(x)$  in equations (8.4), (8.5) and (8.6) with respect to  $x$ .

hyperbolic function: 
$$\frac{\partial G(x)}{\partial x} = K(x) = \frac{c^2}{B^2} \cdot S_{\max} \left[ \operatorname{sech}^2 \left( \frac{cx}{B} \right) \cdot \tanh \left( \frac{cx}{B} \right) \right] \quad (8.7)$$

exponential function: 
$$\frac{\partial G(x)}{\partial x} = K(x) = \frac{(x+B)^2 \cdot S_{\max} \cdot \exp\left[\frac{-0.5(x+B)^2}{B^2}\right]}{B^4} \quad (8.8)$$

$$= \frac{S_{\max} \cdot \exp\left[\frac{-0.5(x+B)^2}{B^2}\right]}{B^2}$$

trigonometric function: 
$$\frac{\partial G(x)}{\partial x} = K(x) = \frac{\pi \cdot S_{\max} \left\{ \pi \cdot \cos^2 \left[ \frac{\pi(x-B)}{4B} \right] \right\}}{8B^2} \quad (8.9)$$

$$= \frac{\pi \cdot S_{\max} \left\{ \pi \cdot \sin^2 \left[ \frac{\pi(x-B)}{4B} \right] \right\}}{8B^2}$$

The profile function methods are simple to use for application. The profile functions are easy to calibrate with field data and also yield satisfactory results, but they can only be applied to simple two-dimensional problems of rectangular extraction.

### 8.3 Comparison of analytical and physical results

Figures 8.1 through 8.6 compare the subsidence profiles obtained from the three functions with those measured from the physical model tests along opening cross-section for different  $W/Z$  and  $E_m$ . It is obvious the three functions give different subsidence characteristics in terms of surface slope, curvature and trough volume even though they have the same maximum subsidence and trough width which are maintained constant for each case. The results indicate that the exponential and trigonometric functions underpredicted the slope, strain and curvature measured from the physical model simulation, while the hyperbolic function is overpredicted with the measurements results.

The calculated maximum surface slope ( $G_{\max}$ ), curvature angle ( $\psi$ ), maximum horizontal displacement-to-opening depth ratio ( $U_{\max}/Z$ ) and maximum surface strain ( $\epsilon_{\max}$ ) obtained from profile functions are compared with physical measurement and summarize in Tables 8.1 through 8.4. The discrepancies among the three functions and the test models are shown in Figures 8.7 through 8.10 in terms of the  $G_{\max}$ ,  $\psi$ ,  $U_{\max}/Z$  and  $\epsilon_{\max}$ . All solutions show the rapid increase of the  $G_{\max}$  when the  $W/H$  ratios increase and elastic moduli decrease. This is true for all opening widths, which implies that both laboratory test results and profile solutions are correct. Nevertheless some discrepancies remain. The hyperbolic function overestimates the maximum surface slope for all opening widths and depths by about 10%. The exponential and trigonometric functions are about 5 and 10% underestimate the measured slope. The predicted  $\psi$  (Figures 8.8),  $U_{\max}/Z$  (Figures 8.9) and  $\epsilon_{\max}$  (Figures 8.10) tend to be similar with the  $G_{\max}$  for all cases.



**Table 8.1** Maximum slope ( $\times 10^{-3}$ ) values from physical and analytical methods under different opening geometries and elastic moduli.

Test variables			Physical	Profile functions		
$E_m$ (MPa)	$E_p$ (GPa)	$W_m/Z_m$		Hyperbolic	Exponential	Trigonometric
1	3.76	0.5	0.25	0.28	0.24	0.21
		1.0	0.88	0.95	0.82	0.80
		2.0	3.52	3.94	3.41	3.27
		3.3	9.22	10.20	8.84	8.59
		5.0	21.50	24.00	20.80	17.80
3	10.96	0.5	0.06	0.06	0.06	0.05
		1.0	0.24	0.27	0.23	0.23
		2.0	1.28	1.41	1.22	1.15
		3.3	2.61	2.97	2.57	2.44
		5.0	5.72	6.23	5.40	5.20
5	16.84	0.5	0.03	0.03	0.02	0.02
		0.6	0.04	0.04	0.04	0.04
		0.8	0.10	0.11	0.09	0.08
		1.0	0.13	0.15	0.13	0.10
		1.3	0.18	0.20	0.17	0.16
		1.3	0.22	0.23	0.20	0.18
		1.5	0.31	0.35	0.30	0.26
		1.7	0.30	0.32	0.28	0.25
		1.9	0.46	0.52	0.45	0.41
		2.0	0.59	0.63	0.54	0.52
		2.5	0.66	0.71	0.62	0.57
		2.5	0.82	0.87	0.75	0.68
		2.5	0.95	1.06	0.92	0.83
		2.5	1.05	1.16	1.00	0.94
		3.1	1.53	1.64	1.42	1.31
		3.3	1.57	1.73	1.50	1.40
		3.8	1.54	1.66	1.44	1.37
4.2	2.73	2.98	2.58	2.38		
5.0	3.64	3.91	3.28	3.19		
6.3	6.23	6.86	5.95	5.63		

**Table 8.2** Maximum horizontal displacement-to-opening depth ratio values from physical and analytical methods under different opening geometries and elastic moduli.

Test variables			Physical	Profile functions		
$E_m$ (MPa)	$E_p$ (GPa)	$W_m/Z_m$		Hyperbolic	Exponential	Trigonometric
1	3.76	0.5	0.0003	0.0003	0.0003	0.0003
		1.0	0.0007	0.0005	0.0004	0.0004
		2.0	0.0042	0.0047	0.0041	0.0039
		3.3	0.0184	0.0204	0.0177	0.0172
		5.0	0.0645	0.0720	0.0624	0.0534
3	10.96	0.5	0.0001	0.0001	0.0001	0.0001
		1.0	0.0003	0.0003	0.0003	0.0003
		2.0	0.0015	0.0017	0.0015	0.0014
		3.3	0.0052	0.0059	0.0051	0.0049
		5.0	0.0172	0.0187	0.0162	0.0156
5	16.84	0.5	0.0000	0.0000	0.0000	0.0000
		0.6	0.0001	0.0001	0.0001	0.0001
		0.8	0.0002	0.0002	0.0002	0.0002
		1.0	0.0002	0.0002	0.0002	0.0001
		1.3	0.0003	0.0003	0.0003	0.0002
		1.3	0.0006	0.0007	0.0006	0.0006
		1.5	0.0004	0.0004	0.0004	0.0003
		1.7	0.0006	0.0006	0.0006	0.0005
		1.9	0.0007	0.0008	0.0007	0.0006
		2.0	0.0007	0.0008	0.0007	0.0006
		2.5	0.0013	0.0014	0.0012	0.0011
		2.5	0.0014	0.0016	0.0014	0.0012
		2.5	0.0016	0.0017	0.0015	0.0014
		2.5	0.0020	0.0021	0.0019	0.0017
		3.1	0.0023	0.0025	0.0021	0.0020
		3.3	0.0031	0.0035	0.0030	0.0028
		3.8	0.0046	0.0050	0.0043	0.0041
4.2	0.0055	0.0060	0.0052	0.0048		
5.0	0.0109	0.0117	0.0098	0.0096		
6.3	0.0187	0.0206	0.0178	0.0169		

**Table 8.3** Maximum horizontal strain ( $\times 10^{-3}$ ) values from physical and analytical methods under different opening geometries and elastic moduli.

Test variables			Physical	Profile functions		
$E_m$ (MPa)	$E_p$ (GPa)	$W_m/Z_m$		Hyperbolic	Exponential	Trigonometric
1	3.76	0.5	0.012	0.013	0.011	0.010
		1.0	0.042	0.046	0.040	0.039
		2.0	0.169	0.189	0.164	0.157
		3.3	0.443	0.490	0.424	0.412
		5.0	1.032	1.152	0.998	0.854
3	10.96	0.5	0.003	0.003	0.003	0.002
		1.0	0.012	0.013	0.011	0.011
		2.0	0.061	0.068	0.059	0.055
		3.3	0.125	0.143	0.123	0.117
		5.0	0.275	0.299	0.259	0.250
5	16.84	0.5	0.001	0.001	0.001	0.001
		0.6	0.002	0.002	0.002	0.002
		0.8	0.005	0.005	0.005	0.004
		1.0	0.006	0.007	0.006	0.005
		1.3	0.009	0.010	0.008	0.008
		1.3	0.010	0.011	0.010	0.009
		1.5	0.015	0.017	0.014	0.013
		1.7	0.014	0.015	0.013	0.012
		1.9	0.022	0.025	0.022	0.020
		2.0	0.029	0.030	0.026	0.025
		2.5	0.032	0.034	0.030	0.027
		2.5	0.039	0.042	0.036	0.033
		2.5	0.046	0.051	0.044	0.040
		2.5	0.050	0.055	0.048	0.045
		3.1	0.074	0.079	0.068	0.063
		3.3	0.076	0.083	0.072	0.067
		3.8	0.074	0.080	0.069	0.066
4.2	0.131	0.143	0.124	0.114		
5.0	0.175	0.188	0.158	0.153		
6.3	0.299	0.329	0.285	0.270		

**Table 8.4** Curvature angle (degrees) values from physical and analytical methods under different opening geometries and elastic moduli.

Test variables			Physical	Profile functions		
$E_m$ (MPa)	$E_p$ (GPa)	$W_m/Z_m$		Hyperbolic	Exponential	Trigonometric
1	3.76	0.5	0.014	0.016	0.014	0.012
		1.0	0.050	0.054	0.047	0.046
		2.0	0.202	0.226	0.195	0.187
		3.3	0.528	0.584	0.506	0.492
		5.0	1.232	1.375	1.192	1.020
3	10.96	0.5	0.003	0.004	0.003	0.003
		1.0	0.014	0.015	0.013	0.013
		2.0	0.073	0.081	0.070	0.066
		3.3	0.150	0.170	0.147	0.140
		5.0	0.328	0.357	0.309	0.298
5	16.84	0.5	0.001	0.001	0.001	0.001
		0.6	0.002	0.002	0.002	0.002
		0.8	0.006	0.006	0.005	0.005
		1.0	0.008	0.009	0.007	0.006
		1.3	0.011	0.011	0.010	0.009
		1.3	0.012	0.013	0.012	0.011
		1.5	0.018	0.020	0.017	0.015
		1.7	0.017	0.018	0.016	0.014
		1.9	0.026	0.030	0.026	0.023
		2.0	0.034	0.036	0.031	0.030
		2.5	0.038	0.041	0.035	0.033
		2.5	0.047	0.050	0.043	0.039
		2.5	0.055	0.061	0.053	0.047
		2.5	0.060	0.066	0.057	0.054
		3.1	0.088	0.094	0.081	0.075
		3.3	0.090	0.099	0.086	0.080
		3.8	0.088	0.095	0.083	0.078
		4.2	0.156	0.171	0.148	0.136
5.0	0.208	0.224	0.188	0.183		
6.3	0.357	0.393	0.341	0.323		

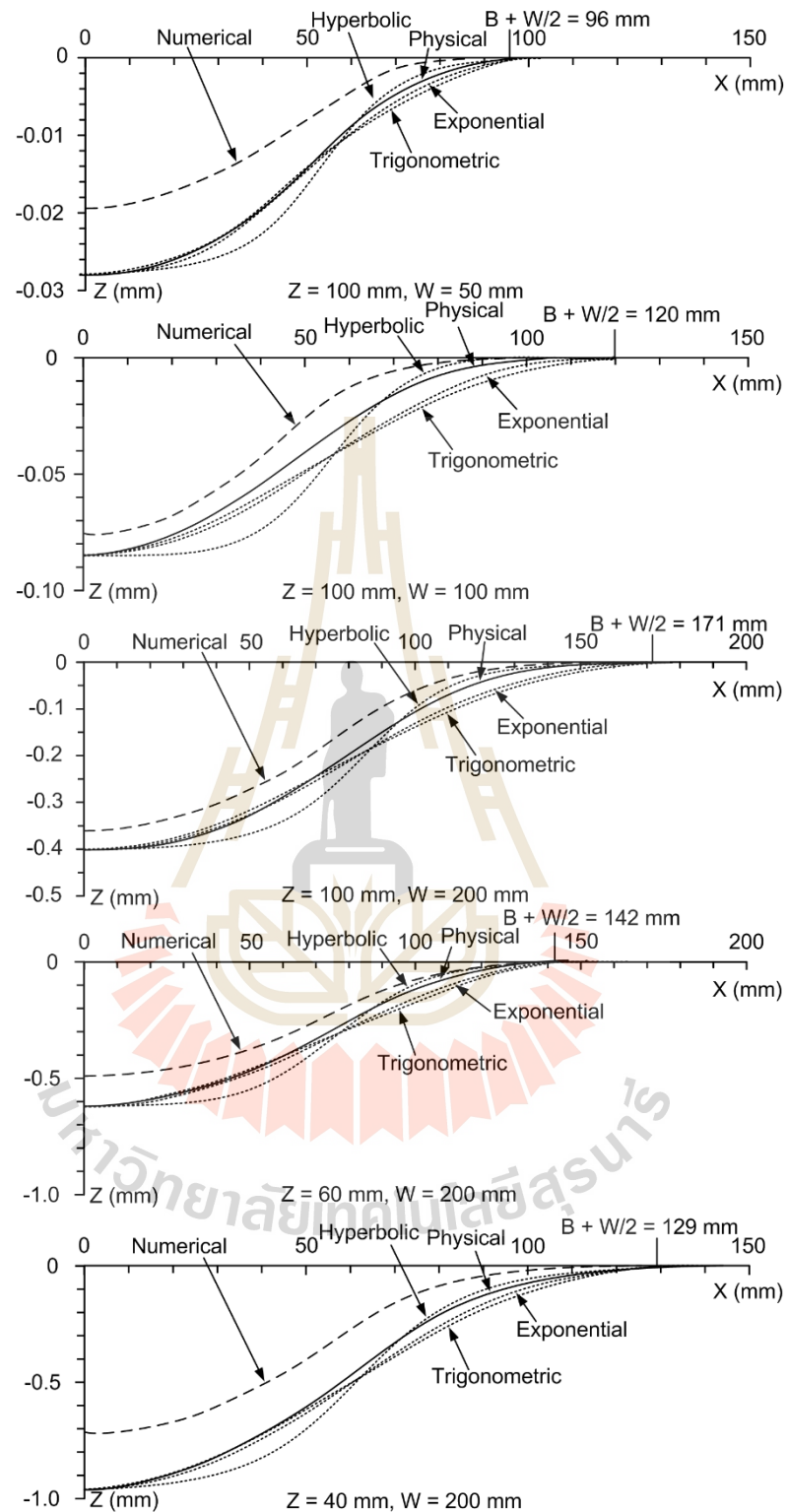


**Figure 8.1** Comparisons of subsidence profile predicted by different functions under  $E_m = 1$  MPa for various opening width and depth.

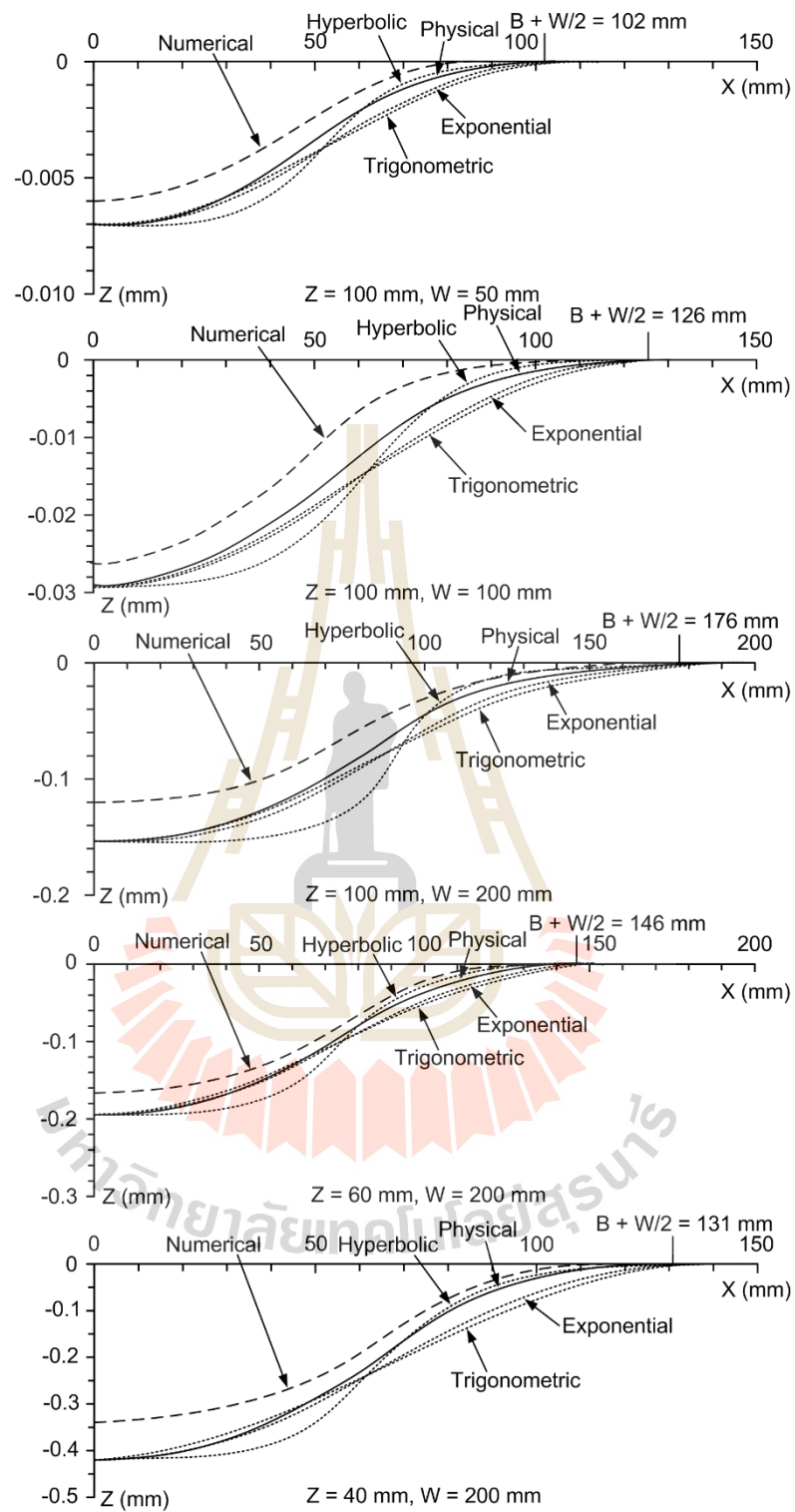


**Figure 8.2** Comparisons of subsidence profile predicted by different functions under

$E_m = 3$  MPa for various opening width and depth.

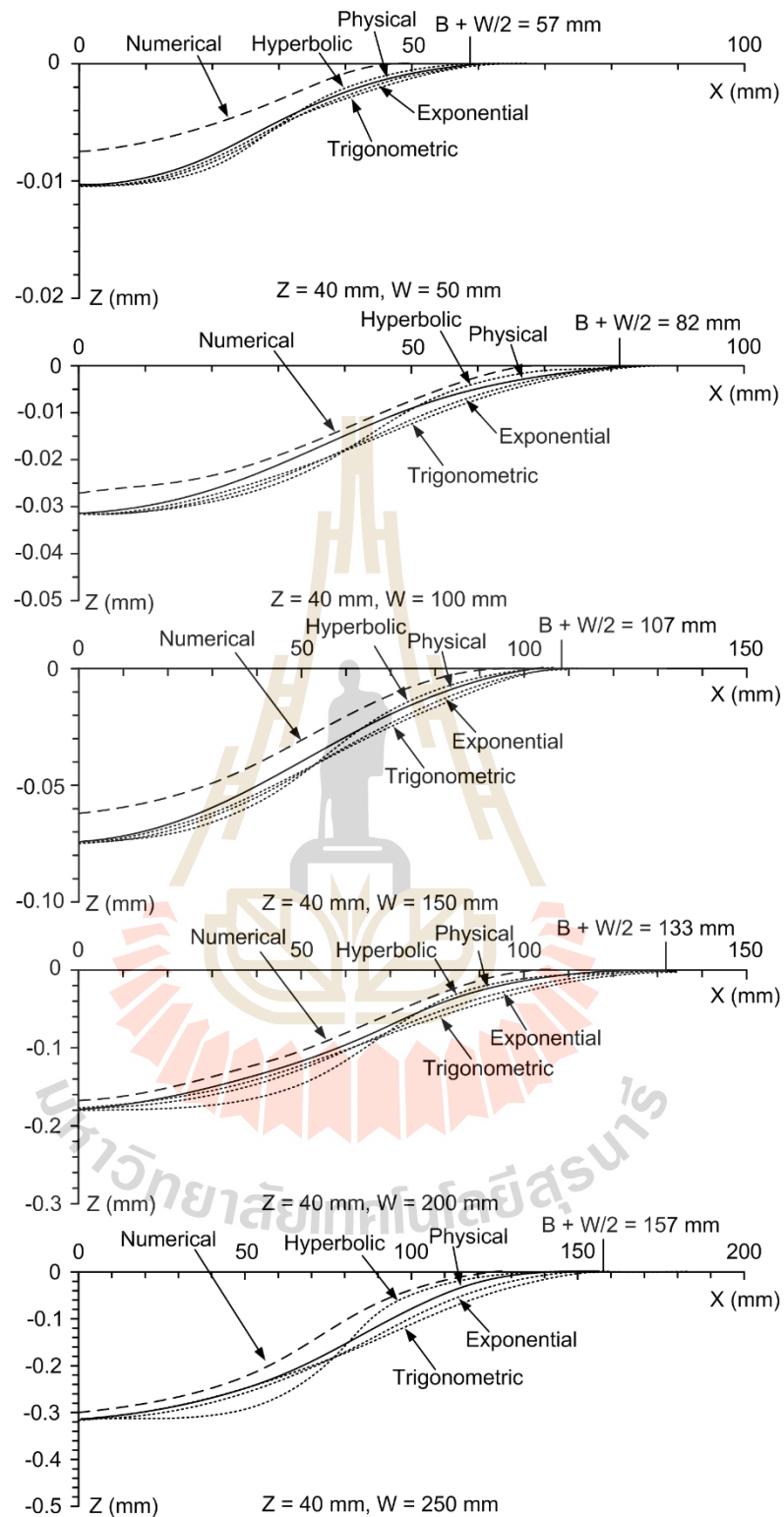


**Figure 8.3** Comparisons of subsidence profile predicted by different functions under

$E_m = 5 \text{ MPa}$  and opening depth = 40 mm.

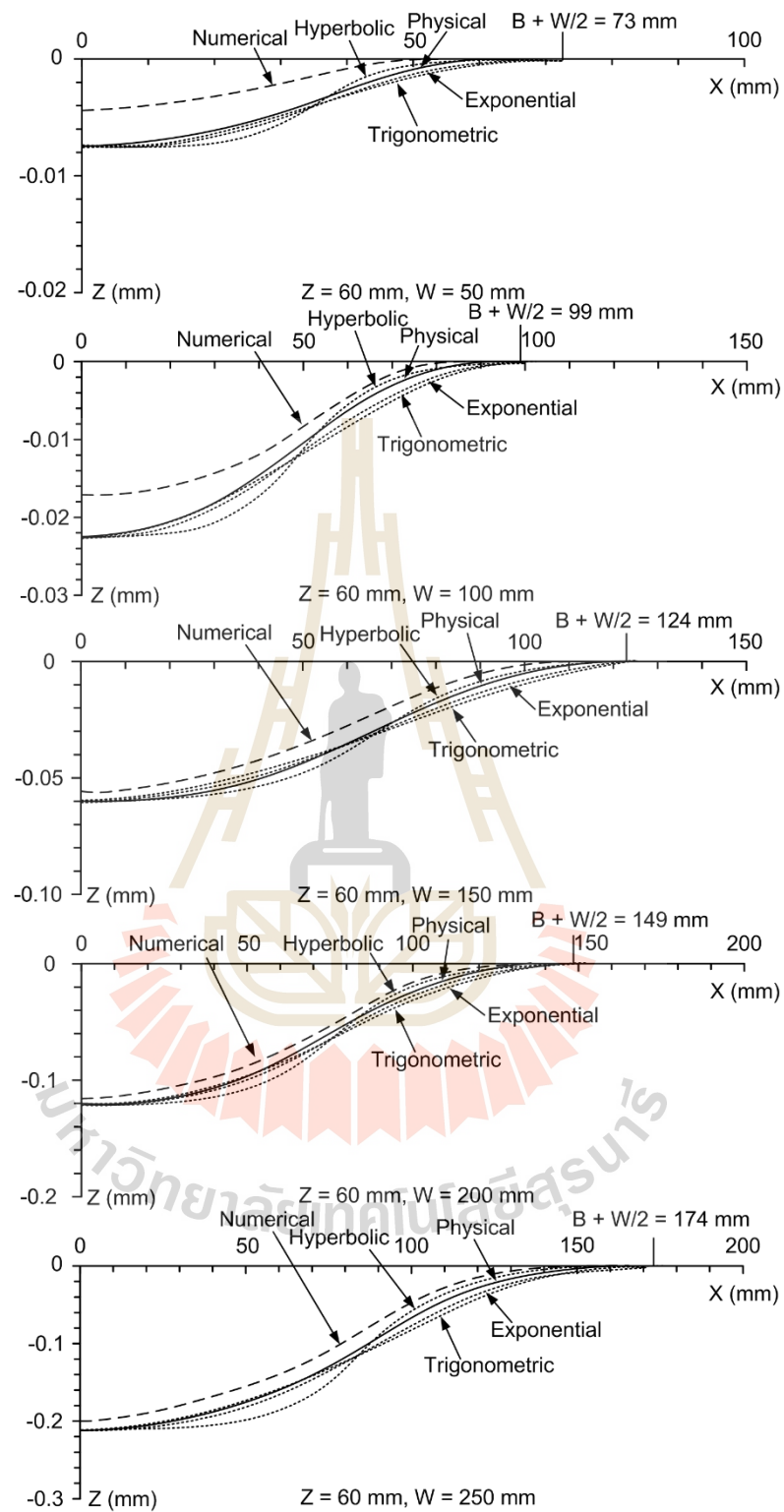


**Figure 8.4** Comparisons of subsidence profile predicted by different functions under  $E_m = 5$  MPa and opening depth = 60 mm.



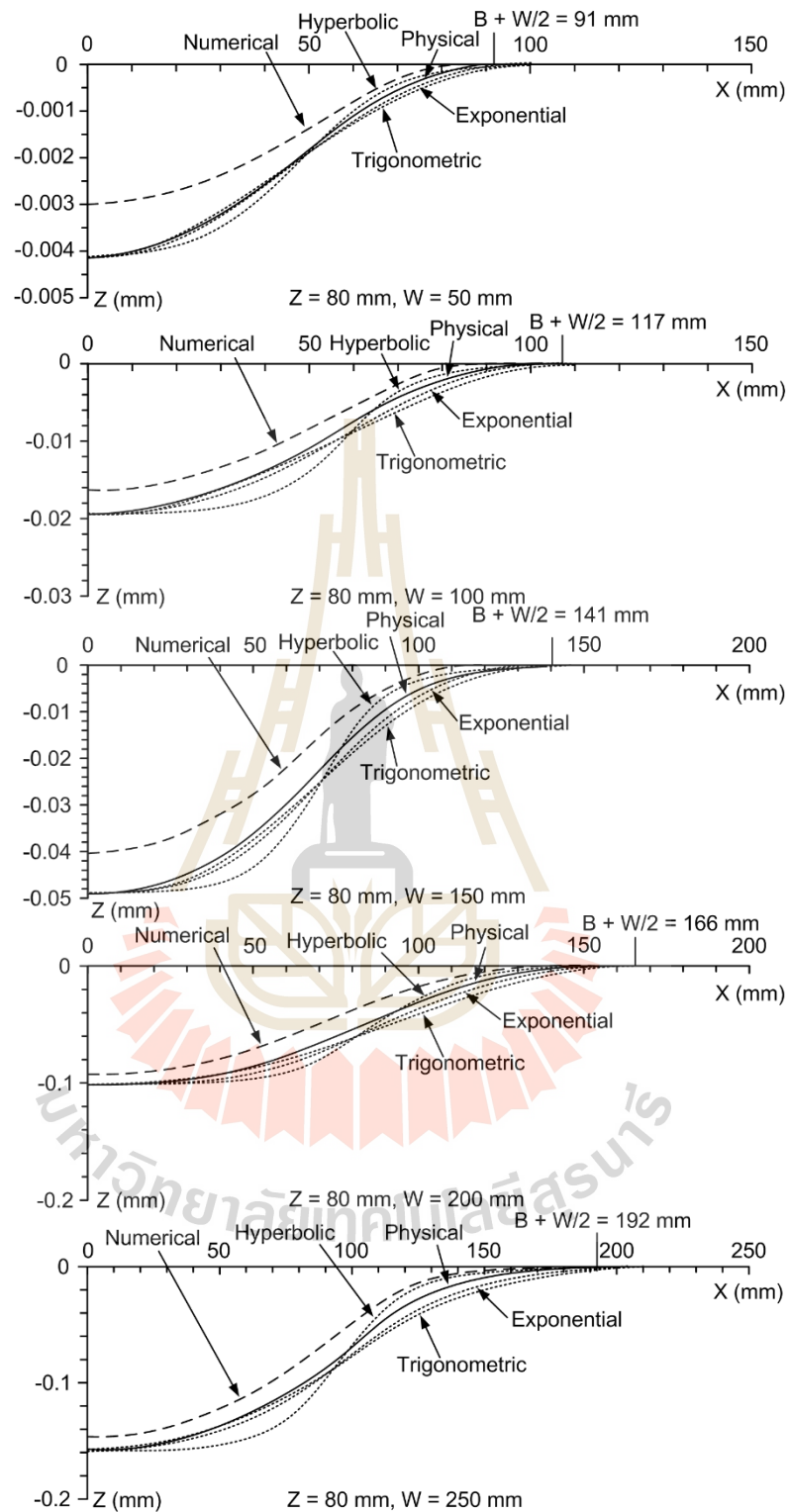


**Figure 8.5** Comparisons of subsidence profile predicted by different functions under

$E_m = 5$  MPa and opening depth = 80 mm.

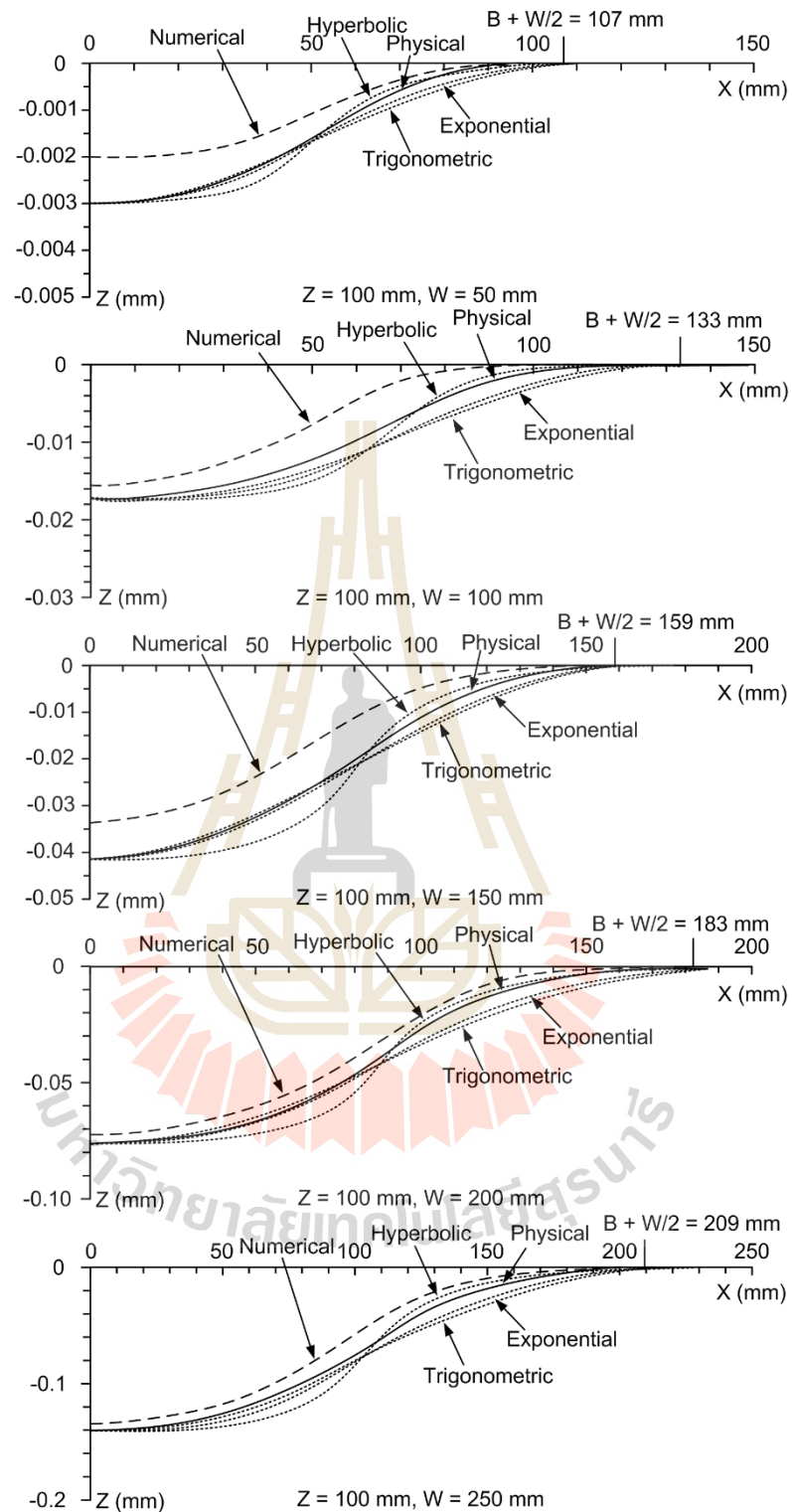


**Figure 8.6** Comparisons of subsidence profile predicted by different functions under  $E_m = 5 \text{ MPa}$  and opening depth = 100 mm.

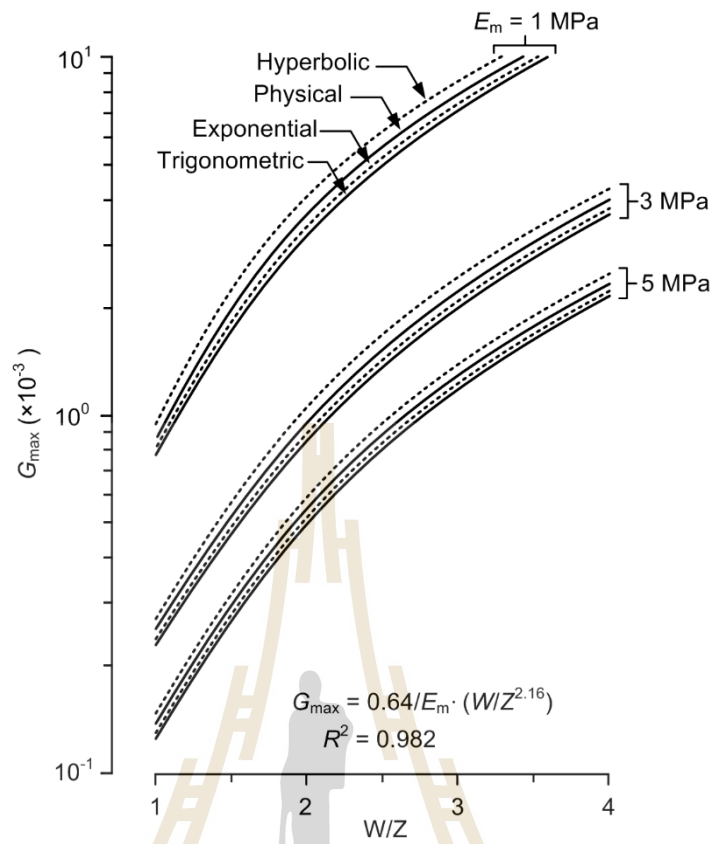


**Figure 8.7** Maximum slope comparisons between physical model and three profile functions where  $W/Z$  ratios = 1 – 4.

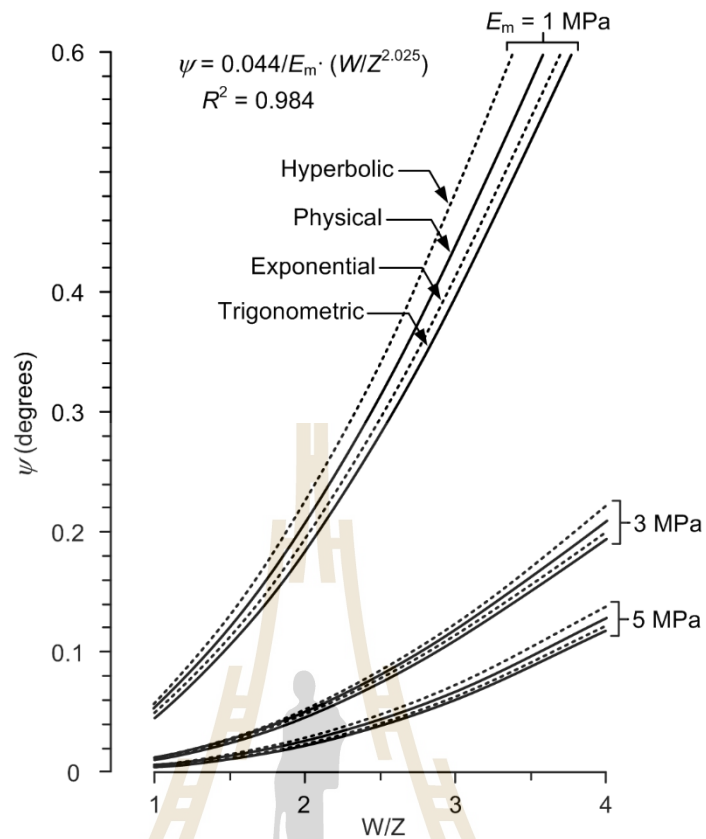


**Figure 8.8** Curvature angle comparisons between physical model and three profile functions where  $W/Z$  ratios = 1 – 4.

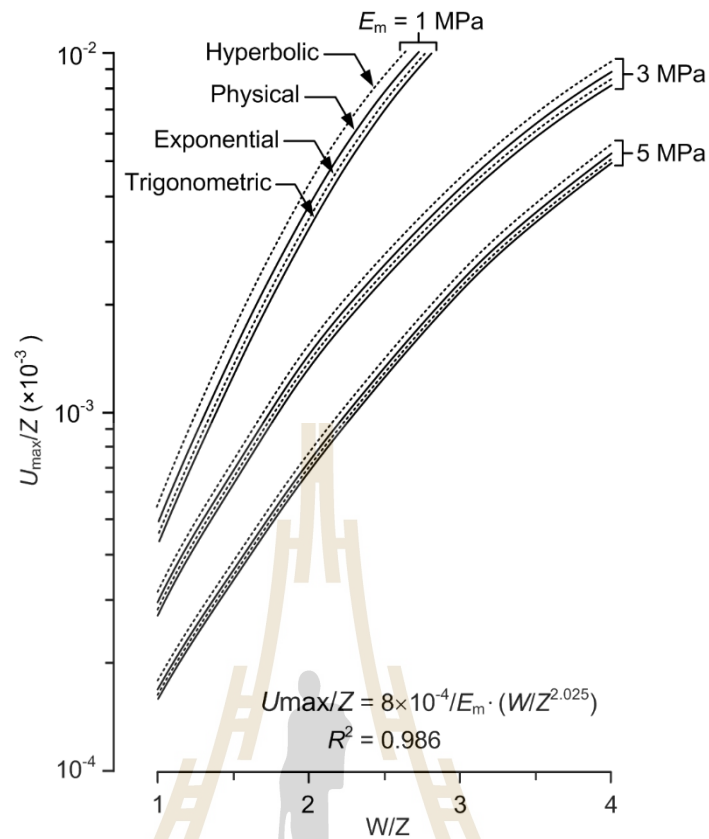


**Figure 8.9** Maximum horizontal displacement-to-opening depth ratio comparisons between physical model and three profile functions where  $W/Z$  ratios = 1

- 4.

มหาวิทยาลัยเทคโนโลยีสุรนารี

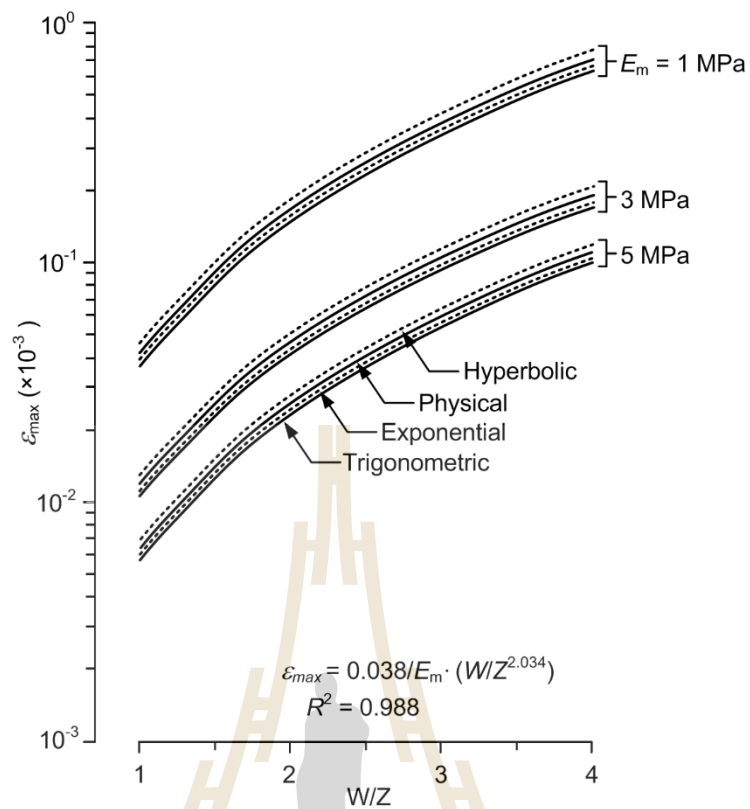


**Figure 8.10** Maximum horizontal strain comparisons between physical model and three profile functions where  $W/Z$  ratios = 1 – 4.

## CHAPTER IX

### DISCUSSIONS AND CONCLUSIONS

#### 9.1 Discussions

This section discusses the key issues relevant to the reliability of the test schemes and the adequacies of the test results. Comparisons of the results and findings from this study with those obtained elsewhere under similar test conditions are also made.

(1) The numbers of the physical models seem adequate, as evidenced by the good coefficients of correlation subsidence components, opening geometries and elastic moduli of the overburden.

(2) The maximum subsidence magnitudes are highly sensitive to both opening depth and width (Figure 6.3(b)).

(3) The close agreement between the numerical simulations and the physical model tests suggests that the concept, procedure and results in the physical model are appropriate and correct. Both methods indicate that maximum subsidence-to-opening depth ratio increases with increasing opening width-to-depth ratios. The  $\gamma$  tends to independent of the opening widths and depths.

(4) The subsidence profiles obtained from the numerical models are shallower and narrower than those obtained from the physical model. Under the same opening depth and width, a soft overburden (lower  $E_m$ ) shows deeper subsidence trough and narrower extent than those obtained under stiffer overburden (higher  $E_m$ ). This is

primarily because the soft overburden can deform easier than the rigid overburden.

(5) The three functions give different subsidence characteristics in terms of surface slope, curvature and trough volume even though they have the same maximum subsidence and trough width which are maintained constant for all cases. The results indicate that the exponential and trigonometric functions underpredict the slope, strain and curvature measured from the physical model simulations, while the hyperbolic function overpredicts the measurements results.

(6) A conservative approach for the actual subsidence profile prediction under sub-critical to critical conditions would be obtained by applying the hyperbolic function for the maximum slope, maximum surface strain and curvature angle predictions.

(7) The subsidence trough volumes predicted by the three functions are similar.

(8) Applications of the results obtained here to other different sequences and thickness of the Maha Sarakham formation to other locations and conditions may be possible by applying the similarity theory (Table 6.4). Different opening widths can also be incorporated to obtain the corresponding prototype condition and obtaining the desired subsidence profiles.

## 9.2 Conclusions

All objectives and requirements of this study have been met. The results of the laboratory testing and analyses can be concluded as follows:

(1) The effects of opening geometries and overburden properties can be observed from  $S_{\max} - Z$ ,  $G_{\max} - W/Z$ ,  $\psi - W/Z$ ,  $U_{\max}/Z - W/Z$  and  $\epsilon_{\max} - W/Z$



diagrams. These values increase with increasing opening width-to-depth ratio and elastic moduli while  $\gamma$  tends to be independent of the opening width-to-depth ratio (Figures 6.3 through 6.5).

(2) The volumes of subsidence trough observed from the physical model are always less than the opening volumes below. The largest trough volume is obtained for  $W/Z = 5.0$  and  $E_m = 1$  MPa, which is about 5% of the opening volume (Figure 6.12). The subsidence trough tends to increase as the opening width increases, particularly for soft overburden (lower  $E_m$  value).

(3) FLAC simulation and physical model results are virtually identical. For all cases, the  $\gamma$  values predicted from the numerical simulations are slightly higher than those obtained from physical results (about 1%), while the maximum subsidence and volumetric ratio of trough-to-opening width obtained from the FLAC model is slightly lower than the physical model (about 5% and 7%). The discrepancies are probably due to the sizes and number of the elements used in the mesh model. The smaller elements and larger number of the elements would provide even closer numerical solutions to the physical model test results.

(4) A new finding is obtained in terms of the accuracy and representativeness of the commonly used profile functions for the subsidence predictions under sub-critical to critical conditions. The exponential and hyperbolic functions provide similar  $G_{\max} - W/Z$ ,  $\psi - W/Z$ ,  $U_{\max}/Z - W/Z$  and  $\varepsilon_{\max} - W/Z$  relations with the laboratory measurements. The hyperbolic function slightly overestimates (by about 10%) the subsidence components. The exponential and trigonometric functions however underestimate the results by about 5-10% (Figures 8.7 through 8.10).

### 9.3 Recommendations for future studies

The uncertainties of the investigation and results discussed above lead to the recommendations for further studies. To confirm the conclusions drawn in this research, more testing is required as follows:

(1) The physical model simulations should be performed on a wider range of the opening geometries to confirm the effects of opening depth, width, length and height on the extent of surface subsidence. More testings are also preferable on a variety of materials with different mechanical properties for overburden simulations.

(2) The effects of vertical and horizontal stresses under various mechanical properties on subsidence trough should be studied for each overburden thickness.

(3) The effects of overburden layers on surface subsidence should be assessed particularly to verify that the average property values ( $E$  and  $\rho$ ) of the overburden as used here are adequately representative of the prototype conditions.

## REFERENCES

- Adachi, T., Kimura, M. and Kishida, K. (2003). Experimental study on the distribution of earth pressure and surface settlement through three-dimensional trapdoor tests. **Tunnelling and Underground Space Technology**. 18: 171-183.
- Allersma, N. (1995). Simulation of subsidence in soil layers in a geotechnical centrifuge. In **Proceedings of the Fifth International Symposium on Land Subsidence**. Wallingford, UK.
- Asadi, A., Shahriar, K. and Goshtasbi, K. (2004). Profiling function for surface subsidence prediction in mining inclined coal seams. **Journal of Mining Sciences**. 40(2): 142-146.
- Asadi, A., Shahriar, K., Goshtasbi, K. and Najm, K. (2005). Development of new mathematical model for prediction of surface subsidence due to inclined coal-seam mining. **Journal of the Southern African Institute of Mining and Metallurgy**. 105(11): 15-20.
- ASTM D695-10 (2010). **Standard test method for compressive properties of rigid plastics**. Annual Book of ASTM Standards, American Society for Testing and Materials, West Conshohocken, PA.
- Bachmann, D., Bouissou, S. and Chemenda, A. (2006). Influence of large scale topography on gravitational rock mass movements: New insights from physical modeling. **Geophysical Research Letters**. 33: 1-4.

- Cai, Y., Verdel, T. and Deck, O. (2014). On the topography influence on subsidence due to horizontal underground mining using the influence function method. **Computer and Geotechnics**. 61: 328-340.
- Crosby, K.S. (2007). Integration of rock mechanics and geology when designing the Udon South sylvinitic mine. In **Proceeding of the 1th Thailand Symposium on Rock Mechanics** (pp. 3-22).
- Cui, X., Miao, X., Wang, J., Yang, S., Liu, H., Song, Y., Liu, H. and Hu, X. (2000). Improved prediction of differential subsidence caused by underground mining. **International Journal of Rock Mechanics and Mining Sciences**. 37(4): 615-627.
- Dai, H., Li, W., Liu, Y., and Jiang, Y. (2011). Numerical simulation of surface movement laws under different unconsolidated layers thickness. **Transactions of Nonferrous Metals Society of China**. 21: 599-603.
- Franzius, J.N., Potts, D.M. and Burland, J.B. (2005). The influence of soil anisotropy and  $K_0$  on ground surface movements resulting from tunnel excavation. **Geotechnique**. 55(1): 189-199.
- Fuenkajorn, K. and Archeeploha, S. (2009). Prediction of cavern configurations from subsidence data. **Engineering Geology**. 110: 21-29.
- Fuenkajorn, K. and Archeeploha, S. (2011). Estimation of cavern configurations from subsidence data. **Bulletin of Engineering Geology and the Environment**. 70: 53-61.
- Fuenkajorn, K. and Phueakphum, D. (2010). Effects of cyclic loading on mechanical properties of Maha Sarakham salt. **Engineering Geology**. 112: 43-52.

- Gao, F., Stead, D. and Coggan, J. (2014). Evaluation of coal longwall caving characteristics using an innovative UDEC Trigon approach. **Computer and Geotechnics**. 55: 448-460.
- Ghabraie, B., Ren, G., Zhang, X. and Smith, J. (2015). Physical modelling of subsidence from sequential extraction of partially overlapping longwall panels and study of substrata movement characteristics. **International Journal of Coal Geology**. 140: 71-83.
- Heib, A.I., Emeriault, F., Caudron, M., Nghiem, L. and Hor, B. (2013). Large-scale soil-structure physical model (1g)-assessment of structure damages. **International Journal of Physical Modelling in Geotechnics**. 13(4): 138-152.
- Helm, P.R., Davie, C.T. and Glendinning, S. (2013). Numerical modelling of shallow abandoned mine working subsidence affecting transport infrastructure. **Engineering Geology**. 154: 6-19.
- Itasca (1992). **User Manual for FLAC-Fast Lagrangian Analysis of Continua**. Version 4.0, Minneapolis, Minnesota.
- Iwanec, A.M., Carter, J.P. and Hambleton, J.P. (2016). Geomechanics of subsidence above single and multi-seam coal mining. **International Journal of Rock Geotechnical Engineering**. 1-10.
- Karmis, M., Goodman, G. and Hasenfus, G. (1984). Subsidence prediction techniques for longwall and room and pillar panels in Appalachia. In **Proceedings of the 2nd International Conference on Stability in Underground Mining**. AIME (pp. 541-553).

- Meguid, M.A., Saada, O., Nunes, M.A. and Mattar, J. (2008). Physical modeling of tunnels in soft ground: A review. **Tunnelling and Underground Space Technology**, 23: 185-198.
- Migliazza, M., Chiorboli, M. and Giani, G.P. (2009). Comparison of analytical method, 3D finite element model with experimental subsidence measurements resulting from the extension of the Milan underground. **Computer and Geotechnics**, 36: 113-124.
- National Coal Board (1975). **Subsidence Engineers Handbook**. National Coal Board, London, pp. 401.
- Nieland, J.D. (1991). **SALT-SUBSID: A PC-Based Subsidence Model**. Solution Mining Research Institute, PA. Report no. 1991-2-SMRI.
- Obert, L. and Duvall, W. (1967). **Rock Mechanics and Design of structure in Rock**. J. Wiley, New York.
- Park, S.H., Adachi, T., Kimura, M. and Kishida, K. (1999). Trap door test using aluminum blocks. In **Proceeding of the 29th Symposium of Rock Mechanics**. pp. 106-111.
- Peck, R.B. (1969). Deep excavations and tunneling in soft ground. In **Proceedings of the 7th international conference on soil mechanics and foundation engineering, State of the art volume** (pp. 225-290). Mexico.
- Rafael, R.D. and Javier, T.A. (2000). Hypothesis of the multiple subsidence trough related to very steep and vertical coal seams and its prediction through profile functions. **Geotechnical and Geological Engineering**, 18: 289-311.

- Rankin, W. (1988). Ground movements resulting from urban tunneling. In **proceedings of 23rd conference of the engineering group of the geological society** (pp. 79-92). London Geological Society.
- Reddish, D.J. (1989). The modeling of rock mass behaviour over large excavations using non-linear finite element techniques. **Mining Department Magazine, University of Nottingham**. 41: 93–102.
- Ren, G. and Li, J. (2008). A study of angle of draw in mining subsidence using numerical modeling techniques. **Electronic Journal of Geotechnical Engineering**. 13: 1-14.
- Ren, W., Guo, C., Peng, Z and Wang, Y. (2010). Model experimental research on deformation and subsidence characteristics of ground and wall rock due to mining under thick overlying terrane. **International Journal of Rock Mechanics and Mining Sciences**. 47: 614-624.
- Shahriar, K., Amoushahi, S. and Arabzadeh, M. (2009). Prediction of surface subsidence due to inclined very shallow coal seam mining using FDM. In **Proceedings of the 2009 Coal Operators' Conference** (pp. 130-139). University of Wollongong, NSW.
- Singh, M.M. (1992). Mine subsidence. In H.L. Hartman (ed). **SME Mining Engineering Handbook** (pp. 938-971.). Society for Mining Metallurgy and Exploration: Inc. Littleton, Colorado.
- Sterpi, D., Cividini, A., Sakurai, S. and Nishitake, S. (1996). Laboratory model tests and numerical analysis of shallow tunnels. In **Proceedings of the International Symposium on Eurock '96 - ISRM**, Torino, vol. 1. Balkema, Rotterdam, pp. 689-696.

- Terzaghi, K. (1936). Stress distribution in dry and in saturated sand above a yielding trap-door. In **Proceeding of the International Conference on Soil Mechanics** (pp. 307-311). Cambridge.
- Thongprapha, T., Fuenkajorn, K. and Daemen, J.J.K. (2015). Study of surface subsidence above an underground opening using a trap door apparatus. **Tunnelling and Underground Space Technology**. 46: 94-103.
- Tunsakul, J., Jongpradist, P., Kongkitkul, W., Wonglert, A. and Youwai, S. (2013). Investigation of failure behavior of continuous rock mass around cavern under high internal pressure. **Tunnelling and Underground Space Technology**. 34: 110-123.
- Wang, F., Du, Y.J., and Yang, X. (2015). Physical modeling on ground responses to tunneling in sand considering the existence of HDPE pipes. **Geotechnical Testing Journal**. 38(1): 85-97.
- Wendai, L. (2000). **Regression Analysis, Linear Regression and Profit Regression, In 13 Chapters; SPSS for Windows: Statistical Analysis**. Publishing House of Electronics Industry, Beijing.
- Wetchasat, K. (2002). Assessment of mechanical performance of rock salt formations for nuclear waste repository in northeastern Thailand. MS thesis, Suranaree University of Technology, Thailand.
- Wood, D.M. (2004). **Geotechnical modelling**. Spon Press, London and New York, 485 p.
- Yao, X.L., Reddish, D.J. and Whittaker, B.N. (1991). Influence of overburden mass behavioural properties on subsidence limit characteristics. **Mining Science and Technology**. 13: 167-173.



Yavuz, H. and Fowell, R.J. (2013). Factors governing the strength and elastic properties of a physical model material used for strata mechanics investigations. **Journal of the Southern African Institute of Mining and Metallurgy**. 63-71.



## **BIOGRAPHY**

Miss Suratwadee Sartkaew was born on February 26, 1990 in Mukdahan, Thailand. She received her Bachelor's Degree in Engineering (Geotechnology) from Suranaree University of Technology in 2011 and received her Master's Degree in Engineering (Geotechnology) from Suranaree University of Technology in 2014. For her post-graduate, she continued to study with a Doctor of Philosophy Program in the Geological Engineering Program, Institute of Engineering, Suranaree university of Technology. During graduation, 2012-2016, she was a part time worker in position of research associate at the Geomechanics Research Unit, Institute of Engineering, Suranaree University of Technology.



มหาวิทยาลัยเทคโนโลยีสุรนารี